UCRL-53543
Distribution Category UC-20d & 21

Multivariable Optimization of Fusion Reactor Blankets

Wayne Raymond Meier

Doctor of Philosophy

in

Engineering

University of California, Berkeley

UCRL--53543

DE84 014131

Manuscript date: April 1984

LAWRENCE LIVERMORE NATIONAL LABORATORY
University of California • Livermore, California • 94550

Available from: National Technical Information Service • U.S. Department of Commerce
5285 Port Royal Road • Springfield, VA 22161 • 19.00 per copy • (Microfiche 4.50)

MULTIVARIABLE OPTIMIZATION OF FUSION REACTOR BLANKETS

Wayne R. Meier

ABSTRACT

The neutron blanket that surrounds the plasma in a deuterium-tritium fusion reactor is an essential component of the system. A method for optimizing the design of a fusion reactor blanket as a function of several design variables is described. The method is applied to two inertial confinement fusion reactor concepts for electric power production.

The optimization problem consists of four key elements: a figure of merit for the reactor, a technique for estimating the neutronic performance of the blanket as a function of the design variables, constraints on the design variables and neutronic performance, and a method for optimizing the figure of merit subject to the constraints.

The figure of merit and constraints depend on the application and design objectives of the particular reactor concept. In general, they

may be functions of the design variables and of the neutronic performance. A variational interpolation method is used to write analytical expressions for the neutronic performance based on a limited number of reference point, neutron transport calculations. This allows the figure of merit and constraints to be evaluated as a function of the design variables. A direct search, nonlinear simplex method is used to optimize the figure of merit subject to the constraints.

The first reactor concept investigated uses a liquid lithium blanket for breeding tritium and a steel blanket to increase the fusion energy multiplication factor. The capital cost per unit of net electric power produced is minimized subject to constraints on the tritium breeding ratio and radiation damage rate. The optimal design has a 91-cm-thick lithium blanket denatured to 0.1% ^{6}Li.

The second reactor concept investigated uses a BeO neutron multiplier and a $LiAlO_2$ breeding blanket. The total blanket thickness is minimized subject to constraints on the tritium breeding ratio, the total neutron leakage, and the heat generation rate in aluminum support tendons. The optimal design consists of a 4.2-cm-thick BeO multiplier and 42-cm-thick $LiAlO_2$ breeding blanket enriched to 34% ^{6}Li.

ACKNOWLEDGEMENTS

I would like to express my appreciation to the many people who helped make this study possible.

First of all, I want to thank my wife Carol. From the very start she has unselfishly supported me in the pursuit of this goal. Her patience, love, and encouragement have been a great source of inspiration.

I would like to thank my committee chairman, Professor Ed Morse, for his direction and advice in this research. It has been a real pleasure to work with him. I am also grateful to Professors Larry Grossman and Maurice Holt for serving on my dissertation committee.

I am indebted to my colleagues in the reactor studies group for their support and recommendations. Jack Hovingh was always ready to hear about my latest results and share his insights. John Pitts has been a continual source of encouragement. The discussions we had on the Cascade concept and the information he supplied were most useful. I am especially grateful to Jim Blink for taking an interest in my research and taking the time to discuss it. His technical advice is greatly appreciated.

I would also like to thank the past and present leaders of the reactor studies group, Mike Monsler and Bill Hogan, and the Inertial Confinement Fusion Program Leader, John Holzrichter, for supporting this project.

A word of thanks also goes to Giles Peterson for helping me with some sticky graphics problems and to Ed Cheng for reviewing an early draft of Chapter 2.

Finally, I am indebted to Karen Hogue for preparing this manuscript. Her skills as a typist and layout artist are evident.

CONTENTS

LIST OF FIGURES

LIST OF TABLES

1. INTRODUCTION

1.1 THE IMPORTANCE OF OPTIMAL BLANKET DESIGN

Controlled thermonuclear fusion holds the promise of one day providing an environmentally acceptable, safe, and abundant source of energy. As national and international fusion programs progress toward the demonstration of energy breakeven, increasing attention is being given to the future applications of fusion. Conceptual design studies have been carried out for electric power plants,[1,2] fusion-fission hybrids which produce fissile fuel for fission reactors,[3] synthetic fuel producers,[4,5] and other applications[6] of both magnetic and inertial confinement fusion.

The majority of current fusion research is focused on demonstrating the feasibility of fusing two heavy isotopes of hydrogen, namely, deuterium (^{2}H or D) and tritium (^{3}H or T). The DT fusion reaction is[7]

$$D + T \rightarrow {}^4He + n. \qquad (1.1)$$

This reaction releases 17.6 MeV; the alpha particles carries off 3.5 MeV and the neutron kinetic energy is 14.1 MeV.[7]

Deuterium is a naturally occurring isotope of hydrogen with an abundance of 1 part in ~6500. Tritium, on the other hand, is radioactive and β^- decays with a half-life of 12.3 years. Therefore, tritium occurs only in trace quantities in nature.

The neutron from the DT fusion reaction, however, can be used to produce tritium via reactions with lithium. The process of producing tritium in a fusion reactor is referred to as tritium breeding.

Natural lithium has two isotopes, 92.58% ^{7}Li and 7.42% ^{6}Li, and both isotopes undergo tritium breeding reactions. These reactions are[8]

$$n + {}^{6}Li \rightarrow T + {}^{4}He + 4.8\ MeV, \qquad (1.2)$$

and

$$n + {}^{7}Li \rightarrow T + {}^{4}He + n' - 2.5\ MeV. \qquad (1.3)$$

As indicated, the breeding reaction with ^{6}Li releases 4.8 MeV, while the breeding reaction with ^{7}Li consumes 2.5 MeV.

The cross sections for these reactions are shown in Fig. 1 (Ref. 9). The $^{7}Li(n,n'T)\alpha$ reaction only occurs with high-energy neutrons, while the cross section for the $^{6}Li(n,T)\alpha$ reaction increases with decreasing neutron energy reaching ~1000 b for thermal neutrons. The ^{7}Li reaction is very important since it produces a tritium atom and a lower energy neutron that can breed more tritium with ^{6}Li. As a result, the fusion reactor can achieve a tritium breeding ratio, defined as tritons bred per triton burned, greater than one. A tritium breeding ratio greater than one is necessary because of the loss of tritium by radioactive decay, and because of losses in the recovery and recycling operations.

Surrounding the fusion plasma is a region within which the neutron kinetic energy is converted to thermal energy and tritium is bred in lithium. This region is referred to as the fusion reactor blanket, neutron blanket or, simply, the blanket. The thermal energy of the blanket is removed by a primary coolant and used to generate electricity. In fusion-fission hybrid applications, fertile materials (^{238}U or ^{232}Th) are located in the blanket where they absorb neutrons to breed fissile fuel.

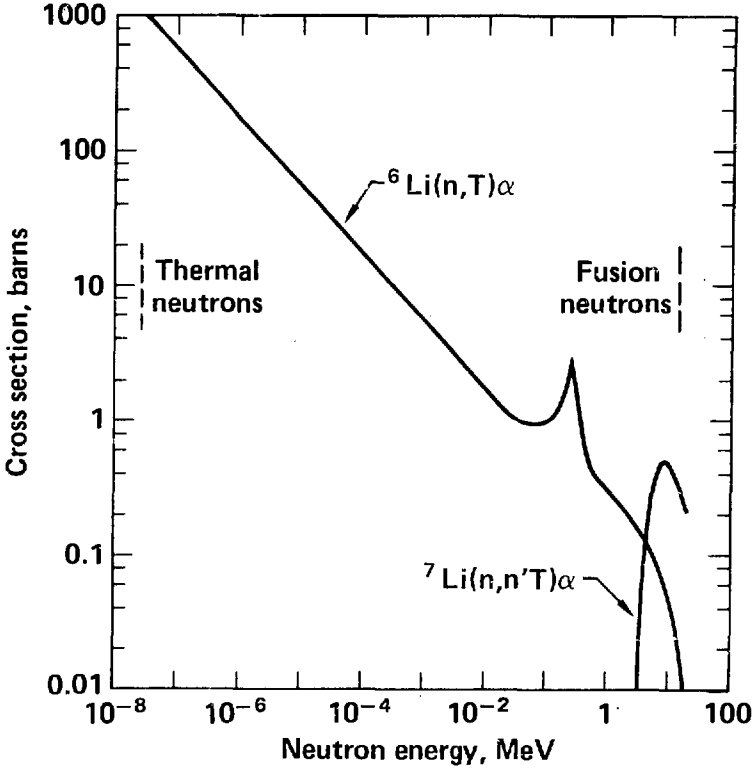

Fig. 1. Cross sections for tritium producing reactions in lithium. ^{7}Li breeds tritium only with high energy neutrons, whereas the cross section for ^{6}Li(n,T)α reactions increases with decreasing neutron energy.

Since 80% of the energy released in DT fusion is carried by the fusion neutron and since efficient tritium breeding is necessary for a self-sufficient fuel cycle, optimal blanket design is a key element in effective fusion reactor design.

1.2 ESSENTIAL ELEMENTS OF THE BLANKET OPTIMIZATION PROBLEM

In the early stages of fusion reactor design, considerable latitude exists in the composition and configuration of the blanket. This is evident in reviewing the variety of designs presented in Refs. 1 and 2. The problem facing the design engineer is how to select the "best" set of blanket design parameters, i.e., the materials, isotopic fractions and geometric factors which define the blanket.

The state of the art in blanket engineering is to develop a point design that meets the system constraints (e.g., tritium breeding ratio greater than one) and then to iterate around that point in an effort to come up with a more attractive design (i.e., improve some figure of merit for the system). These modifications are often directed by intuition and experience, and the final design is not necessarily the most attractive. The optimization problem is complicated by the nonlinear interdependence of design and performance parameters and by the fact that modifications often produce conflicting effects, improving one system parameter while degrading another.

In this research, a methodology has been developed for systematically determining the design parameters that optimize a figure of merit for the reactor. The blanket optimization problem consists of four essential elements:

1. The figure of merit for the particular reactor design,
2. A technique for estimating the neutronic performance as a function of selected design parameters (the independent variables),
3. Constraints on both the design parameters and the neutronic

performance, and

4. A method for optimizing the figure of merit subject to the constraints.

1.2.1 The Figure of Merit.

The figure of merit will depend on the application and design objectives of the particular reactor concept. In fact several different figures of merit may be appropriate for a single concept depending on one's perspective. Consider a fusion electric power plant for example. Minimizing the cost of electricity, minimizing the induced activation and minimizing the plant tritium inventory are each desirable design goals. Fusion-fission hybrids can also have different figures of merit. Some hybrid designs seek to maximize the energy multiplication from fast fission of the fertile material, whereas other concepts seek to suppress fission and maximize the fissile fuel produced per unit of thermal power.[3] In general, the figure of merit can be a function of the design variables themselves (composition and configuration) and the neutronic performance of the reactor which depends on these design variables.

1.2.2 A Technique for Estimating Neutronic Performance.

An important element in the optimization problem is the technique for estimating the neutronic performance of the blanket as a function of the design variables. Neutronic performance refers to the response of the fusion reactor blanket to incident fusion neutrons. In particular, the performance may be characterized by such things as the tritium breeding ratio, the amount of energy deposited as the result of neutron interactions, the neutron damage rate in structural materials and/or the amount of neutron activation.

The objective of a neutronics calculation is to determine the neutronic performance of a reactor blanket with a specific composition and configuration, i.e., a specific set of design parameters. Neutronics calculations for conceptual fusion reactor blankets are carried out with either discrete-ordinate or Monte Carlo neutron transport codes.[10]

In general, optimization algorithms require the evaluation and comparison of the figure of merit at many different points in the search for the most attractive point. In the case of a fusion reactor blanket, an evaluation of the neutronic performance is required each time a new point (i.e., a new set of design parameters) is chosen for comparison. One approach would be to perform a new neutronics calculation for each point requested by the optimization algorithm. While this gives a very accurate evaluation of the neutronic performance and, hence, the figure of merit at the point, the computing time required to perform the neutron transport calculations quickly becomes prohibitive. (For example, a single typical Monte Carlo calculation takes 1-3 minutes of CRAY time. This is ~10 % of daily time allocation (per machine) for the entire Inertial Confinement Fusion Program at Livermore.)

In this research, a variational interpolation method is used to evaluate the neutronic performance.[11,12] With this approach, analytical expressions can be written for the neutronics performance as a function of the design variables based on only a limited number of reference-point, neutron transport calculations. Hence, the figure of merit can be evaluated at any intermediate point without the need for additional transport calculations.

This technique for estimating the neutronics performance as a function of the selected design variables is discussed in Chapter 2.

1.2.3 Constraints on the Design.

Constraints limit the acceptable range from which blanket design variables can be chosen in the attempt to optimize the figure of merit. Constraints can be imposed on design variables, neutronic performance, and factors which depend on the design variables and/or the neutronic performance. An example of the first type of constraint might be a limit on the blanket thickness. Requiring a tritium breeding ratio greater than 1.05 is an example of the second type. A limit on the allowable capital cost of the fusion reactor is an illustration of the third type of constraint.

Clearly the constraints imposed in any optimization problem will be specific to the system being considered. Just as there may be several interesting and appropriate figures of merit, so there may be several different constraints for the same system. That is, it may be desirable to optimize the blanket under the imposition of different constraints and compare the results.

The manner in which constraints are handled in the optimization problem is discussed in Chapter 3.

1.2.4 An Optimization Method.

There is a wide variety of potential methods of optimizing a figure of merit.[13] One of the primary considerations in selecting an appropriate method for the blanket optimization problem is the nonlinearity of the system. The neutronics performance, constraints and figure of merit can all be nonlinear functions of the design variables. Another important consideration is that the form of the

figure of merit may vary from one problem to another. For this reason a general purpose method is desirable, that is, one which is not dependent on the mathematical characteristics of the figure of merit. The nonlinear simplex method of Nelder and Mead[14] was chosen for the blanket optimization problem. According to Walsh,[13] this is one of the most efficient direct search methods available and works particularly well for up to five or six variables. The nonlinear simplex method is described in Chapter 3.

1.3 PREVIOUS FUSION REACTOR OPTIMIZATION STUDIES

Two basic types of fusion reactor optimization studies have been carried out in the past. In the first type, a reactor figure of merit is optimized as a function of the plasma performance, size of the fusion chamber, and/or other plant parameters assuming that the blanket neutronic performance is fixed. In the second type, a neutronic parameter or a reactor figure of merit is optimized as a function of one or more blanket design variables assuming that the plasma performance is fixed. Clearly the subject of this research is of the second type in that variations in neutronic performance as a function of the blanket design are included in evaluating the figure of merit.

References 15-20 are examples of the first type of optimization study. In each case the blanket neutronic performance was fixed or had simple scaling relationships with the parameters being investigated (i.e., in Ref. 18 the fissile-fuel production rate is proportional to the fusion power). In some cases a limited number of different blanket designs are compared, but the neutronic performance of each design is fixed.

In most of the optimization studies of the second type, a new neutron transport calculation is carried out each time the blanket composition and/or configuration is changed in attempting to optimize the chosen figure of merit. Gerstl's blanket and shield optimization was accomplished by this procedure.[21] Abdou investigated options and trade-offs in the nuclear design of the blanket/shield of a Tokamak Experimental Power reactor by comparing the neutronic results

of many different cases.[22] His objective was to minimize the blanket/shield thickness subject to constraints on radiation damage and heating rates in the magnets. The authors of Ref. 23 sought to minimize the peak-to-average fissile fuel production rate across a fuel assembly in the blanket of a fusion-fission hybrid reactor. They did so by comparing this figure of merit for 13 separate cases. In Ref. 24, the cost of electricity from an EBT power plant was evaluated as a function of several blanket design variables. Separate neutronics calculations were carried out for each modification from the baseline case. As one design variable was changed all others were held fixed. Thus, the results show the dependence of the cost of electricity on each variable independently and not as a function of several variables simultaneously. Gohar and Abdou carried out an extensive series of neutronics calculations to define and optimize the neutronic performance of the different solid breeder options for the STARFIRE blanket design.[25] The authors included contour plots of the tritium breeding ratio and heating rates as a function of two variables but did not specify their method. Perkins and Kulcinski reported on the economic optimization of the blanket for the Mirror Advanced Reactor.[26] Their procedure required a neutronics calculation for each iteration in the blanket design.

Some attempts have been made to reduce the number of neutronics calculations required or to automate the iterative process. In their optimization of a magnet shield, Abdou and Maynard used attenuation coefficients to estimate the heating and neutron damage rates in the magnets for various shield designs.[27] The authors of Ref. 28 studied the optimization of a Tokamak reactor. They estimated nuclear

reaction rates and heating rates by an analytical expression involving a leading coefficient plus a sum of exponential terms related to the thickness of various blanket zones. According to their report, only a limited number of neutron transport calculations were required to determine the coefficients of their expression. Engle and Mynatt automated their shield optimization problem by incorporating the transport calculations in the optimization process.[29] Each boundary is varied twice, and a separate neutronics calculation carried out at each position. From these results, the dose-weight derivatives are determined and used to modify the shield configuration in an effort to optimize the design.

Schwartz proposed a method to optimize an economic figure of merit for a fusion-fission hybrid.[30] Starting from a reference point, each design variable was changed while holding the others fixed. Neutronics calculations were carried out at each point and the partial derivatives approximated by the finite differences. The economic figure of merit was then expressed in terms of the first order Taylor series expansions. A gradient projection algorithm was used to optimize the design.

Greenspan has developed a method for optimizing a neutronic characteristic of the blanket by varying the distribution of materials within the blanket.[31,32] It can also be used to minimize a blanket characteristic such as total cost, weight or volume. His method is based on a variational technique which uses both forward and adjoint flux calculations. Each iteration requires two transport calculations, one forward and one adjoint, and determines a new material distribution which improves the neutronic characteristic of

interest. The method can optimize a single characteristic subject to a single constraint. It is not applicable to problems involving the optimization of broader system parameters such as the cost of electricity.

In this research, a variational interpolation method is used to estimate the neutronic performance as a function of more than one variable simultaneously. The method provides analytical expressions for the neutronic characteristics as a function of the blanket design variables based on a limited number of neutron transport calculations. This is the subject of Chapter 2.

1.4 ORGANIZATION OF THE THESIS

The remainder of this thesis is divided into five chapters. The variational interpolation method, and how it is used to make multivariable estimates of the neutronic performance, is described in Chapter 2. The nonlinear simplex optimization method which is used to locate the optimal design point is discussed in Chapter 3. The techniques developed in Chapters 2 and 3 are applied in Chapters 4 and 5. In Chapter 4, the design of an Inertial Confinement Fusion (ICF) reactor with a liquid lithium breeding blanket is optimized. The second optimization problem, discussed in Chapter 5, is also for an ICF reactor. In this case, however, the blanket contains a solid lithium compound for tritium breeding. Conclusions and suggestions for future work are given in Chapter 6.

2. ESTIMATING NEUTRONIC PERFORMANCE

In this chapter the technique used to estimate the neutronic performance as a function of the design variables is described. The heart of the technique is the variational interpolation method described by Cheng and Conn.[11,12] Variational interpolation is a particular application of a broader category of variational methods. Background information and related applications are discussed in Refs. 33-38 and references cited in these papers.

2.1 VARIATIONAL ESTIMATES OF LINEAR FUNCTIONALS

In the study of the neutronics of fusion reactor blankets, one is primarily interested in integral properties which can be written as linear functionals of the neutron flux. Examples include tritium production, nuclear heating, displacement damage, He and H production, and neutron activation rates. Consider for example a reaction rate, R. The reaction rate can be expressed as the inner product of the macroscopic reaction cross section and the neutron flux distribution,[37]

$$R = \langle \Sigma, \phi \rangle. \tag{2.1}$$

The inner product notation $\langle\ \rangle$ indicates a sum over all discrete independent variables (e.g., various regions of the blanket) and an integral over all continuous independent variables (e.g., space,

energy, and direction).

The neutron flux, ϕ, is the solution to the time independent Boltzmann transport equation,[39]

$$L\phi = S, \tag{2.2}$$

where

L = Transport operator such that

$$L\phi = \underline{\Omega}\cdot\underline{\nabla}\phi + \Sigma_T\phi - \int_{\underline{\Omega}'}\int_{E'}\Sigma_T f\phi \, d\underline{\Omega}'dE',$$

$\phi = \phi(\underline{r},\underline{\Omega},E)$ the angular flux distribution at position $\underline{r}$, direction $\underline{\Omega}$ and energy E,

$\Sigma_T = \Sigma_T(\underline{r},E)$ the total macroscopic cross section,

$f = f(\underline{r},\underline{\Omega}' \rightarrow \underline{\Omega},E' \rightarrow E)$ is the transfer probability function such that $\Sigma_T(\underline{r},E')f$ is the transfer kernal for neutron transfer from $\underline{\Omega}'$, E' to $\underline{\Omega}$, E, and

$S = S(\underline{r},\underline{\Omega},E)$ is the external or independent neutron source.

Let x be a variable that characterizes the blanket. The reaction rate, $R(x)$, can be estimated using the flux, ϕ_a, calculated for some reference system, $x = x_a$, in several ways. If we define

$$\delta\phi_a \equiv \phi - \phi_a, \tag{2.3}$$

then

$$R(x) = \langle\Sigma,\phi\rangle = \langle\Sigma,\phi_a\rangle + \langle\Sigma,\delta\phi_a\rangle. \tag{2.4}$$

The estimate,

$$R(x) \simeq \langle \Sigma, \phi_a \rangle, \tag{2.5}$$

is therefore in error to first order in $\delta\phi_a$.

A variational estimate of R yields a result accurate to second order[37] in $\delta\phi_a$ and $\delta\phi_a^*$, where

$$\delta\phi_a^* = \phi^* - \phi_a^*. \tag{2.6}$$

The adjoint flux, ϕ^*, is the solution to

$$L^*\phi^* = S^*, \tag{2.7}$$

where the adjoint operator, L*, is defined by[39]

$$\langle \phi^*, L\phi \rangle = \langle L^*\phi^*, \phi \rangle. \tag{2.8}$$

Consider for example the Roussopoulos functional defined by:[7,10]

$$R_R(\phi_a^*, \phi_a; x) = \langle S^*(x), \phi_a \rangle + \langle \phi_a^*, S(x) - L(x)\phi_a \rangle. \tag{2.9}$$

In order to give this physical significance, let $S^* = \Sigma$ so that the adjoint flux can be related to the reaction rate by

$$\langle L^*\phi^*, \phi \rangle = \langle S^*, \phi \rangle = \langle \Sigma, \phi \rangle = R. \tag{2.10}$$

Using Eqs. 2.3, 2.6, and 2.10 in Eq. 2.9 gives

$$R_R = \langle \Sigma, \phi - \delta\phi_a \rangle + \langle \phi^* - \delta\phi_a^*, S - L(\phi - \delta\phi_a) \rangle. \tag{2.11}$$

Expanding gives

$$R_R = \langle \Sigma, \phi \rangle - \langle \Sigma, \delta\phi_a \rangle + \langle \phi^* - \delta\phi_a^*, S - L\phi + L\delta\phi_a \rangle. \tag{2.12}$$

Noting from Eq. 2.2 that $S - L\phi = 0$, Eq. 2.12 becomes

$$R_R = \langle \Sigma, \phi \rangle - \langle \Sigma, \delta\phi_a \rangle + \langle \phi^*, L\delta\phi_a \rangle - \langle \delta\phi_a^*, L\delta\phi_a \rangle. \tag{2.13}$$

Note that using Eqs. 2.8 and 2.7 along with the fact that $S^* = \Sigma$, the third term can be written as

$$\langle \phi^*, L\delta\phi_a \rangle = \langle L^* \phi^*, \delta\phi_a \rangle = \langle \Sigma, \delta\phi_a \rangle. \tag{2.14}$$

Hence the second and third terms of Eq. 2.13 cancel, and we are left with

$$R_R = \langle \Sigma, \phi \rangle - \langle \delta\phi_a^*, L\delta\phi_a \rangle. \tag{2.15}$$

This demonstrates that the variational estimate, Eq. 2.9, provides a result accurate to second order in $\delta\phi_a$ and $\delta\phi_a^*$ as previously stated.

The variational interpolation method of estimating R is derived from the Schwinger (fractional) functional,[2]

$$R_S(\phi_a^*,\phi_a;x) = \langle\phi_a^*,S(x)\rangle\langle\Sigma(x),\phi_a\rangle/\langle\phi_a^*,L(x)\phi_a\rangle. \tag{2.16}$$

The Schwinger functional is derived from the Roussopoulos functional as follows. First, two scale factors are defined for ϕ_a^*, and ϕ_a, respectively,[37]

$$C^* \equiv \langle\Sigma,\phi_a\rangle/\langle\phi_a^*,L\phi_a\rangle, \tag{2.17}$$

and

$$C \equiv \langle\phi_a^*,S\rangle/\langle\phi_a^*,L\phi_a\rangle. \tag{2.18}$$

The Roussopoulos functional, Eq. 2.9, for $C^*\phi_a^*$ and $C\phi_a$ becomes

$$R_R(C^*\phi_a^*,C\phi_a;x) = \langle\Sigma(x),C\phi_a\rangle + \langle C^*\phi_a^*,S(x)\rangle - \langle C^*\phi_a^*,L(x)C\phi_a\rangle. \tag{2.19}$$

Substituting Eqs. 2.17 and 2.18 gives

$$\begin{aligned} R_R = {} & \langle\Sigma,\phi_a\rangle\langle\phi_a^*,S\rangle/\langle\phi_a^*,L\phi_a\rangle + \langle\phi_a^*,S\rangle\langle\Sigma,\phi_a\rangle/\langle\phi_a^*,L\phi_a\rangle \\ & - \langle\phi_a^*,L\phi_a\rangle\langle\Sigma,\phi_a\rangle\langle\phi_a^*,S\rangle/\langle\phi_a^*,L\phi_a\rangle\langle\phi_a^*,L\phi_a\rangle. \end{aligned} \tag{2.20}$$

Cancelling a $\langle\phi_a^*,L\phi_a\rangle$ term in the numerator and denominator of the third term of Eq. 2.20 reveals that the third term is just the negative of the first term. Hence Eq. 2.20 reduces to

$$R_R = \langle\phi_a^*,S\rangle\langle\Sigma,\phi_a\rangle/\langle\phi_a^*,L\phi_a\rangle, \tag{2.21}$$

which is Eq. 2.16. That is,

$$R_S(\phi_a^*,\phi_a;x) = R_R(C^*\phi_a^*,C\phi_a;x). \tag{2.22}$$

2.2 TWO POINT VARIATIONAL INTERPOLATION FOR FUSION REACTORS

2.2.1 Two Point Variational Interpolation In Terms of Forward Fluxes.

In this section, the two point variational interpolation formula is discussed, and an expression in terms of the forward fluxes at $x = x_a$ and $x = x_b$ is derived. The advantages of this formulation have been pointed out by Cheng.[11] In particular since only forward fluxes are involved (ϕ_a and ϕ_b) no adjoint calculations are required. Calculating ϕ_a and ϕ_b allows one to interpolate in x on the functional $\langle \Sigma(x), \phi \rangle$ for any $\Sigma(x)$. That is, estimates of several different reaction rates, damage rates, etc., can be made based on the results of two transport calculations. This is in contrast to Eq. 2.23 (below) where an adjoint calculation is required for each $\Sigma(x)$ (i.e., S^*) of interest as indicated by Eq. 2.7.

The interpolation form of Eq. 2.16 uses the forward flux calculated at $x = x_a$ and the adjoint flux calculated at a different reference point, $x = x_b$. It is given by,[11]

$$R_{SI}(\phi_b^*, \phi_a; x) = \langle \phi_b^*, S(x) \rangle \langle \Sigma(x), \phi_a \rangle / \langle \phi_b^*, L(x) \phi_a \rangle . \qquad (2.23)$$

For a fusion reactor blanket the external neutron source is fixed in most cases of interest (i.e., a fixed fusion power level). Therefore,

$$L(x_a)\phi_a = L(x_b)\phi_b = S = \text{constant}. \qquad (2.24)$$

If the perturbation is linear in x, then L(x) can be written as

$$L(x) = L(x_a) + \delta L(x), \tag{2.25}$$

where

$$\delta L(x) = [(x-x_a)/(x_b-x_a)][L(x_b) - L(x_a)].$$

By substituting Eq. 2.25 into Eq 2.23 and using Eqs. 2.8 and 2.24, the variational interpolation formula can be written in terms of forward fluxes only. Consider the first term in the numerator of Eq. 2.23. Using Eq. 2.24 it can be written as

$$\langle \phi_b^*, S(x) \rangle = \langle \phi_b^*, L(x_b)\phi_b \rangle. \tag{2.26}$$

Then using Eq. 2.8,

$$\langle \phi_b^*, S(x) \rangle = \langle L^*(x_b)\phi_b^*, \phi_b \rangle. \tag{2.27}$$

Using the fact that $L^*\phi^* = S^* = \Sigma$, gives

$$\langle \phi_b^*, S(x) \rangle = \langle \Sigma(x_b), \phi_b \rangle \tag{2.28}$$

Next consider the denominator of Eq. 2.23. First substitute Eq. 2.25,

$$\langle \phi_b^*, L(x)\phi_a \rangle = \langle \phi_b^*, [L_a + [(x-x_a)/(x_b-x_a)](L_b-L_a)]\phi_a \rangle, \tag{2.29}$$

where the notation $L_a = L(x_a)$ and $L_b = L(x_b)$ has been used. Expanding the right hand side of Eq. 2.29 gives

$$\langle\phi_b^*, L_a\phi_a\rangle + [(x-x_a)/(x_b-x_a)][\langle\phi_b^*, L_b\phi_a\rangle - \langle\phi_b^*, L_a\phi_a\rangle]. \tag{2.30}$$

Using Eqs. 2.24 and 2.8 this becomes

$$\langle L_b^*\phi_b^*, \phi_b\rangle + [(x-x_a)/(x_b-x_a)][\langle L_b^*\phi_b^*, \phi_a\rangle - \langle L_b^*\phi_b^*, \phi_b\rangle], \tag{2.31}$$

or

$$\langle\Sigma(x_b), \phi_b\rangle + [(x-x_a)/(x_b-x_a)][\langle\Sigma(x_b), \phi_a\rangle - \langle\Sigma(x_b), \phi_b\rangle]. \tag{2.32}$$

Substituting Eqs. 2.28 and 2.32 into Eq. 2.23 gives an interpolation formula in terms of the forward fluxes ϕ_a and ϕ_b,

$$R_{SI}(\phi_b, \phi_a; x) = \langle\Sigma(x), \phi_a\rangle\langle\Sigma_b, \phi_b\rangle/D, \tag{2.33}$$

where

$$D = \langle\Sigma_b, \phi_b\rangle + [(x-x_a)/(x_b-x_a)][\langle\Sigma_b, \phi_a\rangle - \langle\Sigma_b, \phi_b\rangle].$$

Here the notation $\Sigma(x_a) = \Sigma_a$ and $\Sigma(x_b) = \Sigma_b$ has been used. Note that at $x = x_a$, $R_{SI} = \langle\Sigma_a, \phi_a\rangle$, and at $x = x_b$, $R_{SI} = \langle\Sigma_b, \phi_b\rangle$. Hence, Eq. 2.33 provides the exact solution at the two reference points and an estimate for other values of x. (Exact means the same result as from the transport calculation.) It has been shown that for $x_a < x < x_b$ variational interpolation relies on cancellation of error.[11] That is, as x approaches x_b from x_a, $\delta\phi_a$ is growing while $\delta\phi_b$ is tending

to zero. For values of x that do not lie between x_a and x_b both $\delta\phi_a$ and $\delta\phi_b$ increase as the distance from the reference point increases. Therefore, great accuracy is not expected in using Eq. 2.33 to extrapolate.

The magnitude of the error will depend both on the proximity of the reference points and on the sensitivity of the reaction rate to the design variable. In general, the farther apart x_a and x_b are, the greater the error in the estimated value of R at intermediate values of x will be. Also, if R is very sensitive to x, the error will be larger than if R is a weak function of x. To determine what the error actually is requires a transport calculation at the intermediate point of interest.

2.2.2 Variational Interpolation for Variations in Blanket Composition.

Of particular interest in the study of fusion reactor blankets, is how reaction rates change as the isotopic composition of the blanket (or a region of the blanket) is changed. For reactions with isotope-j, the macroscopic cross-section is

$$\Sigma_j = N_j\sigma_j = f_j\rho N_o\sigma_j/M, \tag{2.34}$$

where

f_j = atom fraction of isotope-j in the blanket material,

N_j = number density of isotope-j,

σ_j = microscopic reaction cross section with isotope-j,

ρ = material density,

N_o = Avagadro's number, and

M = effective atomic weight of the material.

To investigate the effects of varying the fraction of isotope-j in the blanket, x is set equal to f; hence, the macroscopic cross-sections for reactions with isotope-j are proportional to x. As a result, varying x gives a linear perturbation in L and Eq. 2.33 can thus be applied.

In this case, Eq. 2.33 can be simplified by noting that

$$\Sigma(x) = x\Sigma_a/x_a. \tag{2.35}$$

Substituting gives

$$R_{SI}(\phi_b,\phi_a;x) = (x/x_a)\langle\Sigma_a,\phi_a\rangle\langle\Sigma_b,\phi_b\rangle/D, \tag{2.36}$$

where

$$D = \langle\Sigma_b,\phi_b\rangle + [(x-x_a)/(x_b-x_a)][(x_b/x_a)\langle\Sigma_a,\phi_a\rangle - \langle\Sigma_b,\phi_b\rangle].$$

In terms of the reaction rates obtained from the transport calculations at the two reference points, i.e.,

$$R_a = \langle\Sigma_a,\phi_a\rangle,$$

and (2.37)

$$R_b = \langle\Sigma_b,\phi_b\rangle,$$

Eq. 2.36 becomes

$$R_{SI}(R_a,R_b;x) = (x/x_a)R_aR_b/D, \tag{2.38}$$

where

$$D = R_b + [(x-x_a)/(x_b-x_a)][(x_b/x_a)R_a - R_b].$$

Equation 2.38 is exact at $x = x_a$ and $x = x_b$ and gives a nonlinear interpolation for intermediate values of x. That is, $R_{SI} = R_a$ at $x = x_a$, and $R_{SI} = R_b$ at $x = x_b$. Also note that since $\Sigma(x)$ is proportional to x, $R = 0$ at $x = 0$, and in this case Eq. 2.38 is also exact at $x = 0$.

To illustrate the nature of Eq. 2.38, two cases are shown in Fig. 2.1; the lower curve has reference values $R(0.2) = 0.5$ and $R(0.6) = 3.0$ while the upper curve is for $R(0.2) = 2.0$ and $R(0.6) = 3.0$. The units are arbitrary.

2.2.3 Singularities of the Two Point Interpolation Formula.

Equation 2.38 has a singularity when $D = 0$. Setting $D = 0$ and solving for the location of the singularity, x_s, gives

$$x_s = x_a - (x_b - x_a)R_b/[(x_b/x_a)R_a - R_b]. \qquad (2.39)$$

This is of concern only if $x_s \geq 0$ (since negative atom fractions are meaningless) which occurs if $R_a \geq R_b$, assuming $a < b$. For $R_a < R_b$, Eq. 2.38 is well behaved and gives a nonlinear estimate of R(x) which is monotonically increasing with x. If the reference point calculations give $R_a \geq R_b$, then Eq. 2.38 is inadequate. In this case a 3-point variational interpolation formulation may be useful. The 3-point interpolation formula is developed later in this chapter.

In the case where the blanket is composed of only two isotopes the atom fraction of each is related to x by

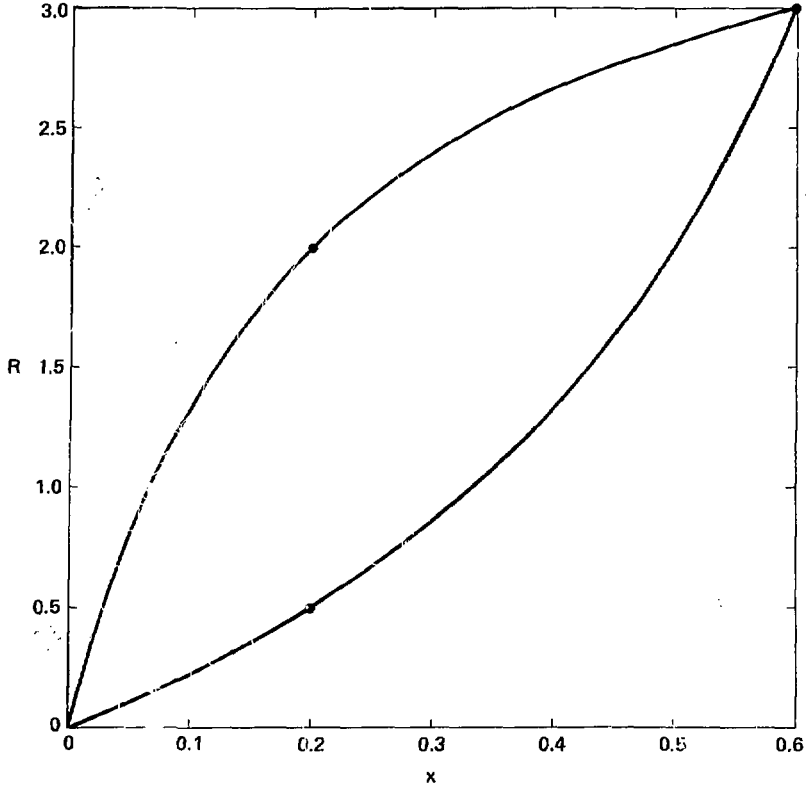

Fig. 2.1 Illustrative examples of two point variational interpolation when $\Sigma(x)$ is proportional to x (Eq. 2.38). The reference points for the lower curve are $R(0.2) = 0.5$ and $R(0.6) = 3.0$. The upper curve has reference points $R(0.2) = 2.0$ and $R(0.6) = 3.0$.

$$f_1 = x,$$

and (2.40)

$$f_2 = 1 - x.$$

Then for isotope-2, Eq. 2.35 becomes

$$\Sigma(x) = (1-x)\Sigma_a/(1-x_a), \tag{2.41}$$

and Eq. 2.38 becomes

$$R_{SI2}(R_a,R_b;x) = (1-x)R_aR_b/[(1-x_a)D], \tag{2.42}$$

where

$$D = R_b + [(x-x_a)/(x_b-x_a)][(1-x_b)R_a/(1-x_a) - R_b].$$

Note that R_a and R_b are the reaction rates with isotope-2 derived from the reference point calculations at $x = x_a$ and $x = x_b$, respectively. For isotope-2, Eq. 2.42 is exact at $x = x_a$, $x = x_b$ and also at $x = 1$. It is not exact at $x = 0$.

To summarize, in the case of blanket composed of only two isotopes where the design variable of interest is the atom fraction of the first isotope, the two point variational interpolation formula gives exact values for reaction rates with isotope-1 at $x = 0$, x_a and x_b, and gives exact values for reaction rates with isotope-2 at $x = x_a$, x_b and 1.

If the atom fraction of an isotope is unaffected by the variation of x, then

$$\Sigma(x) = \Sigma_a = \Sigma_b = \text{constant}. \tag{2.43}$$

In this case Eq. 2.33 becomes

$$R_{SIC}(R_a,R_b;x) = R_aR_b/D, \tag{2.44}$$

where

$$D = R_b + [(x-x_a)/(x_b-x_a)][R_a - R_b].$$

One example where this holds is in a blanket containing 3 or more isotopes with one or more specified as constant. In particular, 3 isotopes could be specified as $f_1 = x$, $f_2 = 1 - C - x$, and $f_3 = C$ = constant. Another example where Eq. 2.44 holds is in regions of the blanket other than the region where x is varied. In these cases, the variational estimate reflects the change in the flux due to a change in x.

Generalizing Eqs. 2.38, 2.42, and 2.44, the two point variational interpolation formula becomes

$$R_{S1}(R_a,R_b;x) = (\Sigma(x)/\Sigma_a)R_aR_b/D, \tag{2.45}$$

where

$$D = R_b + [(x-x_a)/(x_b-x_a)][(\Sigma_b/\Sigma_a)R_a - R_b].$$

2.2.4 Multivariable Estimates Using Two Point Variational Interpolation.

The previous section shows how variational interpolation can be used to estimate neutronic characteristics as a function of a single design variable. In practice it is desirable to evaluate the effects of variations in several design variables simultaneously. By successive application of the variational interpolation procedure discussed in the previous section, one can estimate the neutronic

characteristics of interest at any point in an n-dimensional space, based on a limited number of reference point transport calculations.

Consider the problem of estimating reaction rates as a function of two design variables x_1 and x_2. To do this using the variational interpolation scheme requires four reference point transport calculations. These four points are most conveniently chosen to define a rectangle in Cartesian coordinates as shown in Fig. 2.2. The reference points are denoted (x_{1a},x_{2a}), (x_{1b},x_{2a}), (x_{1a},x_{2b}) and (x_{1b},x_{2b}). The corresponding reaction rates at these four points are denoted R_{aa}, R_{ba}, R_{ab} and R_{bb}, respectively.

The procedure used to estimate the reaction rate at some point (x_{1d},x_{2d}) is illustrated in Fig. 2.3. First, the result R_{da} is found by interpolating on x_1 with $x_2 = x_{2a}$. Next, the result R_{db} is found by interpolating on x_1 with $x_2 = x_{2b}$. The two results are then used to interpolate on x_2 with $x_1 = x_{1d}$, to find the result R_{dd}. As such, 3 interpolations are required to estimate the reaction rate.

In terms of the previous expressions for Schwinger Interpolation, the successive interpolation approach can be written as

$$R_{SSI}(R_{aa},R_{ba},R_{ab},R_{bb};x_1,x_2) = R_{SI}(R_{SI}(R_{aa},R_{ba};x_1),\ R_{SI}(R_{ab},R_{bb};x_1);x_2) \qquad (2.46)$$

(Clearly one could just as easily interpolate on x_2 first and then on x_1).

To extend the approach to a third variable, x_3, requires four additional reference point transport calculations. Assuming the first

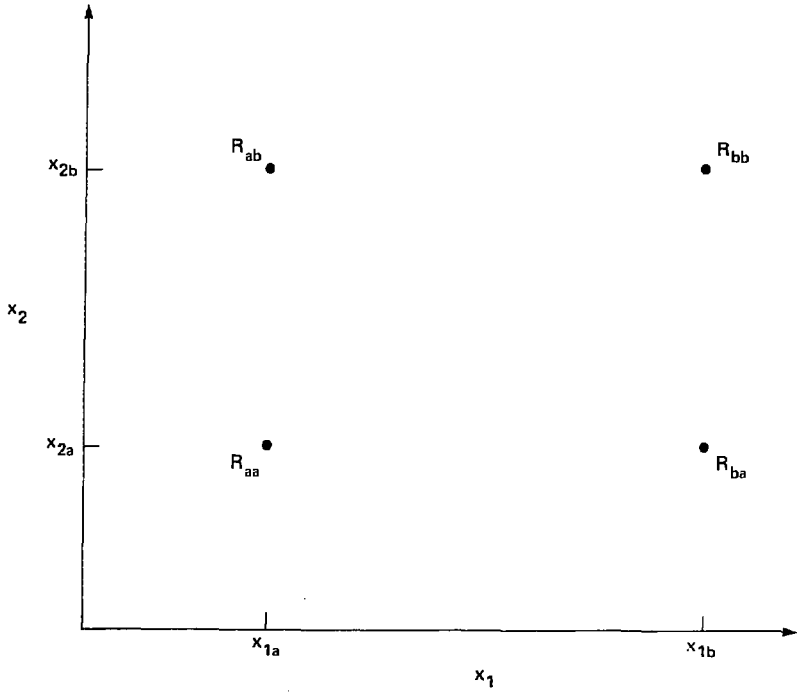

Fig. 2.2 Location of four reference points for two point interpolation on two variables. Neutron transport calculations are carried out at these four points. The resulting reaction rates are denoted by R with two subscripts corresponding to the x_1 and x_2 coordinates, respectively.

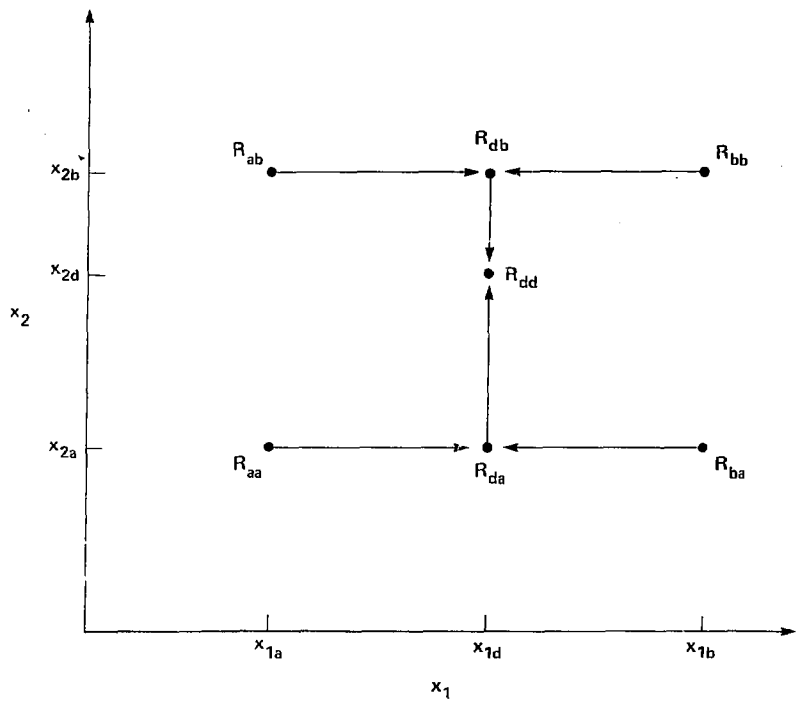

Fig. 2.3 Successive two point variational interpolation. To find the reaction rate at the point (x_{1d}, x_{2d}) requires three interpolations; one to find R_{da}, a second to find R_{db}, and a third to find R_{dd}.

four are in the plane $x_3 = x_{3a}$, the four additional points would be in the plane $x_3 = x_{3b}$. Applying Eq. 2.46 in the plane $x_3 = x_{3a}$ gives the result R_{dda}. A second application of Eq. 2.46 with $x_3 = x_{3b}$ gives R_{ddb}. These are then used to interpolate on x_3 to give the desired result R_{ddd}. In this case a total of 7 interpolations are required.

Generalizing, in order to span n-space with this technique requires 2^n reference point transport calculations and (2^n-1) successive interpolations for each reaction of interest at each point of interest.

2.3 THREE POINT VARIATIONAL INTERPOLATION FOR FUSION REACTORS

The three point variational interpolation formula based on the Schwinger functional is given by,[11]

$$R_{SI3}(\phi_a,\phi_b,\phi_c^*;x) = \langle\Sigma(x),\phi_a\rangle + \langle\phi_c^*,S(x)-L(x)\phi_a\rangle\langle\Sigma(x),\phi_b-\phi_a\rangle/\langle\phi_c^*,L(x)(\phi_b-\phi_a)\rangle \quad (2.47)$$

where $S^*(x)$ has been set equal to $\Sigma(x)$. The subscripts a, b and c refer to conditions at $x = x_a$, $x = x_b$ and $x = x_c$, respectively, where $x_a < x_b < x_c$.

2.3.1 Three Point Variational Interpolation In Terms of Forward Fluxes.

For a fixed external source and linear perturbations, a formula in terms of forward fluxes only can be derived. For a fixed external source,

$$L_a\phi_a = L_b\phi_b = L_c\phi_c = S = \text{constant}. \quad (2.48)$$

If the perturbation is linear in x, then L(x) can be written as

$$L(x) = L_a + \lambda_{ca}(L_c-L_a), \quad (2.49)$$

where

$$\lambda_{ca} = (x-x_a)/(x_c-x_a),$$

or as,

$$L(x) = L_b + \lambda_{cb}(L_c-L_b), \quad (2.50)$$

where

$$\lambda_{cb} = (x-x_b)/(x_c-x_b).$$

Consider the term,

$$\langle \phi_c^*, S(x) - L(x)\phi_a \rangle \tag{2.51}$$

in the numerator of the second term in Eq. 2.47. Substituting Eqs. 2.48 and 2.49 and expanding gives

$$\langle \phi_c^*, L_c\phi_c \rangle - \langle \phi_c^*, L_a\phi_a \rangle - \lambda_{ca}\langle \phi_c^*, (L_c - L_a)\phi_a \rangle. \tag{2.52}$$

Noting that the first two terms of (2.52) cancel, we are left with,

$$- \lambda_{ca}[\langle \phi_c^*, L_c\phi_a \rangle - \langle \phi_c^*, L_a\phi_a \rangle]. \tag{2.53}$$

Using Eqs. 2.8 and 2.48 this can be rewritten as,

$$- \lambda_{ca}[\langle L_c^*\phi_c^*, \phi_a \rangle - \langle \phi_c^*, L_c\phi_c \rangle]. \tag{2.54}$$

Using Eq. 2.8 again gives,

$$- \lambda_{ca}[\langle \Sigma_c, \phi_a \rangle - \langle \Sigma_c, \phi_c \rangle]. \tag{2.55}$$

Hence, ϕ_c^* has been eliminated from this term.

Next, consider the denominator of the second term in Eq. 2.47,

$$\langle \phi_c^*, L(x)(\phi_b - \phi_a) \rangle. \tag{2.56}$$

Expanding gives,

$$\langle\phi_c^*, L(x)\phi_b\rangle - \langle\phi_c^*, L(x)\phi_a\rangle. \tag{2.57}$$

Using Eq. 2.50, the first term of (2.57) becomes,

$$\langle\phi_c^*, L_b\phi_b\rangle + \lambda_{cb}\langle\phi_c^*, (L_c - L_b)\phi_b\rangle. \tag{2.58}$$

Using Eqs. 2.8 and 2.48 gives,

$$\langle\phi_c^*, L_c\phi_c\rangle + \lambda_{cb}[\langle L_c^*\phi_c^*, \phi_b\rangle - \langle\phi_c^*, L_c\phi_c\rangle], \tag{2.59}$$

and then

$$\langle\Sigma_c, \phi_c\rangle + \lambda_{cb}[\langle\Sigma_c, \phi_b\rangle - \langle\Sigma_c, \phi_c\rangle]. \tag{2.60}$$

Similarly the second term of (2.57) reduces to

$$-\langle\Sigma_c, \phi_c\rangle - \lambda_{ca}[\langle\Sigma_c, \phi_a\rangle - \langle\Sigma_c, \phi_c\rangle]. \tag{2.61}$$

Using Eqs. 2.49, 2.50, 2.55, 2.60, and 2.61, Eq. 2.47 can be written as

$$R_{SI3}(\phi_a, \phi_b, \phi_c; x) = \langle\Sigma(x), \phi_a\rangle \tag{2.62}$$
$$- [(x-x_a)/(x_c-x_a)][\langle\Sigma_c, \phi_a\rangle - \langle\Sigma_c, \phi_c\rangle]\langle\Sigma(x), \phi_b-\phi_a\rangle/D,$$

where

$$D = [(x-x_b)/(x_c-x_b)][\langle\Sigma_c, \phi_b\rangle - \langle\Sigma_c, \phi_c\rangle]$$
$$- [(x-x_a)/(x_c-x_a)][\langle\Sigma_c, \phi_a\rangle - \langle\Sigma_c, \phi_c\rangle].$$

In terms of the reaction rates at the reference points

$$\begin{aligned} R_a &= \langle \Sigma_a, \phi_a \rangle, \\ R_b &= \langle \Sigma_b, \phi_b \rangle, \text{ and} \\ R_c &= \langle \Sigma_c, \phi_c \rangle, \end{aligned} \tag{2.63}$$

Eq. 2.62 becomes,

$$\begin{aligned} R_{SI3}(R_a, R_b, R_c; x) &= (\Sigma(x)/\Sigma_a)R_a \\ &- [(x-x_a)/(x_c-x_a)][(\Sigma_c/\Sigma_a)R_a - R_c][(\Sigma(x)/\Sigma_b)R_b - (\Sigma(x)/\Sigma_a)R_a]/D, \end{aligned} \tag{2.64}$$

where

$$\begin{aligned} D = {} & [(x-x_b)/(x_c-x_b)][(\Sigma_c/\Sigma_b)R_b - R_c] \\ & - [(x-x_a)/(x_c-x_a)][(\Sigma_c/\Sigma_a)R_a - R_c]. \end{aligned}$$

Note that Eq. 2.64 is exact at $x = x_a$, x_b and x_c giving the results R_a, R_b and R_c, respectively.

2.3.2 Singularities of the Three Point Interpolation Formula.

This three point interpolation formula has singularities when the denominator of Eq. 2.64 equals zero. This occurs when

$$[(x-x_b)/(x_c-x_b)][(\Sigma_c/\Sigma_b)R_b - R_c] = [(x-x_a)/(x_c-x_a)][(\Sigma_c/\Sigma_a)R_a - R_c]. \tag{2.65}$$

The value of x at which Eq. 2.65 holds is,

$$x_s = \{x_b[(\Sigma_c/\Sigma_b)R_b - R_c]/(x_c-x_b) - x_a[(\Sigma_c/\Sigma_a)R_a - R_c]/(x_c-x_a)\}/D, \tag{2.66}$$

where

$$D = [(\Sigma_c/\Sigma_b)R_b - R_c]/(x_c - x_b) - [(\Sigma_c/\Sigma_a)R_a - R_c]/(x_c - x_a).$$

For the case where $\Sigma(x)$ is proportional to x, i.e., $\Sigma_c/\Sigma_a = x_c/x_a$ and $\Sigma_c/\Sigma_b = x_b/x_a$, Eq. 2.66 reduces to

$$x_s = \{(x_c R_b - x_b R_c)/(x_c - x_b) - (x_c R_a - x_a R_c)/(x_c - x_a)\}/D, \qquad (2.67)$$

where

$$D = (x_c R_b - x_b R_c)/[(x_c - x_b)x_b] - (x_c R_a - x_a R_c)/[(x_c - x_a)x_a].$$

In using the three point interpolation one must check to see if the singularity lies in the range of interest. Consider a specific example where

$$R_a = 2.0 \text{ at } x_a = 0.2,$$

and

$$R_c = 3.0 \text{ at } x_c = 0.6.$$

Figure 2.4 shows the location of the singularity, x_s, as a function of the reaction rate, R_b, at $x_b = 0.4$. If $R_b \leq 2.5$, there is a singularity between 0 and 0.[illegible] If $R_b \geq 4.0$, there is a singularity at a point less than 0.60. Hence, Eq. 2.63 can be used to interpolate between 0.2 and 0.6 and extrapolate down to x = 0 only if $2.5 < R_b < 4.0$.

The envelope of the family of curves which the three point interpolation can fit through the points R(0.2) = 2.0 and R(0.6) = 3.0 is shown in Fig. 2.5. Note that, unlike the two point interpolation, the three point interpolation can generate a curve which goes through

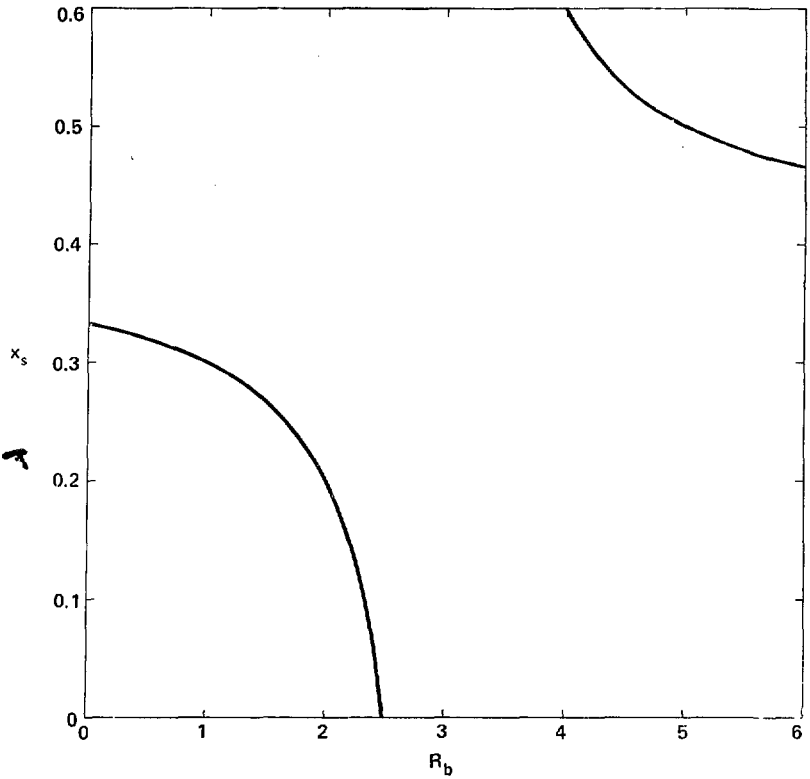

Fig. 2.4 Location of singularity for three point interpolation versus R_b for a curve with negative second derivatives. The reference point results are $R_a(0.2) = 2.0$ and $R_c(0.6) = 3.0$. If the result R_b at $x_b = 0.4$ is not between 2.5 and 4.0, the location of the singularity, x_b, will lie in the range of interest, $0 \leq x \leq 0.6$.

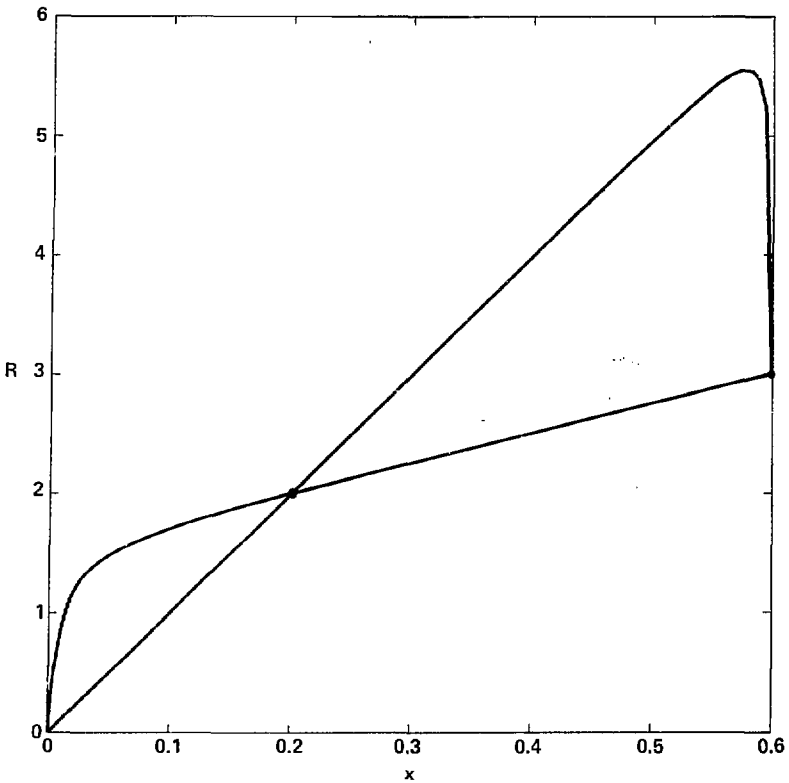

Fig. 2.5 Envelope of family of curves with three point interpolation for R(0.2) = 2.0 and R(0.6) = 3.0. Compare to the upper curve in Fig. 2.1 obtained with two point interpolation.

a maximum. Figure 2.5 should be compared to the upper curve in Fig. 2.1.

Figures 2.4 and 2.5 illustrate the nature of the three point interpolation for $R_a/x_a > R_c/x_c$, i.e., curves which are concave down. Now consider the opposite case where $R_a/x_a < R_c/x_c$. Let

$$R_a = 0.5 \text{ at } x_a = 0.2,$$

and

$$R_c = 3.0 \text{ at } x_c = 0.6.$$

Figure 2.6 shows the location of the singularity as a function of R_b, where $x_b = 0.4$ as before. In this case R_b is limited to values between 1.0 and 1.75 in order to avoid singularity in the range $0 \leq x \leq 0.6$.

Figure 2.7 shows the envelope of the family of curves obtained for $1.0 < R_b < 1.75$. Here we see another limitation of the three point interpolation. If the formula is used to extrapolate between 0.2 and 0, negative reaction rates are predicted. Obviously this is meaningless. In order to assure that $R > 0$ in the extrapolated region, the derivative of Eq. 2.64 as x approaches zero must be ≥ 0. The derivative of Eq. 2.64 for the case of $\Sigma(x) = x\Sigma_a/x_a = x\Sigma_b/x_b$ and the limit as x approaches zero is given in Appendix I. For this specific example (i.e., $R(0.2) = 0.5$ and $R(0.6) = 3.0$) the condition $R_b \leq 1.6$ is required to prevent negative values of R near $x = 0$. The revised envelope of possible curves is shown in Fig. 2.8. See the lower curve of Fig. 2.1 for comparison.

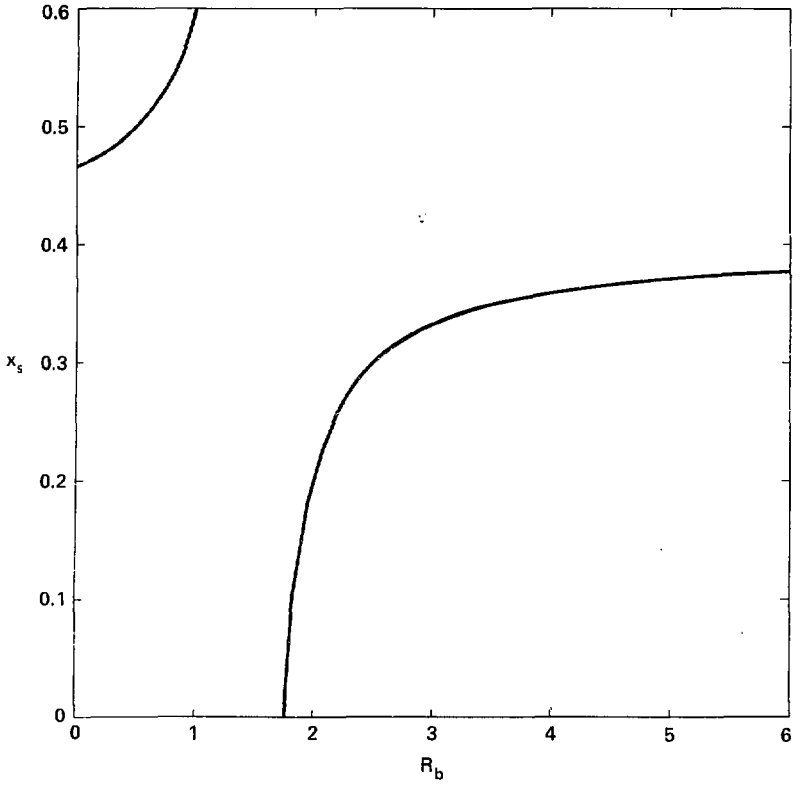

Fig. 2.6 Location of singularity for three point interpolation versus R_b for a curve with positive second derivatives. The reference point results are $R_a(0.2) = 0.5$ and $R_c(0.6) = 3.0$. If the result R_b at $x_b = 0.4$ is not between 1.0 and 1.75, the location of the singularity, x_b, will lie in the range of interest.

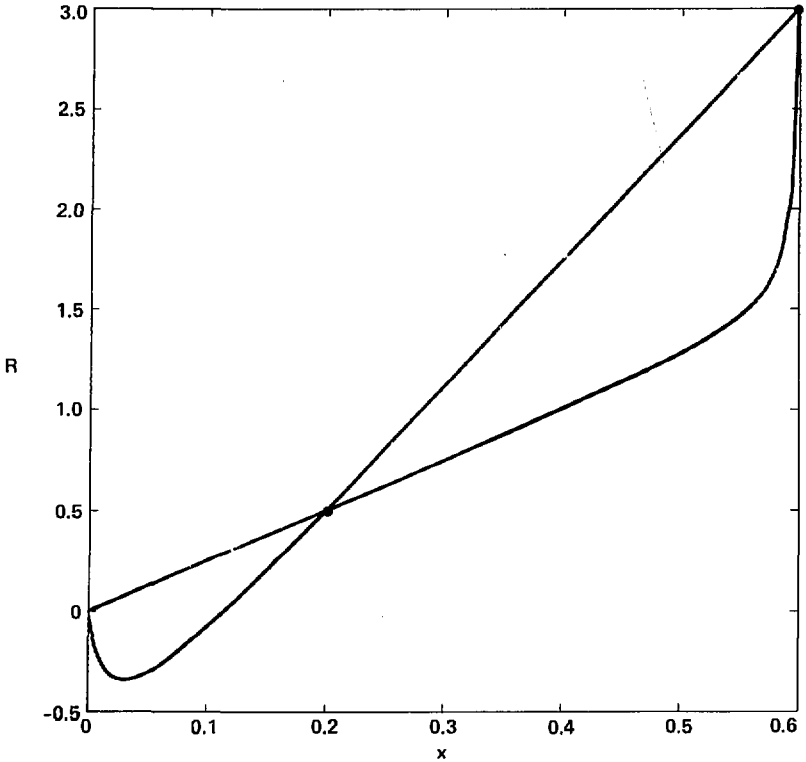

Fig. 2.7 Envelope of family curves with three point interpolation for R(0.2) = 0.5 and R(0.6) = 3.0. In some cases, negative values of R are predicated as x approaches zero.

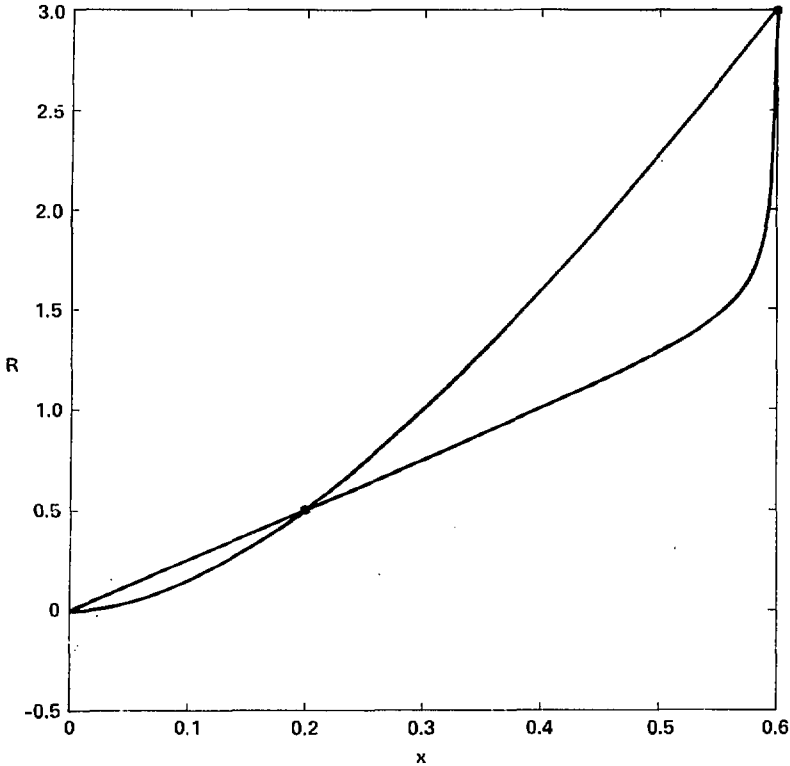

Fig. 2.8 Revised envelope of family of curves. Excluding the curves which give negative values of R changes the envelope shown in Fig. 2.7 to the envelope shown here. Compare to the lower curve in Fig. 2.1 obtained with two point interpolation.

2.3.3 Multivariable Estimates Using Three Point Variational Interpolation.

As with two point interpolation, by successive application of three point variational interpolation, neutronic characteristics can be estimated as a function of more than one variable.

Consider the problem of estimating a reaction rate as a function of two variables x_1 and x_2. Three point interpolation on both variables requires a grid of 9 reference point neutronics calculations as shown in Fig. 2.9. The reference points are denoted (x_{1a},x_{2a}), (x_{1b},x_{2a}), (x_{1c},x_{2a}), (x_{1a},x_{2b}), (x_{1b},x_{2b}), (x_{1c},x_{2b}), (x_{1a},x_{2c}), (x_{1b},x_{2c}), and (x_{1c},x_{2c}). The corresponding reaction rates at the reference points are denoted R_{aa}, R_{ba}, R_{ca}, R_{ab}, R_{bb}, R_{cb}, R_{ac}, R_{bc}, and R_{cc}, respectively.

The procedure to estimate R at some point (x_{1d},x_{2d}) is illustrated in Fig. 2.10. First, the result R_{da} is found by interpolating on x_1 with $x_2 = x_{2a}$. Next, the result R_{db} is found by interpolating on x_1 with $x_2 = x_{2b}$. Thirdly, R_{dc} is found by interpolating on x_1 with $x_2 = x_{2c}$. These three results are used to interpolate on x_2 with $x_1 = x_{1d}$.

In terms of the three point variational interpolation formula, Eq. 2.64, the successive three point interpolation can be written as

$$R_{SI33}(R_{aa},R_{ba},R_{ca},R_{ab},R_{bb},R_{cb},R_{ac},R_{bc},R_{cc};x_1,x_2) \qquad (2.68)$$

$$= R_{SI3}(R_{SI3}(R_{aa},R_{ba},R_{ca};x_1),R_{SI3}(R_{ab},R_{bb},R_{cb};x_1),$$
$$R_{SI3}(R_{ac},R_{bc},R_{cc};x_1);x_2).$$

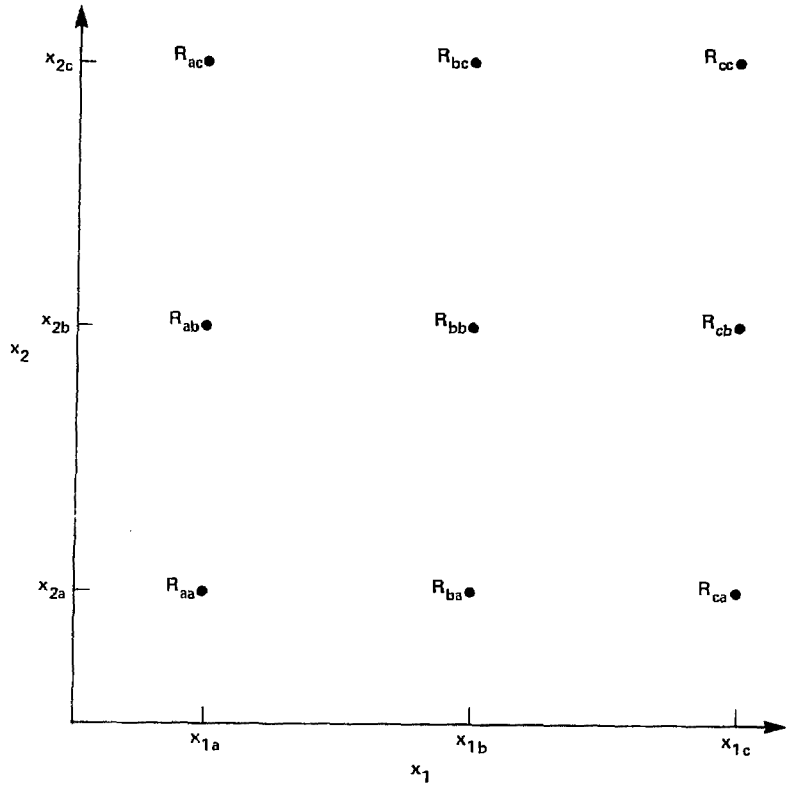

Fig. 2.9 Location of nine reference points for three point interpolation on two variables. Neutron transport calculations are carried out at these nine points. The resulting reaction rates are denoted by R with two subscripts corresponding to the x_1 and x_2 coordinates, respectively.

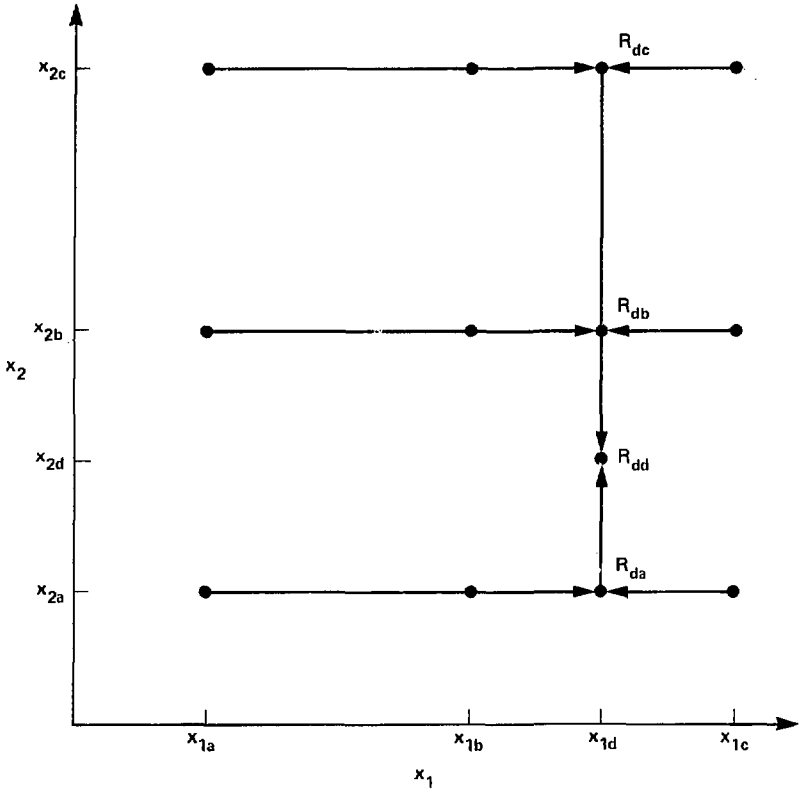

Fig. 2.10 Successive three point variational interpolation. To find the reaction rate at the point (x_{1d}, x_{2d}) requires four interpolations; one to find R_{da}, a second to find R_{db}, a third to find R_{dc}, and a fourth to find R_{dd}.

To extent the three point interpolation to a third variable, x_2, would require 18 more reference transport calculations, and as such gets quite cumbersome. We can, however, combine successive two point and three point interpolations. For two variables, a three point interpolation could be used for one dimension and a two point interpolation for the second. That is,

$$R_{SI32}(R_{aa},R_{ba},R_{ca},R_{ab},R_{bb},R_{cb};x_1,x_2) \tag{2.69}$$

$$= R_{SI2}(R_{SI3}(R_{aa},R_{ba},R_{ca};x_1),\ R_{SI3}(R_{ab},R_{bb},R_{cb};x_1);x_2).$$

This requires 6 reference point transport calculations as indicated. To extend to a third dimension using another two point interpolation requires 6 more transport calculations.

2.4 PROPAGATION OF ERROR

Consider Eq. 2.46 which is the formula for successive, two point interpolation to determine a reaction rate as a function of two variables, x_1 and x_2.

$$R_{SSI}(R_{aa},R_{ba},R_{ab},R_{bb};x_1,x_2) \tag{2.46}$$

$$= R_{SI}(R_{SI}(R_{aa},R_{ba};x_1),\ R_{SI}(R_{ab},R_{bb};x_1);x_2)$$

Note that the "reference values" for interpolation on x_2 are actually estimates based on the previous interpolations on x_1. Refer to Fig. 2.3. The question arises, "How does using these estimates as the basis for interpolation on x_2 affect the accuracy of the result?" Let us compare the result at $x_1 = x_{1d}$ and $x_2 = x_{2d}$ obtained by two methods. The first is by using Eq. 2.46. The second method assumes that two more transport calculations are carried out to determine the exact results at (x_{1d},x_{2a}) and (x_{1d},x_{2b}), denoted R_{dae} and R_{dbe}, respectively. That is, in method 2 the reference values for interpolation on x_2 are exact. Assume that the reference results obtained by variational interpolation on x_1 are related to these exact values by

$$R_{da} = f_a R_{dae}, \tag{2.70}$$

and

$$R_{db} = f_b R_{dbe}.$$

The difference in the result at (x_{1d}, x_{2d}) is given by

$$\Delta = R_{SI}(f_a R_{dae}, f_b R_{dbe}; x_2) - R_{SI}(R_{dae}, R_{dbe}; x_2). \tag{2.71}$$

The magnitude of this additional error (i.e., in addition to the error from using variational interpolation to begin with) depends on the relative magnitude and sign of (f_a-1) and (f_b-1). Referring to Eq. 2.45, note that R_a and R_b terms appear in both the numerator and denominator. If $f_a \sim f_b$, then

$$\Delta \sim (f_a-1)R_{SI}(R_{dae}, R_{dbe}; x_2). \tag{2.72}$$

The fractional difference is (f_a-1). If (f_a-1) and (f_b-1) are opposite in sign; that is, an over estimate of R_{da} and underestimate of R_{db} or vise versa, then the fractional difference will be less than or equal to $(f-1)$. Near $x_2 = x_{2a}$ it will be $\sim (f_a-1)$, and near $x_2 = x_{2b}$ it will be $\sim (f_b-1)$.

Figure 2.11 shows the relative difference as a function of x_2 for three illustrative cases:

$f_a = f_b = 1.05$,
$f_a = 1.05$ and $f_b = 1.00$,
$f_a = 1.05$ and $f_b = 0.95$.

The example is based on the exact reference points (0.2,2.0) and (0.6,3.0). Note how the magnitude of the addition error is less than 5% in all cases.

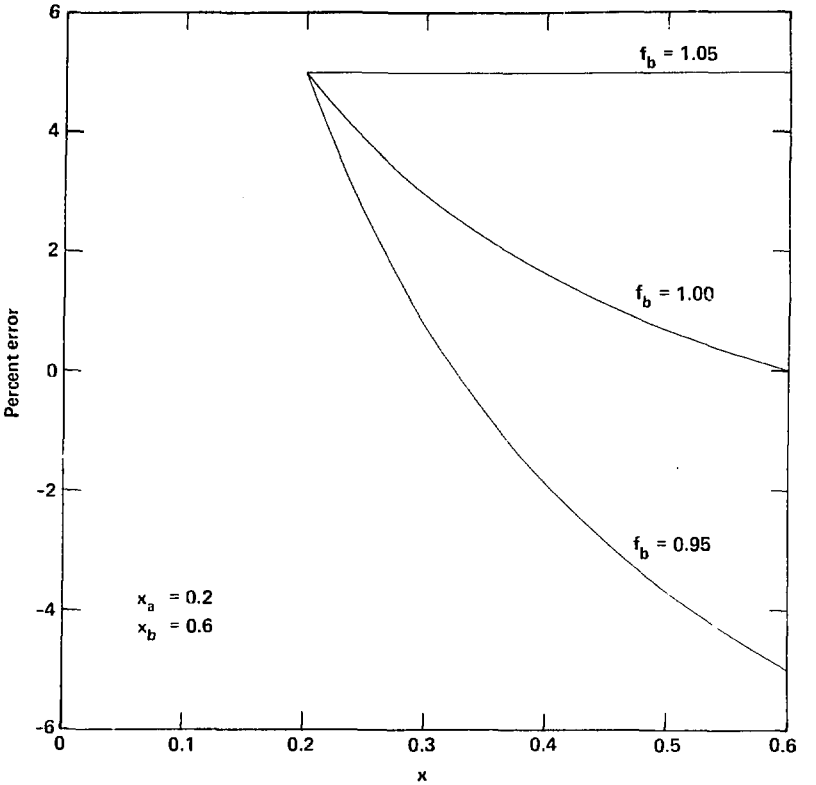

Fig. 2.11 Illustration of additional error due to successive two point interpolation. Refer to Fig. 2.3. The ratios of the interpolated results R_{da} and R_{db} to the exact results at (x_{1d}, x_{2a}) and (x_{1d}, x_{2b}) are denoted f_a and f_b, respectively. Here, f_a = 1.05 and f_b ranges from 0.95 to 1.05. The magnitude of the additional error is less than 5% in the range of interpolation, $0.2 \leq x \leq 0.6$.

For the three point interpolation the additional fractional error can, in some cases, exceed the magnitude of (f_a-1), (f_b-1) or (f_c-1). Here f_a, f_b and f_c are the ratios of the results obtained by three point interpolation on x_1 at $x_2 = x_{2a}$, x_{2b} and x_{2c}, respectively, to the exact results if additional transport calculations had been carried out at (x_{1d},x_{2a}), (x_{1d},x_{2b}) and (x_{1d},x_{2c}), respectively. See Fig. 2.10.

The additional fractional error is shown in Figs. 2.12-2.14. In each case $f_a = 1.05$ and f_c takes on three values 1.05, 1.00, and 0.95. Figure 2.12 is for $f_b = 1.05$, Fig. 2.13 for $f_b = 1.00$ and Fig. 2.14 for $f_b = 0.95$. The exact reference results are (0.2,2.0), (0.4,2.67) and (0.6,3.0). Note that in Fig. 2.12, the error exceeds 5% in the range $0.2 < x_2 < 0.4$ for $f_c = 1.00$ and 0.95. In Fig. 2.13, the magnitude of the error is less than 5% in all cases. In Fig. 2.14, the magnitude of the error exceeds 5% for $f_c = 1.05$ when $0.28 < x < 0.4$ and exceeds 5% for $f_b = 0.05$ when $0.4 < x < 0.6$.

In the previous examples, the error due to the first interpolation was assumed to be less than or equal to 5%. Cheng has evaluated the error due to the Schwinger functional (Eq. 2.16) as well as the two point interpolation form of this functional (Eq. 2.33) by comparing the results to those obtained with transport calculations at various points.[12,36] For the examples he chose, the errors were on the order of 2-5% over a relatively large variation in the design variable.

An expression for the error can be developed in terms of a series solution for the neutron flux. The relationship of the variational principles to perturbation theory has been shown.[36,37] Consider the neutron transport equation

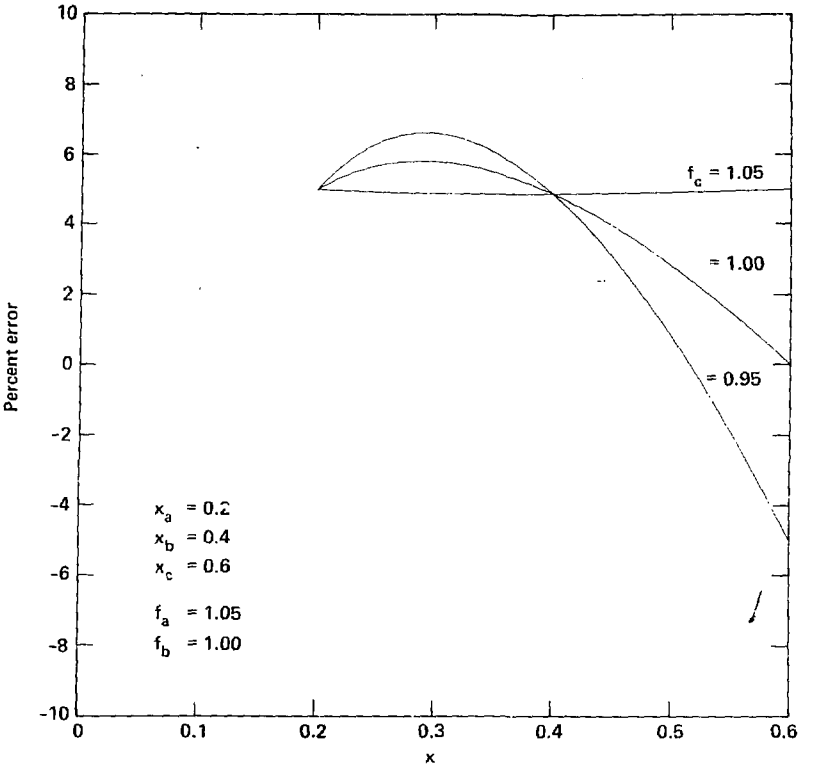

Fig. 2.12 Additional error due to successive three point interpolation for f_b = 1.05. Refer to Fig. 2.10. The ratios of the interpolated results R_{da}, R_{db} and R_{dc} to the exact results at these points are denoted f_a, f_b and f_c, respectively. f_a = 1.05 and f_c ranges from 0.95 to 1.05. The magnitude of the error exceeds 5% in some cases.

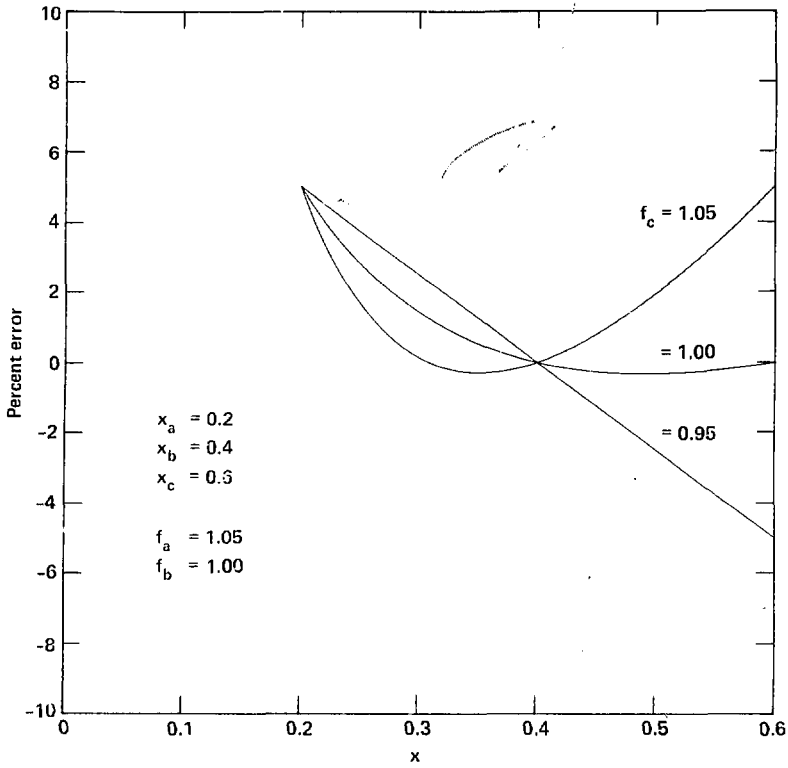

Fig. 2.13 Additional error due to successive three point interpolation for f_b = 1.00.

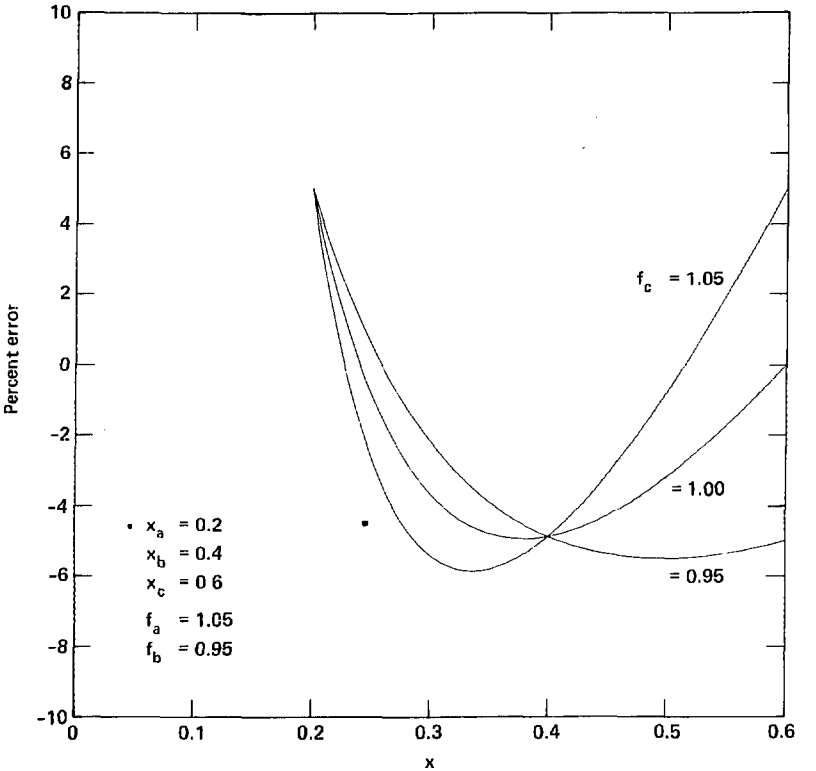

Fig. 2.14 Additional error due to successive three point interpolation for f_b = 0.95.

$$L\phi = S, \tag{2.73}$$

and the associated adjoint equation

$$L^{*}\phi^{*} = S^{*} = \Sigma. \tag{2.74}$$

If the reference system, L_o, is perturbed, the altered system, L, can be related to it by

$$L = L_o + \alpha\delta L, \tag{2.75}$$

where α is a perturbation parameter. The series solution for ϕ is

$$\phi = \sum_{i=0}^{\infty} \alpha^i \phi_i. \tag{2.76}$$

The reaction rate, $<\Sigma,\phi>$, can thus be determined exactly by an infinite series of the solutions, ϕ_i, to the higher order equations

$$L_o\phi_i = -\delta L\phi_{i-1}. \tag{2.77}$$

That is,

$$R = \sum_{i=0}^{\infty} \alpha^i <\Sigma,\phi_i>. \tag{2.78}$$

The variational functionals are given in terms of both forward and adjoint solutions. The adjoint flux can similarly be written as

$$\phi^* = \sum_{i=0}^{\infty} \alpha^i \phi_i^*, \tag{2.79}$$

where ϕ_i^* is the solution to

$$L_0^* \phi_i^* = -\delta L^* \phi_{i-1}^*. \tag{2.80}$$

If the exact solutions, ϕ and ϕ^*, given by Eqs. 2.76 and 2.79 are used in the variational expressions the resultant reaction rate is exact. Truncating the series with the first term gives the Roussopoulos and Schwinger functions described in section 2.1. That is, these estimates are based on the solutions ϕ_0 and ϕ_0^* at the reference point.

The error of the fractional variational functionals, ΔF_{mn}, is given by[36]

$$\Delta F_{mn} = \sum_{j=0}^{n} \sum_{i=0}^{m} \sum_{k=m+1}^{\infty} N \div \sum_{j=0}^{n} D, \tag{2.81}$$

where

$$N = \alpha^{i+j+k+1} \left[\langle \Sigma, \phi_i \rangle \langle \phi_j^*, \delta L \phi_k \rangle - \langle \Sigma, \phi_k \rangle \langle \phi_j^*, \delta L \phi_i \rangle \right],$$

and

$$D = \alpha^j \left[\langle \phi_j^*, S \rangle + \sum_{i=0}^{m} \alpha^{i+1} \langle \phi_j^*, \delta L \phi_i \rangle \right].$$

Here m is the number of terms retained in the solution for ϕ (Eq. 2.76), and n is the number of terms retained in the solution for ϕ^* (Eq. 2.79).

For the Schwinger functional, m=n=0, and Eq. 2.81 reduces to

$$\Delta F_{oo} = \sum_{k=1}^{\infty} \alpha^{k+1} [\langle \Sigma, \phi_o \rangle \langle \phi_o^*, \delta L \phi_k \rangle - \langle \Sigma, \phi_k \rangle \langle \phi_o^*, \delta L \phi_o \rangle] \div [\langle \phi_o^*, S \rangle + \alpha \langle \phi_o^*, \delta L \phi_o \rangle]. \quad (2.82)$$

Hence the error can be evaluated if the solutions, ϕ_k, are calculated.

3. NONLINEAR SIMPLEX METHOD FOR OPTIMIZATION

3.1 BACKGROUND

As previously mentioned, the nonlinear simplex method of Nelder and Mead[14] was chosen for the blanket optimization problem. It is a direct search method which relies on evaluating a function at a sequence of points and comparing values in order to reach the optimal point. The method is based on a geometrical design known as a simplex. An n-dimensional simplex is defined by n + 1 points which are the points at which the function is compared. This should not be confused with the simplex algorithms of linear programming.

Nelder and Mead's method is an improvement on the algorithm proposed by Spendley, et al.[42] Spendley's method uses a regular simplex. A regular simplex is one in which the vertices are equally spaced. An equilateral triangle is an example of a regular simplex. Nelder and Mead's method allows the simplex to become nonregular. It is one of the most efficient direct search methods available and works well if the number of variables is not more than five or six.[13]

While other modifications to Nelder and Mead's method have been proposed,[43,44] they have not been incorporated in the algorithm used in this study. The optimization subroutine used in the blanket optimization problem was previously coded and used by J. Trenholme to optimize the design of experimental lasers at Lawrence Livermore National Laboratory.[45]

3.2 DESCRIPTION OF THE ALGORITHM

The objective is to minimize a function F, where F is a function of n variables $x_1, x_2, \ldots, x_n$. The simplex consists of n + 1 points, P_j.

The following notation will be used. Let

P_h = point with the highest function value,

P_s = point with the second highest function value,

P_ℓ = point with the lowest function value, and

$\bar{P}$ = centroid of all points except P_h.

That is,

$$\bar{P} = \frac{1}{n} \sum_{\substack{j=1 \\ j \neq h}}^{n+1} P_j . \qquad (3.1)$$

Also let

$F_h = F(P_h)$,

$F_s = F(P_s)$,

$F_\ell = F(P_\ell)$.

The method of Nelder and Mead is a follows:[13,14]

1. Choose the points of the initial simplex. In the optimization subroutine used in this work, a single starting

point is specified in the input file. the routine then chooses the initial points of the simplex so that they surround the starting point. It is advantageous, although not required, to choose the starting point from within the feasible region. In general, a feasible starting point can easily be detemined by examining the results of the reference point transport calculations. It is also advisable to run the problem starting at several different points which will help determine if the optimum is unique.

2. Evaluate F at each point and determine the highest point, P_h.

3. Calculate the centroid, $\bar{P}$, of the remaining points.

4. Reflection. The highest point, P_h, is reflected through the centroid of the remaining points, $\bar{P}$. The reflected point is denoted P_r. The value of F at P_r is calculated and denoted F_r. The reflection factor, $\alpha > 0$, is the ratio of the distance between $\bar{P}$ and P_r to the distance between P_h and $\bar{P}$. That is,

$$P_r - \bar{P} = \alpha(\bar{P} - P_h), \tag{3.2}$$

or

$$P_r = (1+\alpha)\bar{P} - \alpha P_h.$$

If $\alpha = 1$, the reflected point is as for on the other side of the centroid as the high point is from the near side. The

reflection move is illustrated in Fig. 3.1a for a two dimensional case.

5. If $F_\ell \leq F_r \leq F_s$, replace P_h by P_r and return to Step 2. That is, if the value of the function at the reflected point falls between the low value and second to highest value, the old high point is replaced by the reflected point.

6. Extension. If $F_r < F_\ell$, extend the simplex using an extension factor $\gamma > 1$. That is, find the extended point, P_e, such that

$$P_e - \bar{P} = \gamma(P_r - \bar{P}) \tag{3.3}$$

or

$$P_e = (1 - \gamma)\bar{P} + \gamma P_r.$$

The value of the function at this point is F_e. In this case a new low value has been found ($F_r < F_\ell$) so the reflected point is moved farther in the same direction to see if f continues to decrease. There are two possible results:

a) If $F_e < F_\ell$, replace P_h by P_e and return to Step 2.

b) If $F_e \geq F_\ell$, replace P_h by P_r and return to Step 2. In this case the extension has failed. It can be viewed as moving into a valley ($F_r < F_\ell$) but the extension produces a result F_e that is up the slope on the opposite side. The extension move is illustrated in Fig. 3.1b.

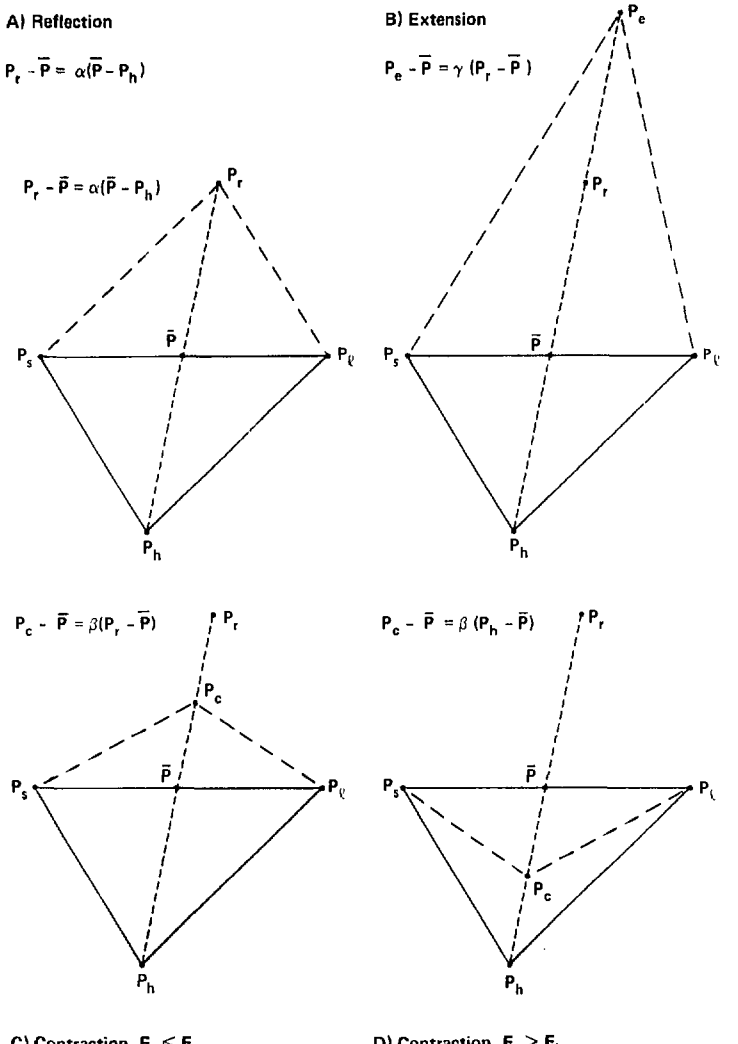

Fig. 3.1 Four basic moves in Nelder and Mead's nonlinear simplex method of optimization.

7. Contraction. If $F_r > F_s$, contract the simplex using a contraction factor β, where $0 < \beta < 1$. There are two cases:

a) If $F_r \leq F_h$, find the contracted point P_c defined by

$$P_c - \bar{P} = \beta(P_r - \bar{P}), \tag{3.3}$$

or

$$P_c = (1 - \beta)\bar{P} + \beta P_r.$$

This is illustrated in Fig. 3.1c.

b) If $F_r > F_h$, find the contracted point P_c defined by

$$P_c - \bar{P} = \beta(P_h - \bar{P}), \tag{3.4}$$

or

$$P_c = (1 - \beta)\bar{P} + \beta P_h.$$

This is illustrated in Fig. 3.1d. Note that Step 6a is the equivalent of replacing P_h by P_r and then finding P_c defined by Eq. 3.4. For either 7a or 7b there are again two cases to consider:

c) If $F_c < F_h$ and $F_c < F_r$, replace P_h by P_c and return to Step 2.

d) If $F_c \geq F_h$ or $F_c \geq F_r$, reduce the size of the simplex by halving the distance from P_ℓ and return to Step 2. That is, replace all P_j by $(P_j + P_\ell)/2$. This last move is referred to

as a huddle.

We see that in Nelder and Mead's method, each iteration begins with a reflection move. Subsequent steps depend on the value of the function at the reflected point with respect to the highest, second-to-highest and lowest values of function evaluated at the vertices of the simplex (i.e., how F_r compares to F_h, F_s, and F_ℓ). The authors recommend the values $\alpha = 1$, $\beta = 0.5$, and $\Upsilon = 2$ as the best strategy.[14] A flow diagram is given in Fig. 3.2.

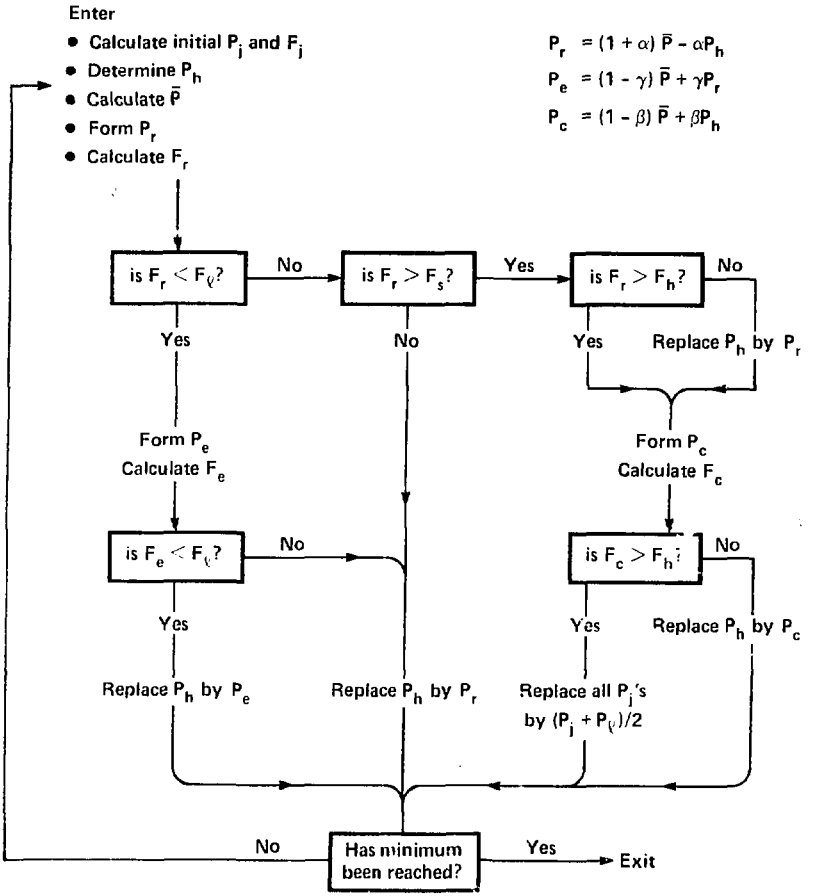

Fig. 3.2 Logic flow diagram for Nelder and Mead's nonlinear simplex method (after Ref. 14).

3.3 CONVERGENCE CRITERION

After each iteration, two convergence criteria are checked to see if the search should be halted, i.e., if the minimum has been located. The first criterion compares the highest function value in the simplex, F_h, to the lowest, F_ℓ. If these two values differ by less than some small number, ε, the search is halted. That is, if

$$F_h - F_\ell < \varepsilon. \tag{3.5}$$

The second criterion is based on the distance between the location of highest and lowest value of the current simplex. If the distance is less than δ, the subroutine terminates. Let $[P_h P_\ell]$ represent the distance between P_h and P_ℓ. If

$$[P_h P_\ell] < \delta, \tag{3.6}$$

the search is halted. Both ε and δ are input parameters for the optimization subroutine. Clearly the optimal point is P_ℓ, and the value of the function is F_ℓ at the time when either criteria is met

3.4 HANDLING CONSTRAINTS

Constraints limit the acceptable range from which points can be chosen in searching for the minimum value of F. With Nelder and Mead's method constraints are handled in the definition of the function to be minimized. That is, if a constraint is violated, F is set equal to an arbitrarily large number. As such, if a point in the simplex results in a violated constraint, contraction moves will be made until all points of the simplex are inside the feasible region. See Fig. 3.3. A problem can arise if the search is started in the unfeasible region. If all points of the initial simplex lie in the unfeasible region, they all have the same value, and the first convergence criterion, Eq. 3.5, is satisfied. As a result the search terminates. This difficulty can easily be corrected.

Fox and Liebman proposed a modified method of handling constraints.[43] It is illustrated in Fig. 3.4. Here the value of the function in the infeasible region slopes down toward the feasible region like a funnel. In this way, if the search is begun in the infeasible region, it will proceed until it falls into the "well" of the feasible region.

In the next chapter, the method of estimating neutronic performance is combined with the optimization algorithm described in this chapter to optimize the blanket of an inertial confinement fusion reactor.

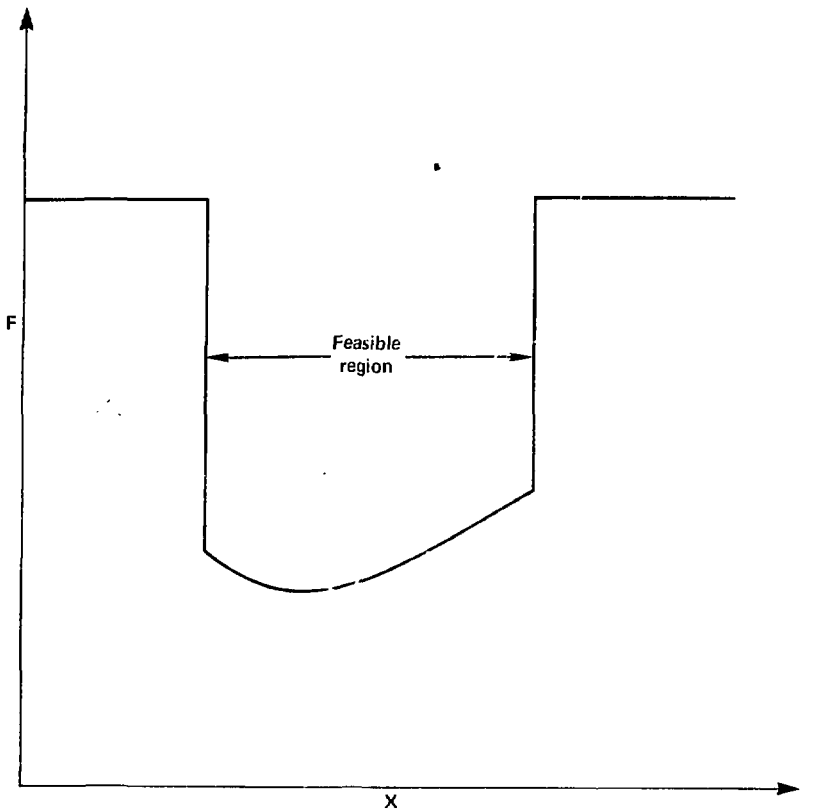

Fig. 3.3 A simple method of handling constraints. The figure of merit, F, is defined to be an arbitrarily large number outside the feasible region.

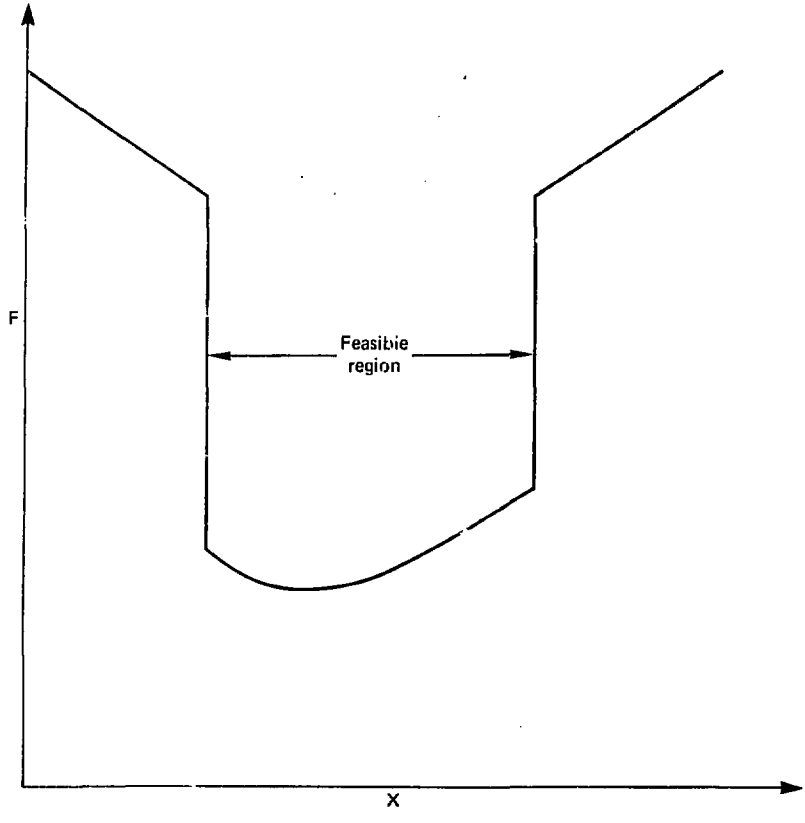

Fig. 3.4 Fox and Liebman's method of handling constraints. The search is directed toward the feasible region.

4. OPTIMIZATION OF A MODIFIED HYLIFE CHAMBER

4.1 DESCRIPTION OF THE PROBLEM

4.1.1 The HYLIFE Reactor Concept.

The High Yield Lithium Injection Fusion Energy (HYLIFE) chamber for inertial confinement fusion (ICF) has been described in detail in the literature.[1,46-51] The HYLIFE Concept is illustrated in Fig. 4.1, and a cross sectional view is shown in Fig. 4.2

In the HYLIFE chamber, an array of lithium jets is injected into the chamber between fusion pulses to provide the equivalent of a 1-m-thick blanket between the fusion target and the first structural wall. This energy conversion blanket shields the chamber structural materials from direct exposure to the x-rays, debris, and high-energy neutrons emitted by the fusion pellet. The 14 MeV neutron flux is reduced by more than a factor of 200, and neutron damage levels are low enough to allow the 5-m-radius chamber wall to operate for more the 30 years without replacement.[52,53] With a 1.0 m thick blanket of natural lithium (7.42% ^{6}Li and 92.58% ^{7}Li), HYLIFE achieves a tritium breeding ratio of 1.75.[54]

The subject of this first blanket optimization problem is a modification of the HYLIFE chamber. The modified design is an attempt to increase the energy deposited in the chamber per fusion reaction. The ratio of total energy deposited to the fusion energy released per DT reaction is defined as the fusion energy multiplication factor, M_f. It is given by

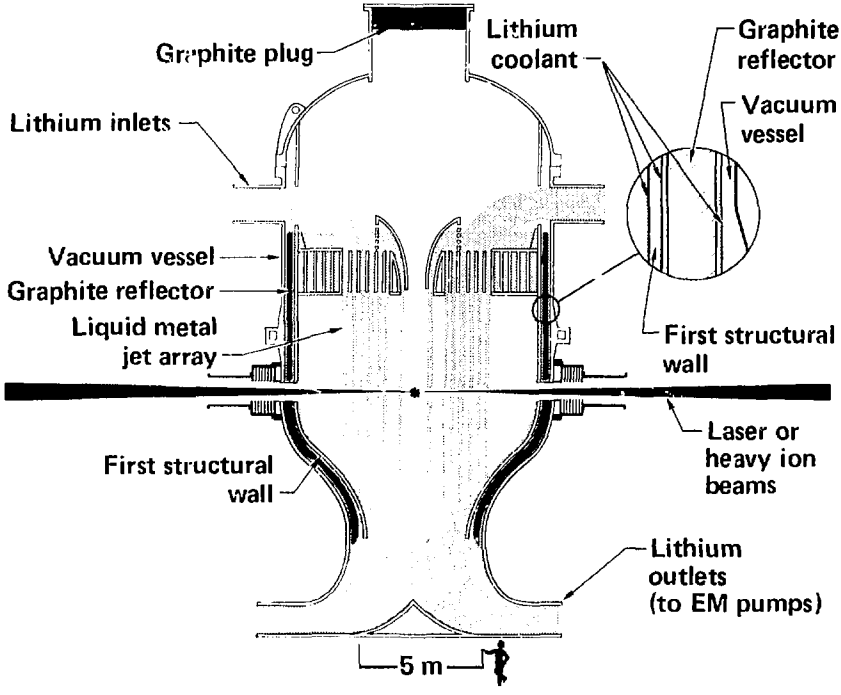

Fig. 4.1 The HYLIFE concept.

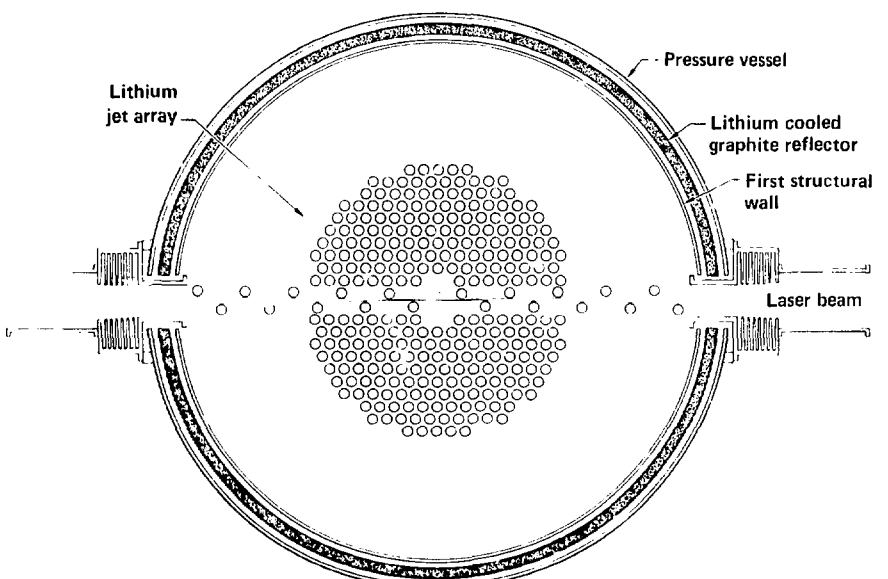

Fig. 4.2 Cross sectional view of HYLIFE.

$$M_f = (E_n + 3.5)/17.6, \quad (4.1)$$

where

E_n = the total energy (MeV) deposited as a result of neutron reactions within the chamber. It includes the neutron energy deposited in the compressed fuel region of an ICF target.

The factor 3.5 is the fusion alpha particle energy in MeV and 17.6 MeV is the total fusion energy released per DT reaction. In general, M_f will be slightly greater than one due to exoergic neutron reactions with blanket materials, e.g., the $^6Li(n,T)\alpha$ reaction which releases 4.8 MeV. For HYLIFE, M_f is 1.16.

The approach in the modified HYLIFE design is to reduce the tritium breeding ratio and capture the excess neutrons in ^{55}Mn. Each capture in ^{55}Mn adds 9.8 MeV to the energy balance. The $^{55}Mn(n,\gamma)$ reaction releases 7.3 MeV while the decay of the product, ^{56}Mn, releases an additional 2.5 MeV of recoverable energy.[55] The half-life for the β^- decay is 2.6 hours.

Increasing M_f by capturing neutrons in structural material has been previously proposed.[56] The authors of Refs. 57 and 58 suggested a 14% Mn steel called Fe-1422 for the purposes of increasing M_f. In this work, a 20% Mn steel, known as Nippon Steel Alloy NM-1, is used.[59] The composition of NM-1 by weight percent is 77.5% Fe, 20.0% Mn, 2.0% Cr and 0.5% C.[59]

The potential advantage of increasing the fusion energy multiplication factor is a lower cost of electricity from a fusion-electric power plant. This follows since more power is

available for a given investment in the laser driver and target factory in the case of ICF (or for a given investment in the magnets for magnetic fusion reactors). That is, fixing the size of the laser and the characteristics of the target, fixes the fusion energy released per pulse. If this energy can be increased as a result of neutron reactions in the blanket, more thermal energy will be available for conversion to electricity. In the blanket optimization problem, the characteristics of the driver and target are fixed, as is the chamber pulse repetition rate. The variables relate only to the design of the blanket itself as discussed below.

There are two simple ways to reduce the tritium breeding ratio in HYLIFE; one is to reduce the fraction of ^{6}Li in lithium and the other is to reduce the effective thickness of the lithium blanket, i.e., the lithium jet array.[60] In addition, the Li cooled graphite reflector (see Fig. 4.1 and 4.2) is replaced by a sodium cooled Mn-steel blanket in the modified design. Hence all the tritium breeding must occur in the lithium blanket. The two design variable for this problem are

x_1 = ^{6}Li fraction in Li,

and

x_2 = effective Li blanket thickness, m.

Note that the actual thickness of the Li blanket is held constant while the packing fraction of liquid lithium jets within that region is varied. This is, in essence, a variation of the material density and thus qualifies as a linear perturbation as seen from Eq. 2.34.

4.1.2 Constraints on the Design.

Reducing the blanket thickness is advantageous in that it reduces the Li flow rate resulting in savings in pumping power and capital costs for liquid metal pumps and piping. There is a lower limit, however, set by a constraint on the maximum allowable radiation damage rate in the first structural wall. For HYLIFE the rate was limited to the point where the wall was expected to maintain its structural integrity for the 30 year life of the power plant.[1] The life limiting radiation damage mechanism for HYLIFE was found to be the displacement of atoms from their lattice positions.[1] Displaced atoms leave vacancies which can conglomerate to form voids within the steel, and this leads to a phenomena known as void swelling.[61] After some total amount of damage, expressed in terms of displacements per atom or dpa, the structural material is deformed, and/or its properties are degraded to the point where it loses its integrity.

Currently there is insufficient data to set absolute damage limits for structures in fusion reactors. It is known, however, that ferritic steels are less susceptible to the effects of displacement damage than austenitic steels,[62] and a damage limit of ~200 dpa was recently suggested as a reasonable estimate for high Cr ferritic steels.[63] A low-alloy, ferritic steel, 2.25 Cr-1 Mo, was specified for HYLIFE due to its low cost, resistance to liquid-metal corrosion and resistance to the effects of radiation damage.[51]

For the purposes of this study, the total displacement damage in the first structural wall of the modified HYLIFE chamber is limited to 200 dpa over an operating period of 30 years at 70% plant capacity factor. This gives a constraint on the displacement damage rate of

9.5 dpa per full-power-year. The dpa rate is expected to depend primarily on the blanket thickness, x_2, but may also depend somewhat on the ^6Li fraction.

Another constraint in the optimization problem is the requirement for a tritium breeding ratio high enough to assure a self-sufficient fuel cycle. A tritium breeding ratio $\geq$ 1.05 has been chosen to satisfy this criteria. Clearly the tritium breeding ratio will be a function of both design variables.

4.1.3 Figure of Merit for HYLIFE.

The figure of merit for this optimization problem is the capital cost of the power plant divided by the net electric power production. That is,

$$F = C_T/P_n, \tag{4.2}$$

where

C_T = total plant capital cost including the cost of the reactor, laser and target factory, \$, and

P_n = net electric power produced and available for sale, kW_e.

The cost of electricity (i.e., ¢/kW_eh) from a fusion electric power plant is expected to be dominated by the carrying charges on the capital investment.[47] The capital cost portion of the cost of electricity is given by

$$C_e = 1C_T/8760fP_n \tag{4.3}$$

where

i = fixed charged rate, yr^{-1} (typically 15% per year),

f = plant capacity factor (typically 70%), and

8760 = number of hours per year.

Since to first order, i and f are independent of the blanket design, the cost of electricity is proportional to C_T/P_n. Hence minimizing the plant capital cost per unit of net electric power is equivalent to minimizing the cost of electricity under these assumptions.

The total capital cost is broken into four components,

$$C_T = C_R + C_P + C_L + C_{TF}, \tag{4.4}$$

where

C_R = cost of the reactor including the balance of plant required for heat transfer and conversion to electricity,

C_P = cost of lithium recirculating pumps and piping required to maintain the flowing lithium blanket,

C_L = cost of the laser driver, and

C_T = cost of the target factory.

The cost of the reactor scales as the plant thermal power, P_t, raised to the 0.8 power,[64]

$$C_R \propto P_t^{0.8}. \tag{4.5}$$

The thermal power is simply the fusion power, P_f, times the fusion energy multiplication factor, M_f. Hence

$$C_R \propto (M_f P_f)^{0.8}. \tag{4.6}$$

As previously stated, P_f is fixed but M_f will be a function of both the ^6Li fraction, x_1, and the Li blanket thickness, x_2.

The cost of the pumps will be proportional to the total lithium flow rate through the chamber. The flow rate is taken to be proportional to the effective blanket thickness x_2, hence

$$C_p \propto x_2. \tag{4.7}$$

The cost of the laser and target factory are fixed and independent of the two design variables.

The actual costs are referenced to those listed in Table 4.1 for HYLIFE.[47] Using these values, the direct capital cost of the modified HYLIFE chamber in \$B is,

$$C_T \quad 0.96(M_f/1.16)^{0.8} + 0.16x_2 + 0.43. \tag{4.8}$$

The net electric power is given by

$$P_n = P_g - P_\ell - P_a - P_p, \tag{4.9}$$

where

P_g = gross electric power, MW_e,

P_ℓ = laser power requirement, MW_e,

Table 4.1

Reference HYLIFE plant characteristics for comparison

Tritium breeding ratio	$T = 1.75$
Neutron energy deposition	$E_{n} = 16.9$ MeV
Fusion power	$P_f = 2700$ MW
Fusion energy multiplication factor	$M_f = 1.16$
Thermal power	$P_t = 3130$ MW_f
Thermal conversion efficiency	$\eta_t = 39\%$
Gross electrical power	$P_g = 1220$ MW_e
Laser power consumption	$P_\ell = 135$ MW_e
Auxiliary power requirements	$P_a = 75$ MW_e
Lithium pumping power[a]	$P_p = 30$ MW_e
Net electrical power	$P_n = 980$ MW_e
Direct capital costs	
Reactor[b]	$C_R = \$960$ M
Lithium pumps	$C_P = \$160$ M
Laser[c]	$C_L = \$330$ M
Target factory	$C_{TF} = \$100$ M
TOTAL	$C_T = \$1.55$ B

(a) based on a lithium blanket thickness of 1.0 m and ~50% efficient EM pumps.

(b) reactor includes the chamber and balance of plant required for heat transfer and conversion to electricity; it excludes the Li recirculating pumps.

(c) half the estimated cost of 4.5 MJ laser; it is assumed that the laser drives two full sized reactors by switching beams.

P_a = plant auxiliary power requirements, MW_e, and

P_p = lithium pumping power, MW_e.

The gross electric power is equal to the thermal conversion efficiency times the thermal power and, therefore, is proportional to the fusion energy multiplication factor M_f. The laser and auxiliary power requirements are independent of the blanket design. The lithium pumping power is taken to be proportional to the lithium flow rate and hence to the blanket thickness, x_2. Again, the values are based on the HYLIFE parameters listed in table 4.1. Hence

$$P_n = 1220(M_f/1.16) - 135 - 75 - 30x_2, \qquad (4.10)$$

or

$$P_n = 1220(M_f/1.16) - 30x_2 - 210,$$

where x_2 is in meters.

Combining Eqs. 4.8 and 4.10 and normalizing to the HYLIFE cost of \$1.55 B and net power of 980 MW_e gives the figure of merit as

$$F = [0.62(M_f/1.16)^{0.8} + 0.10x_2 + 0.28]/D, \qquad (4.11)$$

where

$$D = 1.24(M_f/1.16) - 0.03x_2 - 0.21.$$

4.1.4 Summary.

In summary, the optimization problem is to minimize F given by Eq. 4.11 subject to the constraint on the displacement damage rate,

$$D \leq 9.5 \text{ dpa/yr}, \qquad (4.12)$$

and the constraint on the tritium breeding ratio,

$$T \geq 1.05. \tag{4.13}$$

The methods of Chapter 2 are used to write analytical expressions for the fusion energy multiplication factor, the tritium breeding ratio, and the displacement damage rate, as a function of the two design variables, x_1 and x_2. Hence the figure of merit can be calculated at any point (x_1,x_2). The methods of Chapter 3 are then applied to optimize the figure of merit subject to the constraints.

The first calculation of the optimal design point for the modified HYLIFE chamber is based on the two point variational interpolation method for estimating the neutronic performance. As such, four reference point neutron transport calculations are required. The neutronics model and results for these initial reference point calculations are discussed in the next section.

4.2 REFERENCE POINT TRANSPORT CALCULATIONS

4.2.1 TART Monte Carlo Transport Code.

All neutronics calculations were carried out with TART, a coupled neutron-photon Monte Carlo transport code.[65] Cross sections are derived from TART's data base, the Evaluated Nuclear Data Library which includes neutron data from 10^{-9} MeV to 20 MeV and photon data from 1 keV to 20 MeV.[9] It is a multigroup code utilizing 175 energy groups.

An input file is created by the user which describes the geometry of the problem, composition of each zone, the characteristics of the neutron source and the type of output desired. Geometry refers to the boundary functions of a problem. Combining a number of boundary functions creates a unique and unambiguous volume called a zone. The boundaries are either planes or quadradic. TART is capable of handling three dimensional problems. The composition of each zone is described by specifying the isotopes, the isotopic fraction and density of the material represented by the zone. For fusion reactor problems a monoenergetic source of 14.1 MeV neutrons is generally specified. Many different kinds of output can be obtained from the same TART problem. Of particular interest for this study are reaction rates, energy dependent neutron flux, and energy deposition as a result of neutron interactions. All output is normalized to one source neutron. A typical problem will track 20,000 neutrons (20 groups of 1000) and take 1-3 minutes of CRAY time. In addition to Ref. 65, a TART users manual is available on the MFECC computer network (see Appendix II).

4.2.2 Neutronics Model of the HYLIFE Chamber.

The neutronics model of the modified HYLIFE chamber is shown in Figs. 4.3 and 4.4. Figure 4.3 represents a horizontal slice through the midplane of the chamber. Note that it has been subdivided into two halves and Fig. 4.4 shows only the right half. This was necessary since the current version of TART does not allow the user to output reaction rates and neutron flux for the same zone. A new version of TART will correct this difficulty.[66]

Zone 1 represents the compressed DT in which the 14.1 MeV fusion neutrons are born. The neutron source is distributed uniformly throughout this hemispherical zone. The target has a density radius product, ρR, of 3 g/cm^2. Zone 2 is essentially void, containing Li vapor at a very low density.

Zones 3 and 4 represent the Li jet array where all the tritium breeding occurs in this modified HYLIFE concept. The effective density and isotopic fraction of ^{6}Li is varied in these zones. The inner radius of these zones in 0.5 m and they are 2.0 m thick. The density of Li in zones 3 and 4 is less than normal density in order to represent the packing fraction of liquid Li jets within the jet array. Using density multipliers of 0.375 and 0.625 give effective thicknesses of 0.75 m and 1.25 m for the Li blanket. These are the two reference values for x_2. That is, $x_{2a} = 0.75$ and $x_{2b} = 1.25$. The reference values for ^{6}Li concentration in the Li are 0.50% and 7.42%, i.e. $x_{1a} = 0.0050$ and $x_{1b} = 0.0742$. The combinations of these values define the four reference point calculations for the two point interpolation on two variables.

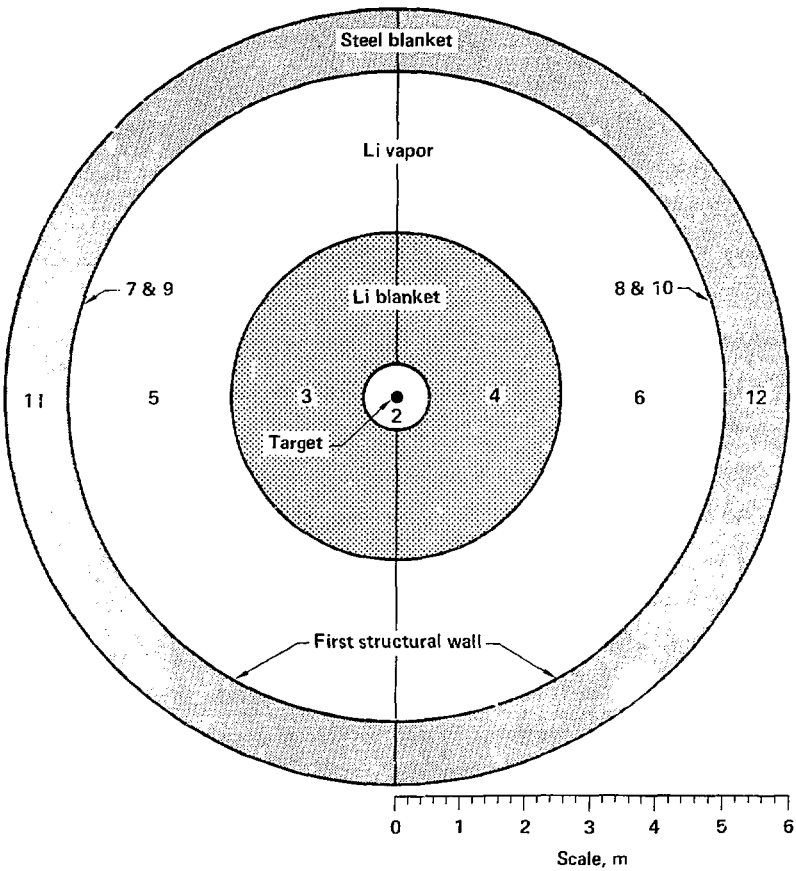

Fig. 4.3 Cross sectional view of the neutronics model for the modified HYLIFE chamber. Zone numbers are indicated.

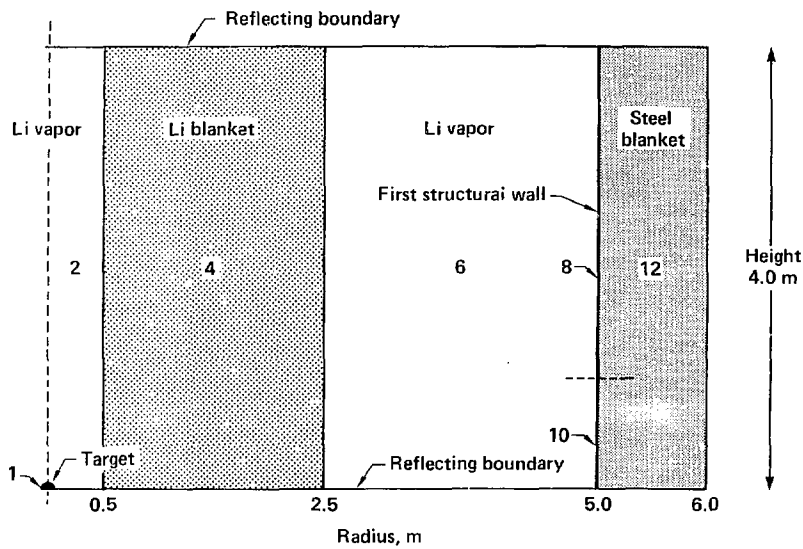

Fig. 4.4 Neutronics model of the modified HYLIFE chamber.

Returning to Figs. 4.3 and 4.4, zones 5 and 6 are again Li vapor regions. Zones 7-10 represent a low-alloy, ferritic steel, first structural wall for the chamber. The inner radius is 5.0 m and the wall is 2 cm thick. The neutron flux in the 1-m-high zone 10 is used to determine the peak neutron damage rate in the first structural wall. It gives a peak damage rate since it is nearer to the neutron source and protected by less Li than the wall as a whole. Zones 11 and 12 represent the energy multiplying steel blanket. These 1-m-thick zones contain 80 vol% Mn steel and 20 vol% Na coolant.

Figure 4.4 is a vertical slice through the neutronics model. The top and bottom boundaries are reflecting planes. That is, if a neutron's path intersects one of these planes, it is "reflected" back into the problem at the point of intersection. The bottom plane represents the symmetry of the HYLIFE chamber.

The top (and the bottom) of the HYLIFE chamber contain thick pools of Li. With a top reflecting plane in the neutronics model, neutrons are reflected back into the Li jet array and the effect is essentially the same as if a Li pool would have been added at the top. This was verified by comparing the results of a TART calculation with a model such as this to the results reported in Ref. 10 which modeled the HYLIFE chamber in detail. Both the tritium breeding ratio and neutron energy deposition were very close. With the reflected model, the tritium breeding ratio and neutron energy deposition were 1.74 and 17.0 MeV, respectively, compared to the Ref. 54 results of 1.75 and 16.9 MeV. Hence it is felt that the simple model illustrated in Figs. 4.3 and 4.4 adequately represents the chamber being considered

in this study.

A detailed description of the geometry and composition of the neutronics model is given in Tables 4.2 and 4.3.

4.2.3 Results of the Four Initial Transport Calculations.

The results of the reference point neutronics calculations are given in Tables 4.4 and 4.5. With a few exceptions all parameters listed are output directly by TART. The exceptions are discussed below.

The energy deposition by isotope in the Li blanket required a modification of the standard method that TART uses to calculate energy deposition. Normally, energy-dependent energy deposition factors are determined for the mixture of isotopes making up the material in a zone. These factor times the expected number of collisions per energy group, summed over all energy groups gives the total energy deposited in the zone.

To get the energy deposition by isotope requires the order of summations to be changed. By determining energy deposition factors for each isotope in the material, multiplying it by the number of collisions with that isotope, and summing over all energy groups gives the energy deposition by isotope in the zone.

The other calculated parameter is the displacement damage rate. Using the neutron fluence in zone 10 calculated by TART, the displacement damage rate (dpa per full power year) is calculated as follows:

$$D = S \sum_{i} \sigma_i \Phi_i, \qquad (4.14)$$

Table 4.2

Geometric characteristics of the modified HYLIFE neutronics model

Zone	Description	Inner Radius (cm)	Outer Radius (cm)	Height (cm)	Material
1	Target	0	0.03	--	1
2	Li Vapor	0	50	400	2
3, 4	Li Blanket	50	250	400	3
5, 6	Li Vapor	250	400	400	2
7, 8	Steel Wall	500	502	300	4
9, 10	Steel Wall	500	502	100	4
11, 12	Steel Blanket	502	600	400	5

Table 4.3

Material compositions of the modified HYLIFE neutronics model

Material	Composition (Vol%)		Density (g/cm^3)	Isotopic Fractions (%)	
1	DT	100	100	D	50
				T	50
2	Li	100	10^{-8}	^6Li	7.42
				^7Li	92.58
3a	Li	100	0.490	^6Li	7.42
				^7Li	92.58
3b	Li	100	0.495	^6Li	0.50
				^7Li	99.50
4*	Fe	100	7.86	Fe	100.00
5**	NM-1	80	6.49	Na	5.97
	Na	20		Cr	2.01
				Mn	19.03
				Fe	72.99

* The first structural wall is 2.25 Cr-1 Mo steel. For the purposes of these calculations, it is represented by 100% natural Fe.

** The steel blanket is 80 Vol% NM-1 steel (77.5 wt% Fe, 20.0 wt% Mn, 2 wt% Cr) and 20 vol% Na as the coolant.

Table 4.4

Reaction rates and neutron damage rates for the four initial reference points

Reference Point	1	2	3	4
^{6}Li Fraction, %	0.50	7.42	0.50	7.42
Li Thickness, m	0.75	0.75	1.25	1.25
Reactions[a]				
^{6}Li(n,T)α	0.440 (1.2)[c]	0.797 (1.2)	0.733 (1.0)	1.004 (1.1)
^{7}Li(n,n'T)α	0.664 (1.2)	0.628 (0.8)	0.718 (1.1)	0.663 (1.2)
^{7}Li(n,γ)	0.004 (1.2)	--	0.007 (1.5)	--
Mn(n,γ)	0.331 (1.9)	0.156 (2.3)	0.185 (1.5)	0.057 (4.1)
Fe(n,γ)	0.343 (1.8)	0.159 (2.1)	0.193 (1.5)	0.057 (3.8)
Displacement Damage Rate[b]	15.5 (3)	13.5 (3)	3.95 (8)	2.92 (8)

a) per DT fusion reaction.

b) dpa per full-power-year based on 2700 MW of fusion power.

c) percent standard deviation.

Table 4.5

Energy deposition for the four initial reference points

Reference Point	1	2	3	4
^{6}Li Fraction, %	0.50	7.42	0.50	7.42
Li Thickness, m	0.75	0.75	1.25	1.25
Energy Deposition[a]				
Target	1.83 (0.4)[c]	1.85 (0.4)	1.83 (0.5)	1.84 (0.4)
^{6}Li	2.09 (1.2)	4.66 (1.0)	3.61 (0.9)	5.72 (1.0)
^{7}Li	8.96 (1.7)	8.21 (3.0)	9.64 (2.3)	8.73 (4.7)
First wall	0.73 (1.7)	0.35 (3.0)	0.40 (2.3)	0.09 (4.7)
Steel blanket	5.29 (1.5)	2.94 (2.1)	2.57 (1.7)	0.89 (3.5)
Mn decay[b]	0.83	0.39	0.46	0.14
Alpha particle	3.52	3.52	3.52	3.52
TOTAL	23.25	21.92	22.03	20.93

a) MeV per DT fusion reaction.

b) energy released from decay of ^{56}Mn equals 2.5 MeV per Mn(n,Y) reaction.

c) percent standard deviation.

where

S = neutron source, n/yr,

σ_i = energy dependent displacement cross section, b,

Φ_i = energy dependent neutron fluence, n/cm^2 per source neutron, and

i = energy group index for the multigroup calculation.

The source of DT neutrons is related to the fusion power, P_f, by

$$S = 11.2 \times 10^{24} P_f, \tag{4.15}$$

where P_f is in MW.

The displacement damage cross section for iron is shown in Fig. 4.5. This cross section was calculated by Doran and Graves[67] and is somewhat higher than a previously published version.[68,69] It is based on an effective displacement energy of 40 eV, which is recommended for iron. For low energy neutrons, the displacement cross section varies as $E^{-0.5}$ from a value of 17b at 0.025 eV.[68]

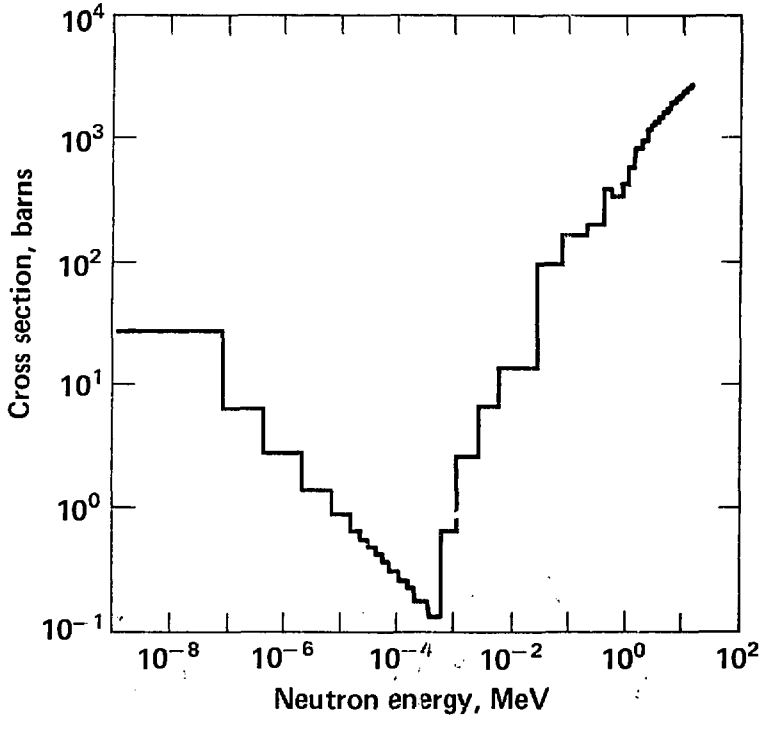

Fig. 4.5 Displacement damage cross section for iron.

4.3 INITIAL OPTIMIZATION RESULTS FOR HYLIFE

Estimated Neutronic Performance.

Based on the results of the four reference point neutronics calculations, the tritium breeding ratio, displacement damage rate and neutron energy deposited in the chamber are estimated using successive two point interpolation (Eq. 2.46).

The results for tritium breeding are shown in Figs. 4.6-4.9. Figure 4.6 shows the number of $^{6}Li(n,T)\alpha$ reactions per DT reaction, denoted T6, as a function of the two design variables, ^{6}Li fraction in the Li blanket and the Li blanket thickness. (Note that those portions of the surface outside the range $0.5\% \leq x_1 \leq 7.42\%$ are extrapolations not interpolations.) As seen in Fig. 4.6, T6 increases with increasing ^{6}Li fraction and also with increasing blanket thickness. The rise in T6 is very sharp at low ^{6}Li concentrations.

The number of $^{7}Li(n,n'T)\alpha$ reactions per DT fusion reaction, denoted T7, as a function of the two design variables is shown in Fig. 4.7. Note the change in the vertical scale from the previous figure. As indicated, T7 decreases with increasing ^{6}Li fraction. This is as expected since the ^{7}Li concentration decreases as the ^{6}Li concentration increases. Also, T7 increases with increasing blanket thickness.

The sum of T6 and T7 gives the tritium breeding ratio, denoted T, as shown in Fig. 4.8. Since the variation in T7 over this range of variables is relatively small, the tritium breeding ratio surface essentially mimics the features of the T6 surface. Some difference,

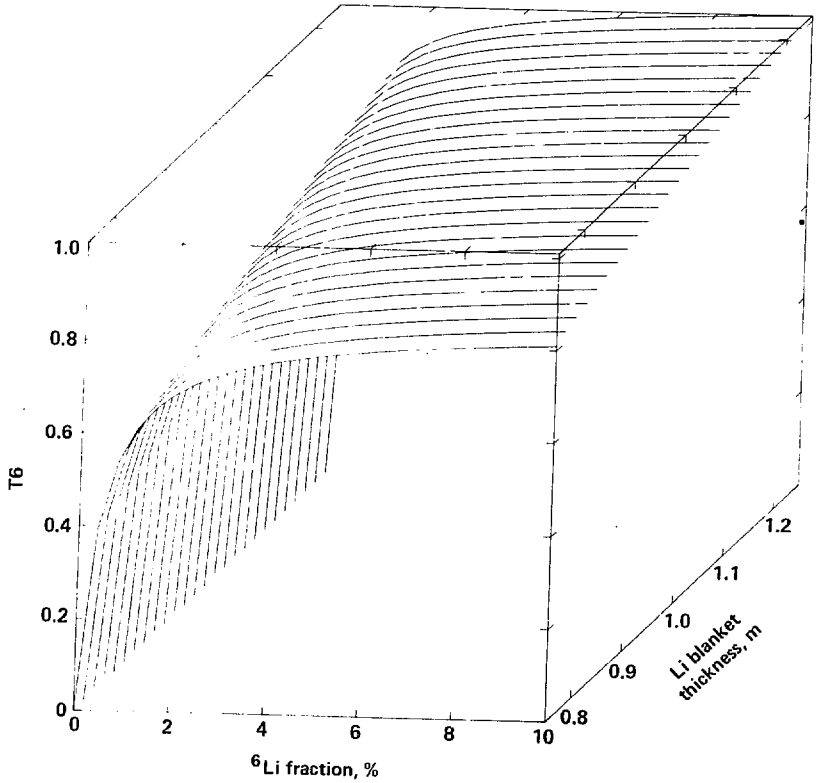

Fig. 4.6 ^{6}Li(n,T)α reactions per DT reaction as a function of the ^{6}Li fraction and Li blanket thickness.

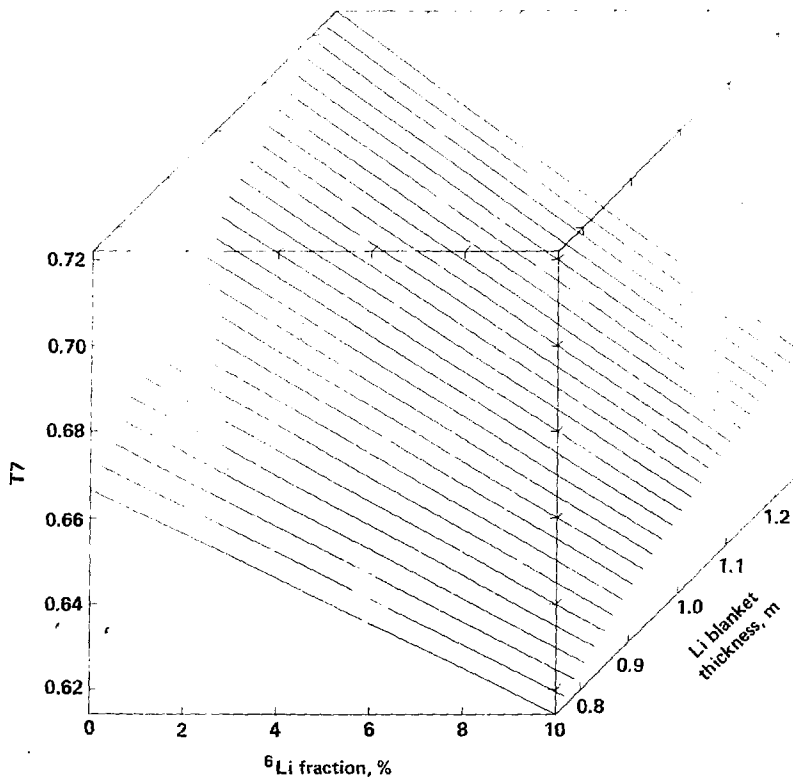

Fig. 4.7 ^{7}Li(n,n'T)α reactions per DT reaction as a function of the ^{6}Li fraction and the Li blanket thickness.

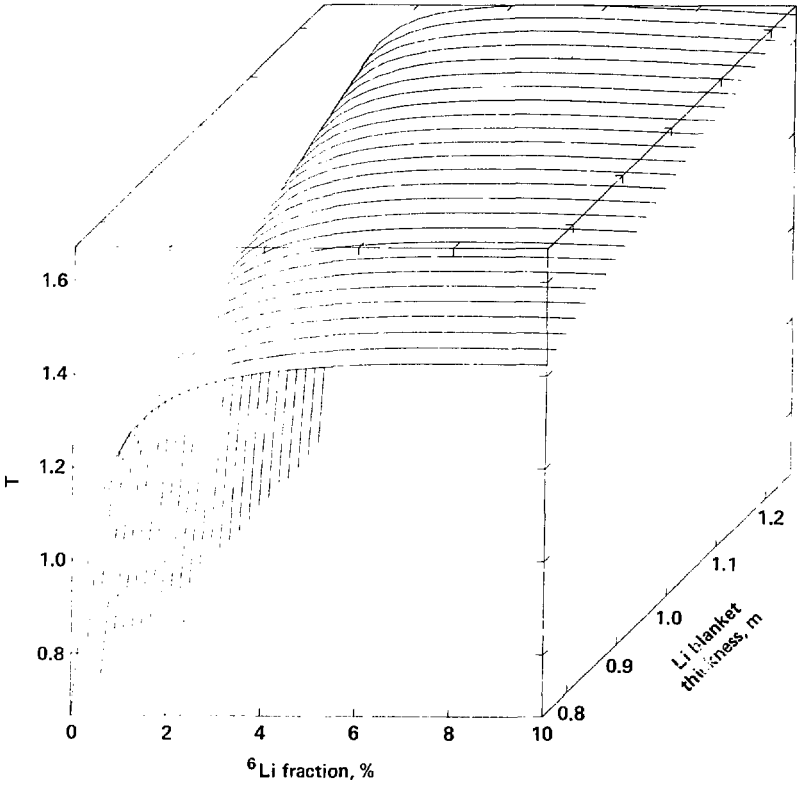

Fig. 4.8 Tritium breeding ratio as a function of the ^{6}Li fraction and the Li blanket thickness.

however, are visible. Note how at x_2 = 1.25 m, T goes through a broad maximum as x_1 increases, indicating that T7 is falling faster than T6 is rising in this region.

A contour plot of the tritium breeding ratio is shown in Fig. 4.9. The first solid line is T = 1.05, the constraint on the breeding ratio. At low ^{6}Li fractions T is primarily a function of the ^{6}Li fraction whereas above ~5% ^{6}Li, T is primarily dependent on the blanket thickness.

The displacement damage rate, dpa per full-power-year, is shown in Fig. 4.10 as a function of the two design variables. As indicated, the dpa rate decreases with increasing ^{6}Li fraction and increasing blanket thickness. The contour plot, Fig. 4.11, gives a better indication of the nature of the dependence of damage rate on the two design variables. It is clear that the dpa rate depends primarily on the blanket thickness. This is due to the nature of the displacement damage cross section. Most of the displacement damage results from high energy neutrons. Hence simply moderating the fusion neutrons is sufficient to decrease the dpa rate significantly. Increasing the ^{6}Li fraction attenuates the neutron flux reaching the first wall by absorbing neutrons in ^{6}Li(n,T)α reactions. Since ^{6}Li more readily captures lower energy neutrons, the dpa rate decreases only slightly with increasing ^{6}Li fraction. The dashed line is the displacement damage rate constraint of 9.5 dpa/yr.

Next, consider the energy deposited in the chamber. Figures 4.12 and 4.13 show the neutron energy deposited in ^{6}Li and ^{7}Li. The features of these surfaces are similar to those for T6 and T7. The energy deposited in the first structure wall and the Na cooled steel

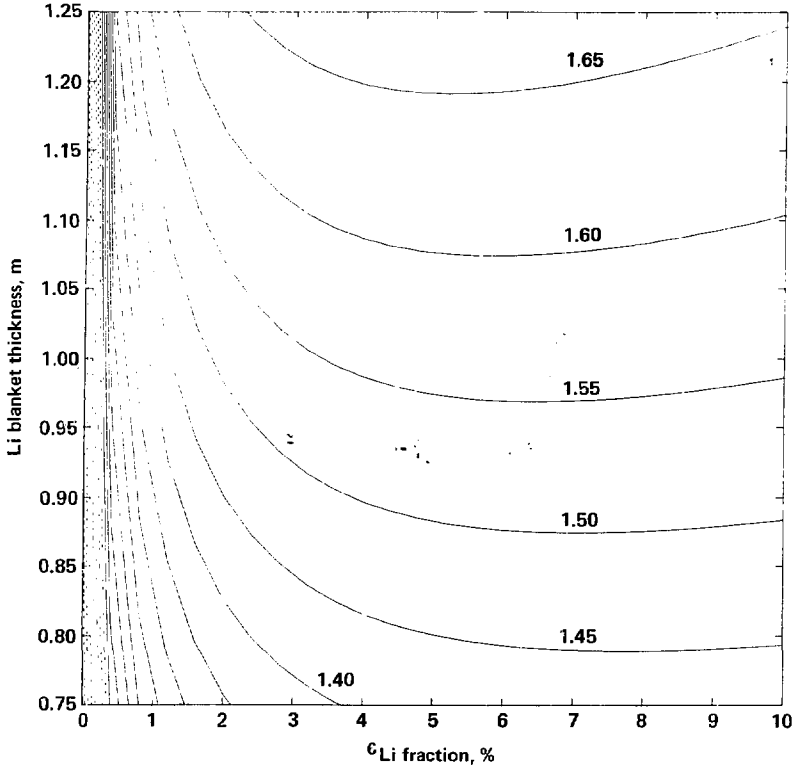

Fig. 4.9 Contour plot of the tritium breeding ratio for the modified HYLIFE chamber.

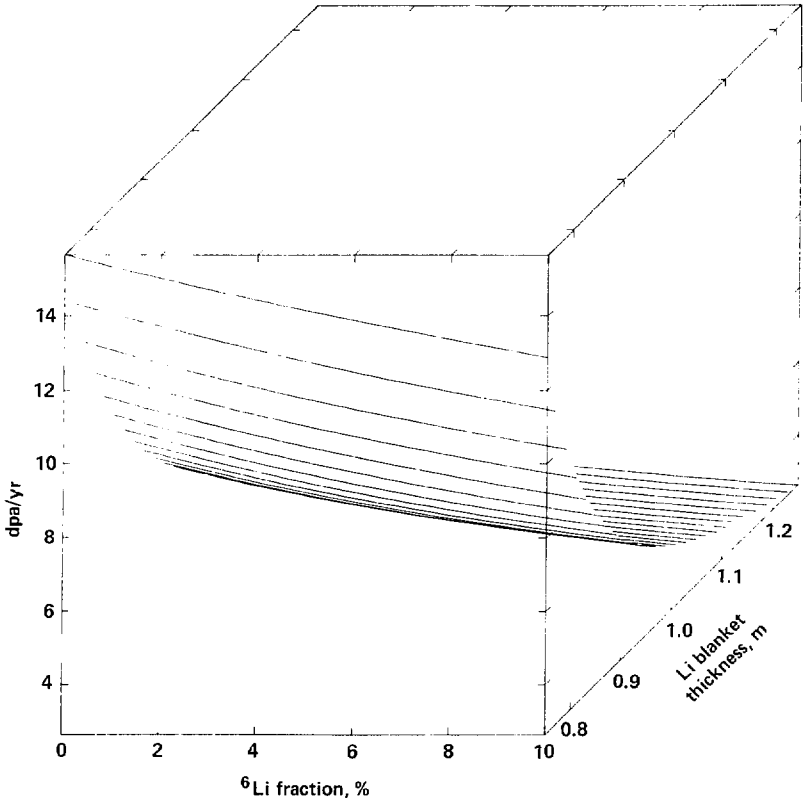

Fig. 4.10 Displacement damage rate in dpa per full-power-year as a function of the ^{6}Li fraction and the Li blanket thickness.

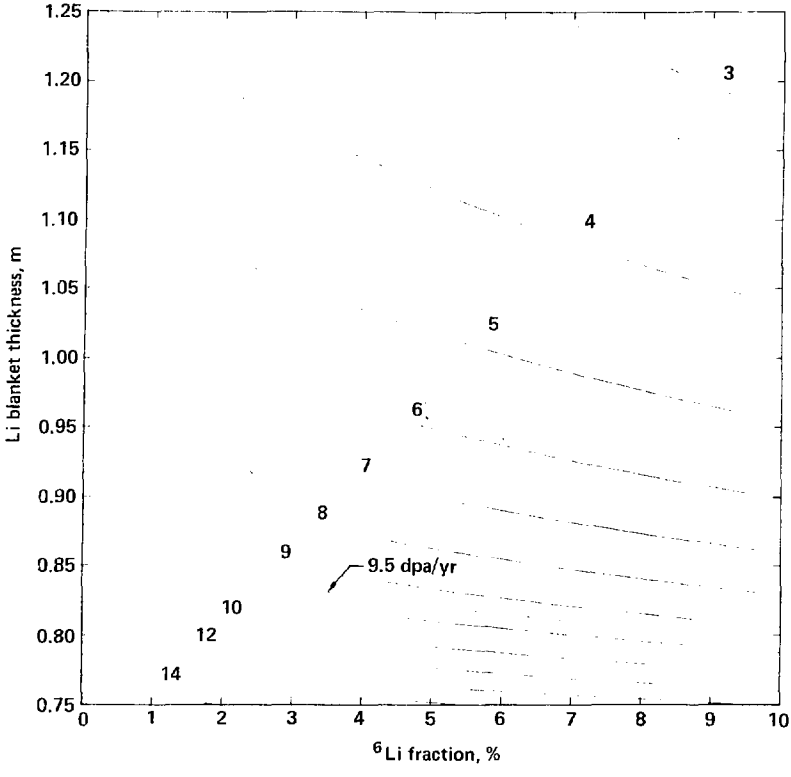

Fig. 4.11 Contour plot of the displacement damage rate. For a 30 year wall life, the damage rate must be less than 9.5 dpa/yr.

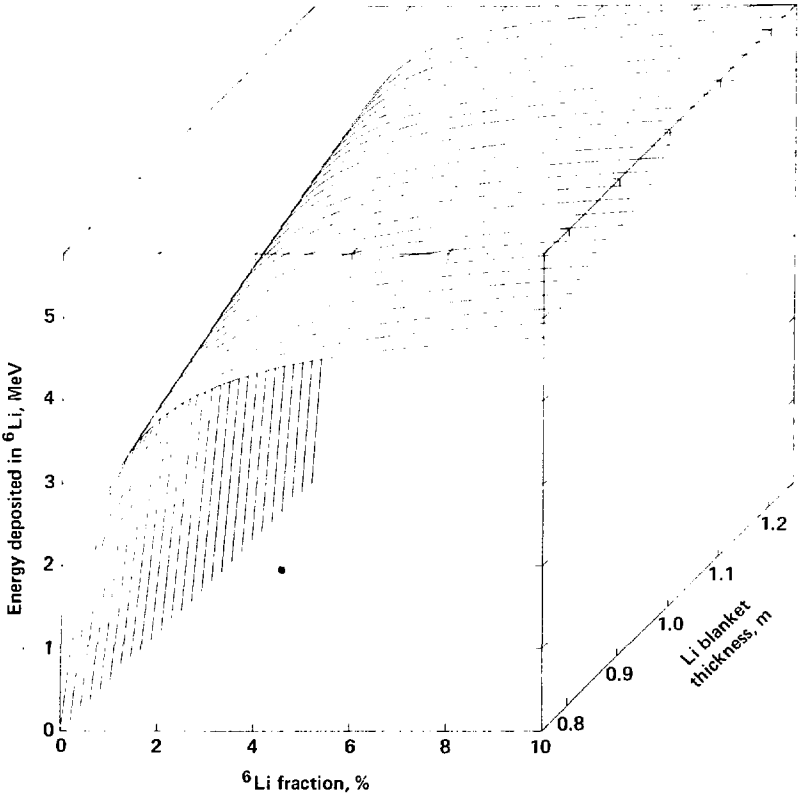

Fig. 4.12 Energy deposited in ^{6}Li as a function of the ^{6}Li fraction and the Li blanket thickness.

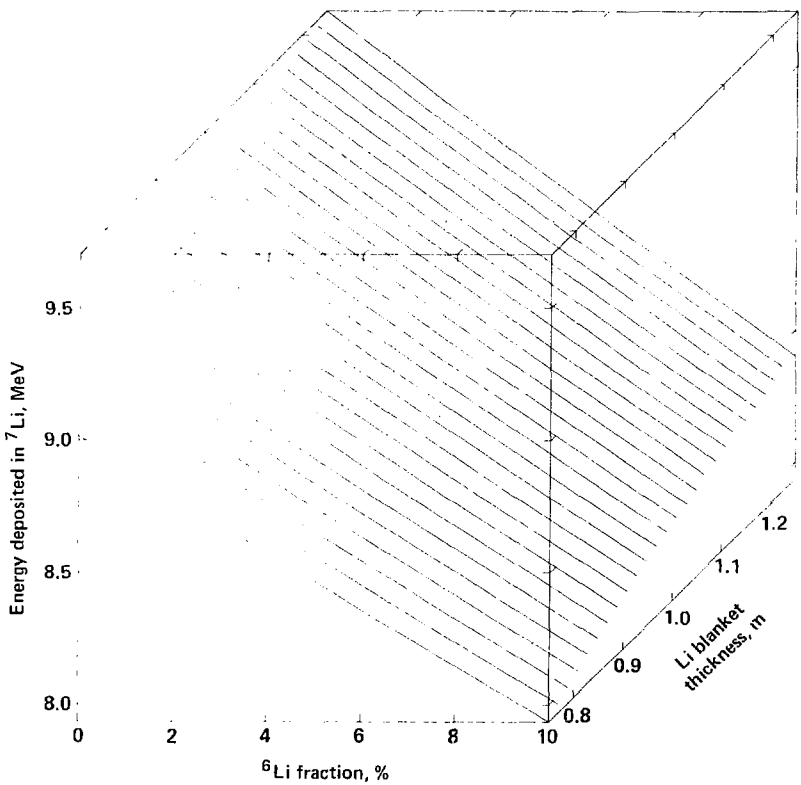

Fig. 4.13 Energy deposited in ^{7}Li as a function of the ^{6}Li fraction and the Li blanket thickness.

blanket is shown in Fig. 4.14. The energy deposited in these regions is primarily due to the energy released in neutron capture reactions in Fe and Mn. As indicated, the energy deposition in these regions increases with decreasing ^{6}Li fraction and with decreasing Li blanket thickness. This follows since decreasing the ^{6}Li fraction and the Li blanket allows more neutrons to penetrate the Li blanket and be captured in structures.

The total energy deposited in the chamber is shown in Fig. 4.15. It includes the neutron energy deposited in the compressed fuel of the target (1.84 MeV), the fusion alpha particle energy (3.52 MeV), and the ^{56}Mn decay energy. The ^{56}Mn decay energy is 2.5 MeV per $^{55}Mn(n,\gamma)$ capture reaction. In general, the total energy deposition increases with decreasing ^{6}Li and Li blanket thickness.

At very low ^{6}Li concentrations, however, the energy deposition begins to fall off. This is due to the nature of the variational estimates in the extrapolated region ($x_1 < 0.5\%$) and is not based on the physical situation. The variation interpolation estimate for the energy deposition in ^{6}Li must go to zero as the ^{6}Li fraction goes to zero. The variational estimate of the energy deposition in structures, however, has no additional boundary condition at low ^{6}Li fractions, and hence the extrapolation to values below $x_1 = 0.5\%$ does not rise as steeply as would be expected based on the number of neutrons penetrating the Li blanket as the number of $^{6}Li(n,T)\alpha$ reactions falls to zero.

To get a more accurate estimate of the total energy deposition, especially at low ^{6}Li fractions, a neutron balance approach is used. The number of available neutrons per DT fusion reaction is 1.00

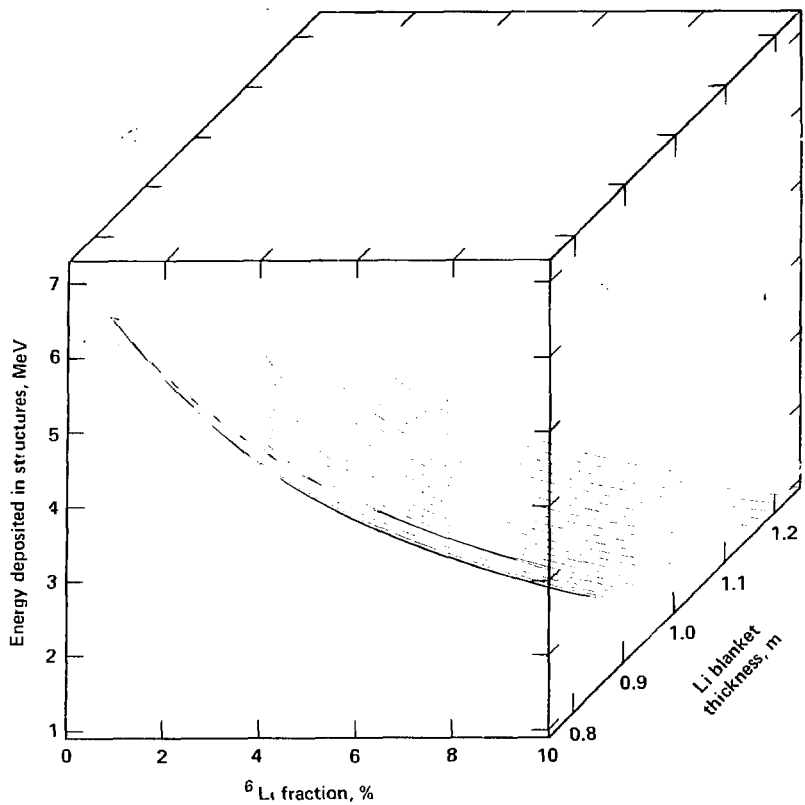

Fig. 4.14 Energy deposited in structures as a function of the ^{6}Li fraction and Li blanket thickness.

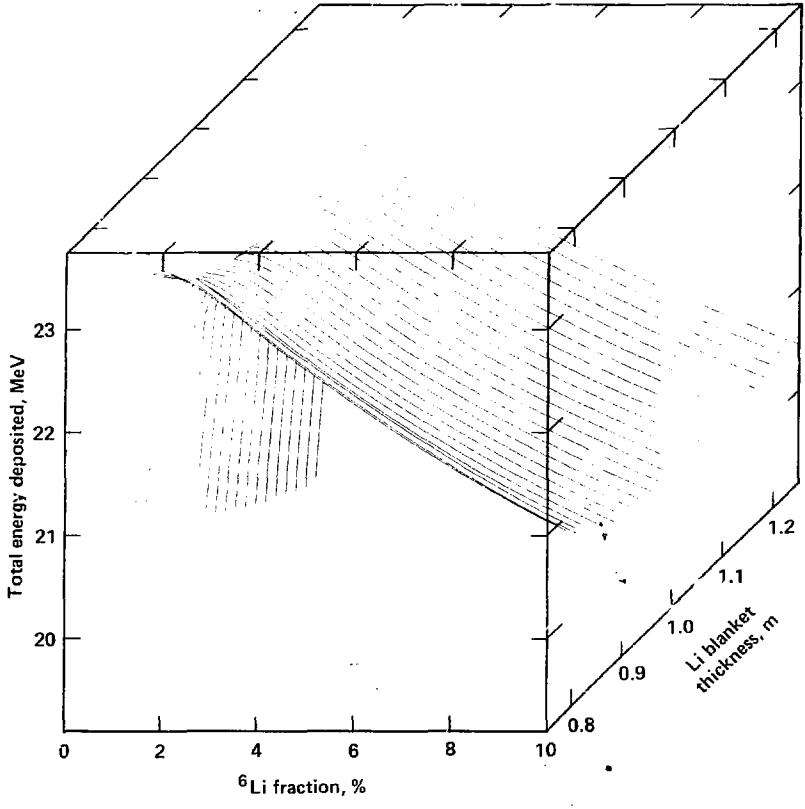

Fig. 4.15 Total energy deposited in the chamber per DT reaction as a function of the two design variables. The 3.5 MeV alpha particle energy and Mn decay energy are included.

from the fusion reaction, plus 0.05 from (n,2n) reactions with D and T in the compressed fuel of the target, plus 0.06 from (n,2n) reactions with ^{7}Li in the Li blanket for a total of 1.11.

There are three primary neutron sinks in the chamber; neutrons can be captured in ^{6}Li(n,T)α, Fe(n,γ) and Mn(n,γ) reactions. The sum of these three reactions for the four reference point transport calculations listed in Table 4.4 is essentially constant (to within 1%) with an average value of 1.114.

In the neutron balance method, the number of ^{6}Li(n,T)α reactions is estimated using variational interpolation and then the number of neutrons available for capture in Fe or Mn is calculated from,

$$N = 1.114 - T6. \tag{4.16}$$

Also note from Table 4.4 that Mn capture reactions are always ~49% of the total capture in Fe and Mn. Each Fe(n,γ) reaction releases ~7.7 MeV and each Mn(n,γ) reaction releases ~7.3 MeV. In addition, each Mn capture leads to a β^{-} decay which releases 2.5 MeV of recoverable energy. Therefore, the energy deposited in structures due to neutron capture and ^{56}Mn decay is

$$E_c = 7.7(0.51)N + 9.8(0.49)N,$$

or

$$E_c = 8.73N. \tag{4.17}$$

Summing the energy deposited in the first wall, steel blanket and Mn decay listed in Table 4.5 gives a total energy deposition which is

somewhat higher than predicated by Eqs. 4.16 and 4.17 when the value of T6 from Table 4.4 is used. This additional energy, which can be viewed as deposition due to scattering reactions in these regions, must be added to E_c to get the correct total energy deposition in the structures. The additional energy for reference point cases 1-4 are 0.96, 0.92, 0.09, and 0.16 MeV, respectively.

The neutron balance estimate of the energy deposited in the first wall and steel blanket is shown in Fig. 4.16. This surface shows the sharp rise in energy deposition as the ^{6}Li approaches zero as expected. The improved estimate of the total energy deposited in the chamber is shown in Fig. 4.17. It increases with decreasing ^{6}Li fraction and decreasing Li blanket thickness over the entire range of x_1 and x_2.

A contour plot of the fusion energy multiplication factor, M_f, is given in Fig. 4.18. This figure clearly shows the sharp rise at low ^{6}Li concentrations.

4.3.2 Optimal Design Point.

Based on the previous results the figure of merit is calculated as a function of the two design variables as shown in Fig. 4.19. Recall that low values of F, the normalized capital cost per net electric power production, are desirable. As seen in Fig. 4.19, F decreases with decreasing ^{6}Li fraction and Li blanket thickness. A contour plot of F is shown in Fig. 4.20.

The constraints on the tritium breeding ratio and displacement damage rate limit the degree to which the ^{6}Li fraction and blanket thickness can be decreased in the attempt to decrease F. Figure 4.21 shows these two constraints overlaid on the contour plot of F. Note

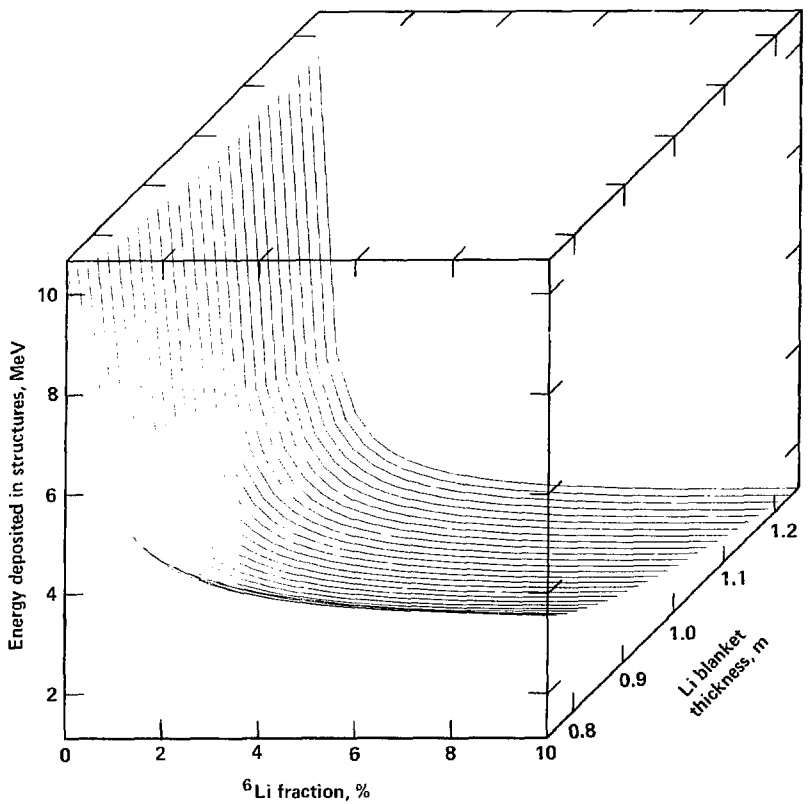

Fig. 4.16 Energy deposited in structures as a function of the two design variables using the neutron balance method.

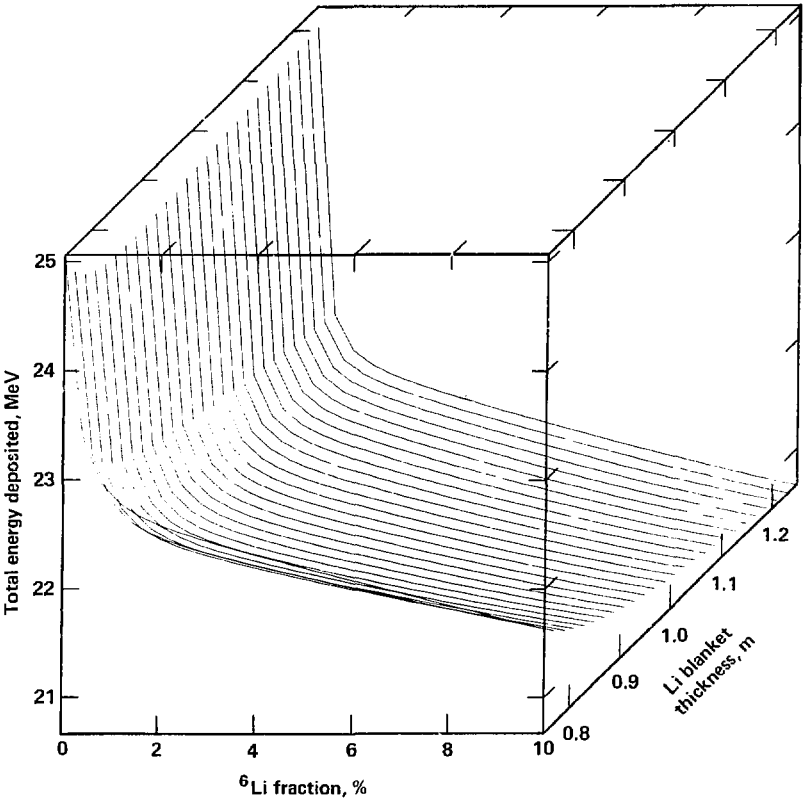

Fig. 4.17 Total energy deposited in the chamber per DT reaction using the neutron balance method.

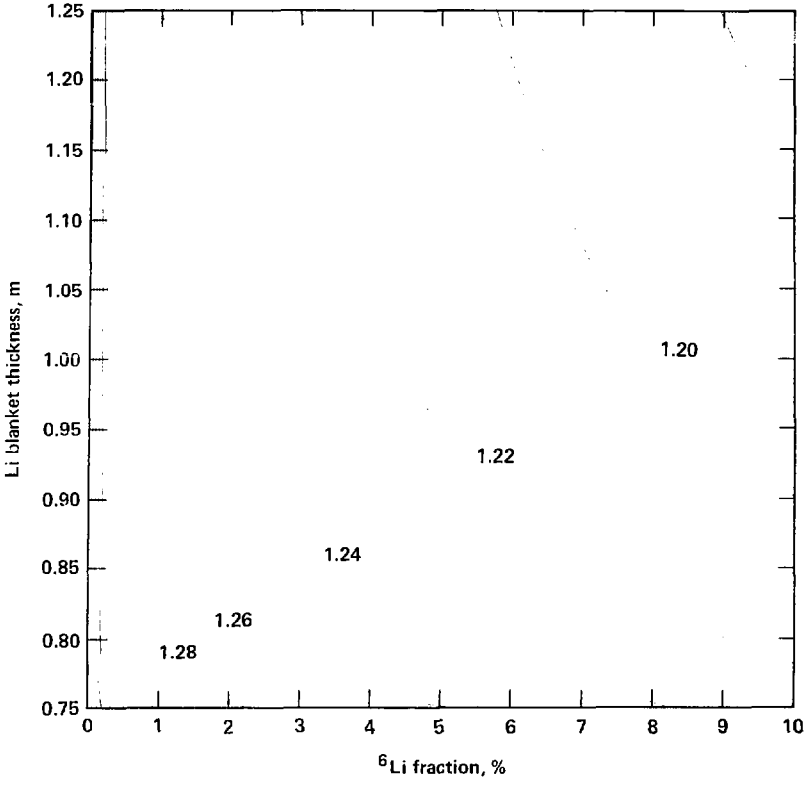

Fig. 4.18 Contour plot of the fusion energy multiplication factor for the modified HYLIFE chamber.

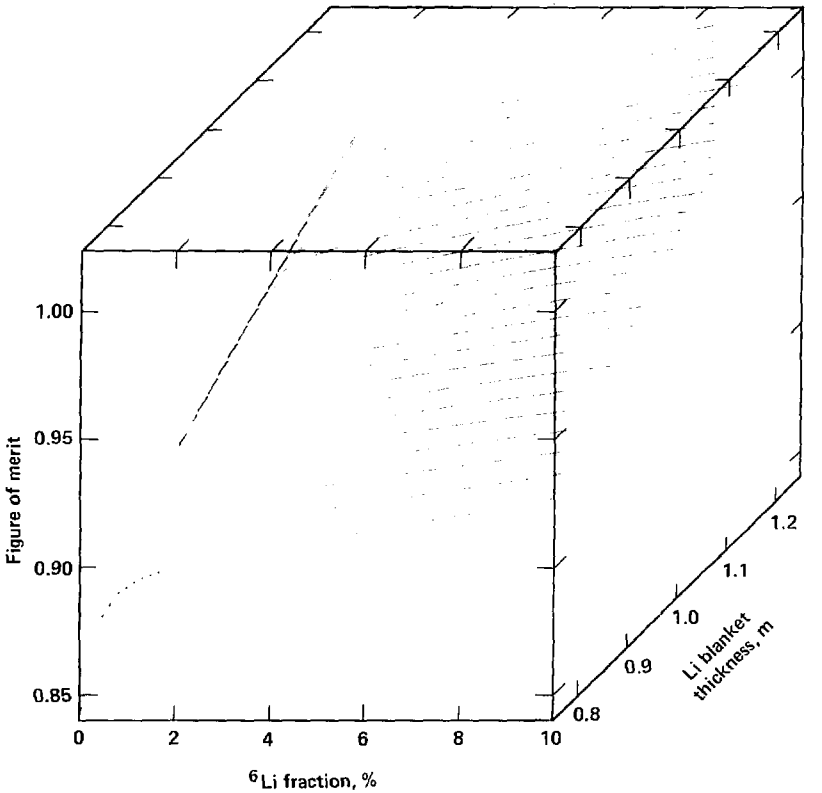

Fig. 4.19 Figure of merit as a function of the ^{6}Li fraction and the Li blanket thickness. The figure of merit is a normalized capital cost per unit of net electric power production.

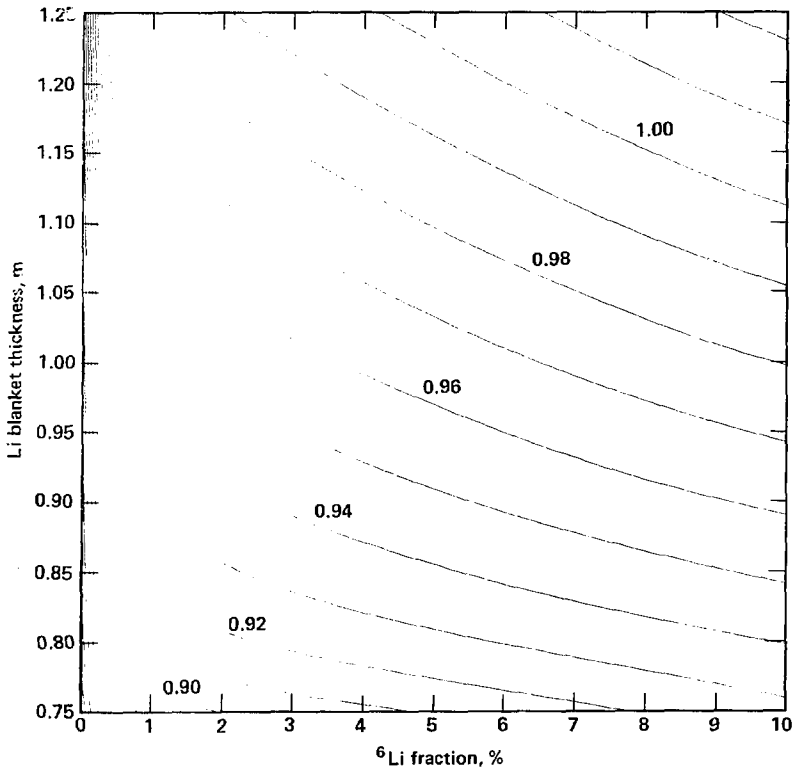

Fig. 4.20 Contour plot of the figure of merit for the modified HYLIFE chamber.

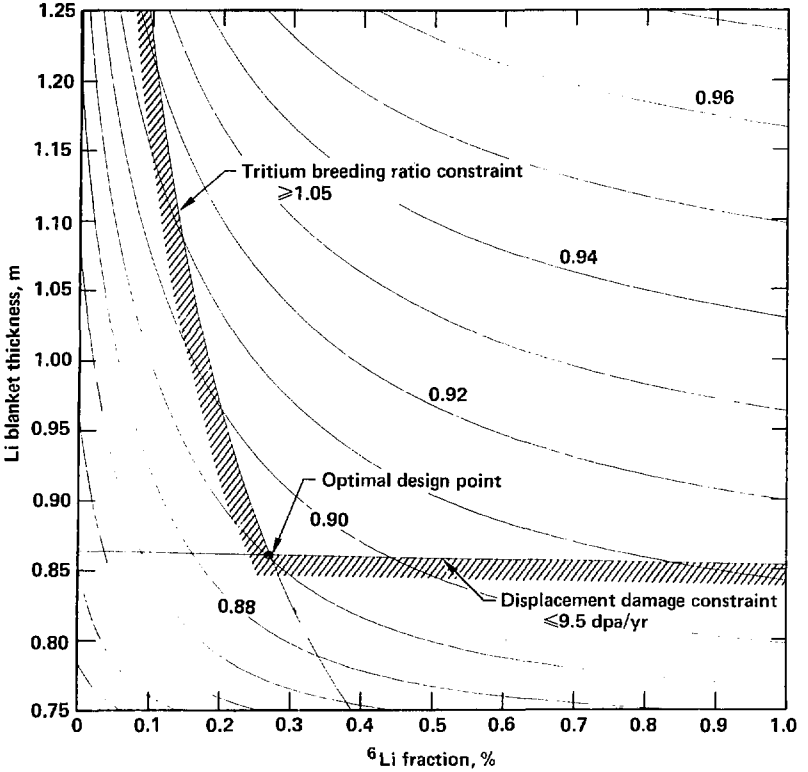

Fig. 4.21 First estimate of the location of the optimal design point. The point lies the intersection of the tritium breeding and displacement damage constraints.

the scale of the horizontal axis has been changed in order to focus on the region of interest. The optimal design point lies at the intersection of the two constraints. The optimal ^{6}Li concentration is 0.27% and the optimal Li blanket thickness if 0.86 m. At this point the modified HYLIFE plant costs 4.8% more than HYLIFE but produces 16% more electric power. The power plant cost per unit of net electric power is, therefore, reduced by 10%, and the figure of merit is 0.90.

4.3.3 Comparison to Transport Calculation at Optimal Point.

In order to check the accuracy of the result an additional neutron transport calculation was carried out for these conditions, i.e., x_1 = 0.27% and x_2 = 0.86 m. The results of the neutron transport calculation are compared with the estimated parameters in Table 4.6.

The variational estimate of the number of $^{6}Li(n,T)\alpha$ reactions is low by ~17%. This relatively large error is not totally surprising considering the steepness of the T6 surface at such low ^{6}Li concentrations (see Fig. 4.6). In particular, T6 increases by 0.8 per 1% increase in ^{6}Li fraction in this region. On the other hand the number of tritium breeding reactions with ^{7}Li is predicted quite accurately. The actual tritium breeding ratio thus exceeds the required 1.05 by 0.074 and the breeding ratio constraint is satisfied.

The neutron capture rate in Mn and Fe is overestimated. This is a direct result of underestimating T6 since the neutron balance method is used to calculate these rates.

The underestimate of the energy deposited in ^{6}Li is consistent with underestimating T6. The estimated energy deposition in ^{7}Li is very close to the transport calculation result. The energy deposited

Table 4.6

Comparison of neutronic performance at x_1 = 0.27%, x_2 = 0.86 m

	TART	Estimated
Reactions[a]		
$^6Li(n,T)\alpha$	0.441 (1.2)[2]	0.368
$^7Li(n,n'T)\alpha$	0.683 (1.2)	0.682
T	1.124	1.050
Mn(n,Y)	0.318 (1.2)	0.366
Fe(n,Y)	0.336 (1.4)	0.380
Energy Deposition,[a] MeV		
Target	1.85 (0.4)	1.84
^6Li	2.12 (1.2)	1.64
^7Li	9.22 (0.8)	9.19
Structures[b]	6.48 (1.4)	6.81
Alpha particle	3.52	3.52
TOTAL	23.19	23.00
Displacement damage rate[c]	10.82	9.50

a) per DT fusion reaction.

b) Energy deposited in first structural wall and steel blanket including Mn decay energy.

c) dpa per full-power-year based on 2700 MW of fusion power.

d) percent standard deviation.

in the first structural wall and steel blanket including ^{56}Mn decay is overestimated by ~5%. The errors in estimating the energy deposition nearly cancel and the total is low by less than 1%. The final parameter is the displacement damage rate. It is underestimated by ~12%. This means that the displacement damage rate constraint is not really met at this point.

Based on this comparison some conclusions can be drawn with respect to the location of the optimal design point. Since the tritium breeding ratio is higher than required, the ^{6}Li concentration could in fact by lowered below 0.27%. Also since the displacement damage rate is not met, the Li blanket must be made somewhat thicker than 0.86 m. This then will allow an even greater reduction in the ^{6}Li concentration. A better estimate of the location of the optimal design point is made in the next section.

4.4 IMPROVED ESTIMATES OF LOCATION OF OPTIMUM

4.4.1 Improved Estimate Using Taylor Expansion at Original Optimal Point.

An improved estimate of the location of the optimal design point can be made by making use of the results of the additional transport calculation discussed in the previous section and tabulated in Table 4.6. Since the location of the optimal design point is at the intersection of the two constraints, the objective is to produce a better estimate of point at which T = 1.05 and D = 9.50. This can be done by expanding T and D in first order Taylor Series in the two design variables.[70] The required partial derivatives are approximated by finite differences between points bounding the original optimal design point, i.e. x_1 = 0.27% and x_2 = 0.86 m. The values of T and D at these adjacent points are calculated using successive variation interpolation as in the previous section.

The Taylor Series expansions for T and D are[70]

$$T(x_1,x_2) = T(x_{1o},x_{2o}) + T'_{x1}\Delta x_1 + T'_{x2}\Delta x_2, \qquad (4.18)$$

and

$$D(x_1,x_2) = D(x_{1o},x_{2o}) + D'_{x1}\Delta x_1 + D'_{x2}\Delta x_2, \qquad (4.19)$$

where,

(x_1,x_2) = New optimal design point,

(x_{1o},x_{2o}) = (0.0027,0.86) = original optimal design point,

$T(x_1,x_2)$ = 1.05 = tritium breeding ratio constraint,

$D(x_1,x_2)$ = 9.50 = displacement damage rate constraint,

$T(x_{1o},x_{2o})$ = 1.124 = TART result,

$D(x_{1o},x_{2o})$ = 10.82 = TART result,

T'_{x1} and D'_{x1} = partial derivatives of T and D with respect to x_1 at the point (x_{1o},x_{2o}),

T'_{x2} and D'_{x2} = partial derivatives of T and D with respect to x_2 at the point (x_{1o},x_{2o}),

$\Delta x_1 = (x_1 - x_{1o})$, and

$\Delta x_2 = (x_2 - x_{2o})$.

The partial derivatives at (x_{1o},x_{2o}) are

$T'_{x1} = 79.8$,

$D'_{x1} = -35.7$,

$T'_{x2} = 0.645$, and

$D'_{x2} = -33.7$.

These were calculated from the variations in T and D between x_1 = 0.24 and 0.30% with x_2 = 0.86, and between x_2 = 0.85 and 0.87 with x_1 = 0.27%.

Substituting the above partials and the known values for T and D, Eqs. 4.18 and 4.19 reduce to

$$-0.074 = 79.8\Delta x_1 + 0.645\Delta x_2, \tag{4.20}$$

and

$$-1.32 = -35.7\Delta x_1 - 33.7\Delta x_2. \tag{4.21}$$

Solving for Δx_1 and Δx_2 gives $\Delta x_1 = -0.00136$, and $\Delta x_2 = 0.041$. The new optimal design point is, therefore, x_1 = 0.14%, and x_2 = 0.90 m.

4.4.2 Improved Estimate Using New Set of Four Reference Points.

As previously noted, the original estimate of the optimal design point, i.e., x_1 = 0.27% and x_2 = 0.86 m, did not fall between the reference values for the ^6Li fraction, i.e., 0.5 and 7.42%. Hence the neutronic performance in the vicinity of the optimal point was estimated based on extrapolations on x_1. An improved estimate of the location of the optimal design point is obtained if it falls within the rectangle defined by the four reference points. In this section the two reference value for x_1 are 0.07% and 0.5%, which, based on the results of the previous section, i.e., x_{1o} = 0.14%, should bound the optimal ^6Li fraction.

The results of the two new reference point transport calculations are tabulated in Tables 4.7 and 4.8. Comparing these results to the results given in Tables 4.4 and 4.5 reveals that the $^7Li(n,n'T)\alpha$ reaction rate, the energy deposited in ^7Li, and the displacement damage rate are independent of x_1 in this range. That is, the variations are less than one standard deviation for the Monte Carlo result. Hence in evaluating the figure of merit and constraints, these parameters are only functions of x_2 and are estimated using two point interpolation on x_2. In each case, the average of the results at x_1 = 0.07 and 0.5% serves as the reference value for interpolation on x_2. These average reference values are listed in Table 4.9.

The neutron balance method described in section 4.3 is also used here to estimate the energy deposition in structures. In this case, however, the average number of available neutron is 1.101 compared to

Table 4.7

Reaction rates and neutron damage rates for

x_1 = 0.07%, x_2 = 0.75 and 1.25 m

Reference Point	5	6
^{6}Li Fraction, %	0.07	0.07
Li Thickness, m	0.75	1.25
Reactions per DT reaction		
^{6}Li(n,T)α	0.229 (1.9)[a]	0.503 (1.6)
^{7}Li(n,n'T)α	0.680 (0.8)	0.709 (1.0)
^{7}Li(n,Y)	0.013 (1.7)	0.029 (1.5)
Mn(n,Y)	0.403 (1.3)	0.253 (1.8)
Fe(n,Y)	0.444 (1.2)	0.297 (1.7)
Displacement Damage Rate[b]	15.6 (3)	3.97 (8)

a) percent standard deviation.

b) dpa per full-power-year based on 2700 MW of fusion power.

Table 4.8

Energy deposition for x_1 = 0.07%, x_2 = 0.75 and 1.25 m

Reference Point	5	6
^{6}Li Fraction, %	0.07	0.07
Li Thickness, m	0.75	1.25
Energy Deposition[a]		
Target	1.83 (0.4)[b]	1.84 (0.4)
^{6}Li	1.12 (1.9)	2.43 (1.6)
^{7}Li	8.99 (0.5)	9.62 (0.6)
First wall	1.12 (1.6)	0.81 (1.7)
Steel blanket	6.37 (1.4)	3.62 (1.8)
Mn decay	1.01	0.63
Alpha particle	3.52	3.52
TOTAL	23.96	22.47

a) MeV per DT reaction.

b) percent standard deviation.

Table 4.9

Reference results used to interpolate on x_2

Parameter	0.75 m	1.25 m
$^7Li(n,n'T)\alpha$ reactions	0.672	0.713
Energy deposition in ^7Li, MeV	8.98	9.63
Displacement damage rate, dpa/yr	15.52	3.96

1.114 used previously. Also at 0.07% ^{6}Li, neutron capture in ^{7}Li becomes significant (i.e., > 1%) and is therefore included as a sink in the neutron balance. Finally Mn accounts for 48% of the captures in Mn and Fe compared to 49% in the previous case.

The expression for energy deposition in structures due to neutron capture and ^{56}Mn decay is

$$E = 8.71(1.101 - T6 - C7), \text{ MeV}, \tag{4.22}$$

where

C7 = neutron capture in $^{7}Li(n,\gamma)$ reactions.

Compare this to Eqs. 4.16 and 4.17. As before, T6 and C7 are estimated using variational interpolation.

The direct neutron energy deposition is equal to the difference between the result obtained with Eq. 4.22 and the sum of the tabulated energy deposition in the steel wall, in the steel blanket, and due to Mn decay.

The resulting contour plot of the figure of merit is shown in Fig. 4.22. The displacement damage rate and tritium breeding constraints have been overlaid. In this case, the optimal design point is located at x_1 = 0.13% and x_2 = 0.86 m. The ^{6}Li concentration agrees more closely with the improved estimate obtained in the previous section, i.e., 0.14%. The optimal Li blanket thickness however, is the same as the original estimate. This is as expected since the blanket thickness is limited by the displacement damage rate which in this range is independent of the ^{6}Li fraction. Hence, the two new transport calculations at different values of ^{6}Li

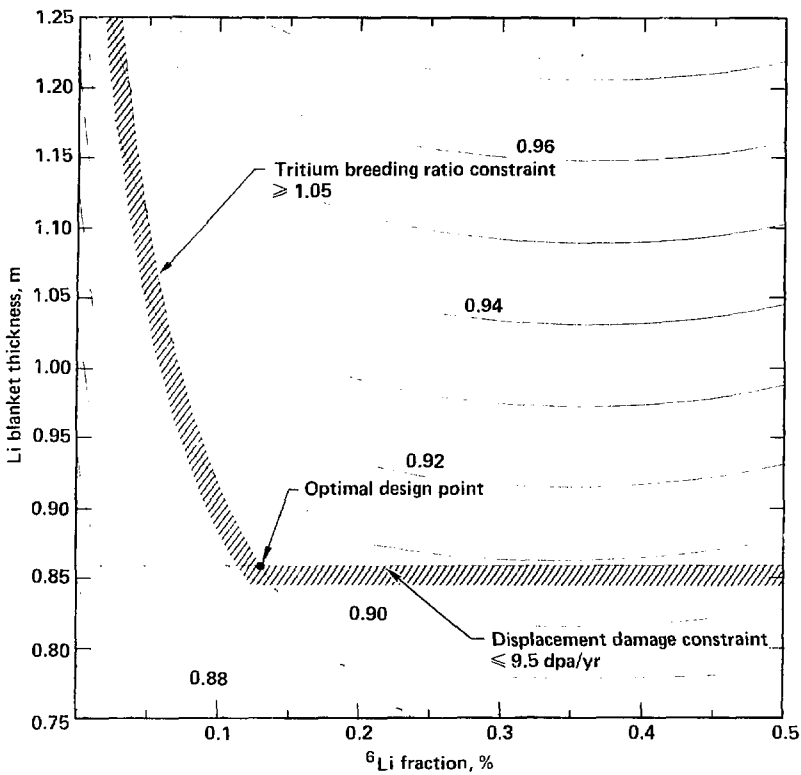

Fig. 4.22 Third estimate of the location of the optimal design point.

fraction did not add any new information relative to the damage rate.

To get an improved estimate of the displacement damage rate as a function of thickness requires additional transport calculations at an intermediate value of x_2. This is discussed in the next section.

4.4.3 Using Three Point Interpolation on One Variable.

In this section the optimal design point is estimated using three point interpolations on x_2 followed by two point interpolations on x_1. Two new transport calculations were carried out with x_2 = 1.00 m; one with x_1 = 0.07%, and one with x_1 = 0.5%. The results at these points are given in Tables 4.10 and 4.11.

Note that the number of $^6Li(n,T)\alpha$ reactions varies linearly with the Li blanket thickness in this range. Therefore T6 is estimated by a two point interpolation on x_1 between two linear expressions in x_2, one at x_1 = 0.07% and one at x_1 = 0.5%. The energy deposition in ^6Li is also linear in x_2 and thus estimated in the same manner as T6.

As before T7, E7 and the displacement damage rate are independent of the ^6Li fraction at these low concentrations. Note that the variation in the displacement damage rate at 1.00 m is within the 6% standard deviation. The average values for T7, E7 and displacement damage rate at 1.0 m are 0.709, 9.46 MeV and 7.34 dpa/yr. These, along with the values listed in Table 4.9, serve as the reference points for three point interpolation on x_2. Also, the neutron balance method, Eq. 4.22, is used to calculate the energy deposition in structures.

Table 4.10

Reaction rates and neutron damage rates for x_1 = 0.07 and 0.50% with x_2 = 1.00 m

Reference Point	7	8
^{6}Li Fraction, %	0.07	0.50
Li Thickness, m	1.00	1.00
Reactions per DT reaction		
^{6}Li(n,T)α	0.366 (1.5)[a]	0.588 (1.0)
^{7}Li(n,n'T)α	0.704 (1.3)	0.713 (1.2)
^{7}Li(n,Y)	0.021 (1.3)	0.009 (1.0)
Mn(n,Y)	0.325 (1.3)	0.253 (2.5)
Fe(n,Y)	0.370 (1.2)	0.262 (2.3)
Displacement damage rate[b]	7.57 (6)	7.11 (6)

a) percent standard deviation.

b) dpa per full-power-year based on 2700 MW of fusion power.

Table 4.11

Energy deposition for x_1 = 0.07 and 0.50% with x_2 = 1.00 m

Reference Point	7	8
^{6}Li Fraction, %	0.07	0.50
Li Thickness, m	1.00	1.00
Energy Deposition[a]		
Target	1.83 (0.4)[b]	1.82 (0.5)
^{6}Li	1.75 (1.5)	2.98 (1.0)
^{7}Li	9.52 (0.8)	9.40 (0.8)
First wall	0.96 (1.9)	0.53 (1.9)
Steel blanket	4.81 (1.4)	3.77 (2.0)
Mn decay	0.81	0.63
Alpha particle	3.52	3.52
TOTAL	23.20	22.65

a) MeV per DT reaction

b) percent standard deviation.

The resulting figure of merit contour plot with constraints is shown in Fig. 4.23. In this case the predicted optimal design point is x_1 = 0.09% and x_2 = 0.91 m. Note that the value of x_2 increased to lower the dpa rate as expected. The results of this final estimate are compared to the results of a transport calculation at this design point in the next section.

A transport calculation was carried out with a Li blanket thickness of 0.91 m and a ^{6}Li fraction of 0.09% in order to check the estimated results at the optimal design point..

The neutronic performance is compared in Table 4.12. All the results agree quite closely. The tritium breeding ratio is off by ~0.5%, the total energy deposition is within 1% of the transport calculation result, and the dpa rate is high by ~0.5%. The close agreement in the dpa rate is somewhat fortuitous considering that the standard deviation in the result is ~5%.

Based on the agreement with the transport calculation the optimal design point of 0.09% ^{6}Li and a blanket thickness of 0.91 m is quite acceptable.

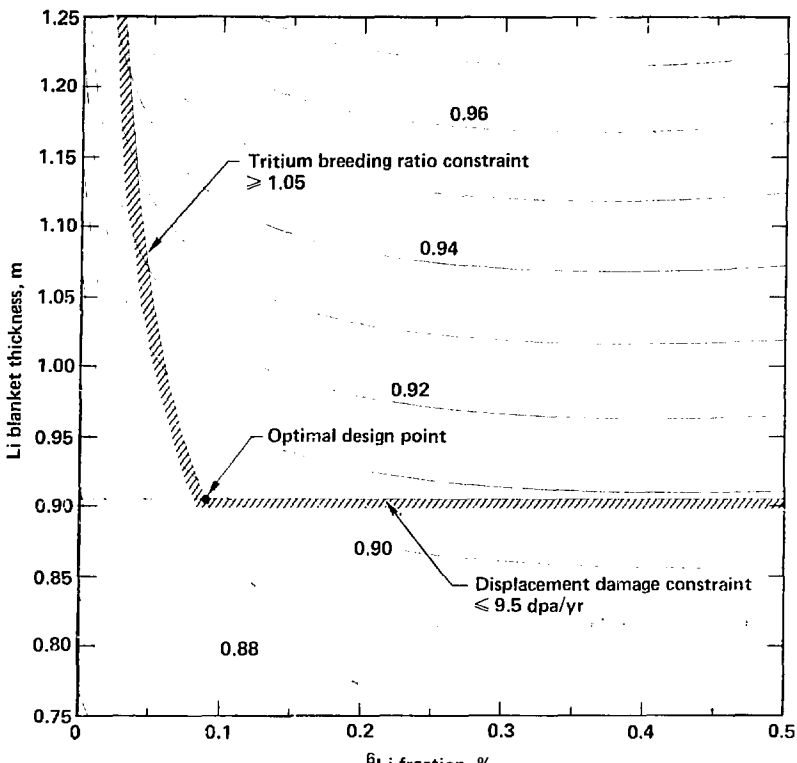

Fig. 4.23 Fourth estimate of the location of the optimal design point.

Table 4.12

Comparison of TART and estimated results at $x_1 = 0.09\%$ and $x_2 = 0.91$ m

	TART	Estimated
Reactions per DT reaction		
$^6Li(n,T)\alpha$	0.357 (1.7)[c]	0.350
$^7Li(n,T)\alpha$	0.698 (0.7)	0.700
T	1.055	1.050
$^7Li(n,\gamma)$	0.016 (1.6)	0.016
Mn(n,γ)	0.353 (1.5)	0.353
Fe(n,γ)	0.390 (1.4)	0.382
Energy deposition[a]		
Target	1.82 (0.4)	1.84
^6Li	1.67 (1.7)	1.70
^7Li	9.45 (0.5)	9.32
Structures	6.17 (1.5)	6.03
Mn decay	0.88	0.88
Alpha particle	3.52	3.52
TOTAL	23.51	23.29
Displacement damage rate[b]	9.45 (5)	9.50

a) MeV per DT reaction.

b) dpa per full-power-year based on 2700 MW of fusion power.

c) percent standard deviation.

4.5 SUMMARY OF OPTIMIZATION RESULTS.

The plant parameters at the final optimal design point are compared to the reference HYLIFE parameters in Table 4.13. With the modified design, the fusion energy multiplication factor is increased to 1.34. As a result, the modified design produces 19.4% more electric power. The plant capital cost, however, is only 6.5% higher for an 10.8% reduction in the cost per kWe. To put this into perspective note that with the modified HYLIFE design the driver and target factory could cost $200 M more (direct) for the same cost of electricity as from HYLIFE.

The various optimal design points described in this chapter are summarized in Table 4.14.

Table 4.13

Comparison of HYLIFE and modified HYLIFE parameters at $x_1 = 0.09\%$ and $x_2 = 0.91$ m

	HYLIFE	Modified HYLIFE
Tritium breeding ratio	1.75	1.05
Neutron energy deposition, MeV	16.9	20.0[a]
Fusion power, MW	2700	2700
Fusion energy multiplication factor	1.16	1.34
Thermal power, MW_t	3130	3607
Thermal conversion efficiency, %	39	39
Gross electrical power, MWe	1220	1407
Laser power consumption, MWe	135	135
Auxiliary power requirements, MWe	75	75
Lithium pumping power, MWe	30	27
Net electrical power, MWe	980	1170
Direct capital costs, $M		
Reactor	960	1075
Lithium pumps	160	146
Laser	330	330
Target factory	100	100
TOTAL	1550	1651

(a) based on results of transport calculation.

Table 4.14

Summary of optimal design points discussed in Chapter 4

Number	Optimal Point x1, %	Optimal Point x2, m	Reference Points x1, %	Reference Points x2, m	Method
1	0.27	0.86	0.50	0.75	Successive two
			0.50	1.25	point interpolation
			7.42	0.75	
			7.42	1.25	
2	0.14	0.90	0.27	0.86	Taylor Series about point 1
3	0.13	0.86	0.07	0.75	Successive two
			0.07	1.25	point interpolation
			0.50	0.75	
			0.50	1.25	
4	0.09	0.91	0.07	0.75	Three point
			0.07	1.00	interpolation on x_2
			0.07	1.25	Two point
			0.50	0.75	interpolation on x_1
			0.50	1.00	
			0.50	1.25	

5. OPTIMIZATION OF THE CASCADE CHAMBER

5.1 DESCRIPTION OF THE PROBLEM

5.1.1 The Cascade Reactor Concept.

The subject of the second optimization problem is another inertial confinement fusion reactor concept called Cascade.[71,72] The primary feature of Cascade (see Fig. 5.1) is a rotating chamber in which a cascading blanket of solid lithium ceramic pebbles breeds tritium, acts as the heat transfer medium, and protects the chamber wall from the damaging effects of neutrons, x-rays and target debris. Pebbles are injected at each end of the chamber, and are held against the wall by centrifugal action. The pebbles cascade toward larger radii and exit through apertures into a stationary pebble catcher. Heat and tritium are removed, and the pebbles are recirculated for reinjection into the chamber. This concept is currently under investigation at Lawrence Livermore National Laboratory, and researchers at GA Technologies are participating in the study under contract.

As reported in the literature,[72] the solid breeding material used in Cascade is Li_2O. While Li_2O is a good tritium breeding material, there are some concerns about the corrosive effects of LiOH which is formed from Li_2O.[73,74] From a compatibility standpoint, a more attractive ceramic tritium breeding material is $LiAlO_2$.[75] Unfortunately, $LiAlO_2$ will not give a tritium breeding ratio greater than one unless a neutron multiplier is placed between the fusion neutron source and the $LiAlO_2$ breeding blanket.[25]

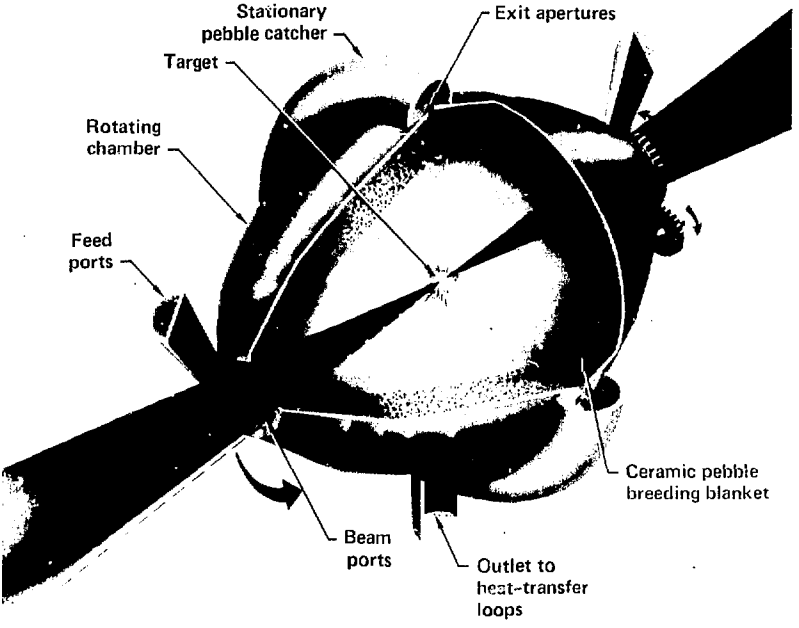

Fig. 5.1 The Cascade chamber.

In this optimization problem, a Cascade chamber using a $LiAlO_2$ breeding blanket and a BeO neutron multiplier is investigated. Beryllium is an excellent neutron multiplier with a threshold of only 1.85 MeV.[76] Beryllium oxide is proposed here to allow for high temperature operation, which is one of the goals of the Cascade concept.[77,78]

A flowing layer of BeO pebbles can be maintained on the surface of the $LiAlO_2$ blanket by fabricating the BeO larger and less dense than the $LiAlO_2$ pebbles.[79] The normal density of BeO is 3.01 g/cm^3, while $LiAlO_2$ has a normal density of 2.55 g/cm^3. Therefore, the BeO pebbles must be fabricated at less than 85% normal density.

Three blanket design variables are considered in the Cascade optimization problem. They are

x_1 = ^6Li fraction in Li,

x_2 = $LiAlO_2$ blanket thickness, m, and

x_3 = BeO multiplier thickness, m.

5.1.2 Figure of Merit for Cascade.

The figure of merit chosen for this design is simply the sum of the $LiAlO_2$ blanket thickness and the BeO multiplier thickness. That is, we seek to minimize

$$F = x_2 + x_3. \tag{5.1}$$

At this stage in the development of the Cascade concept, it is not

possible to optimize a more general system parameter, such as the cost of electricity, since cost estimates for the reactor plant have not yet been made. By minimizing the total blanket thickness (the multiplier is considered part of the blanket) the size of the rotating chamber can be minimized. This inner radius of the blanket is assumed to be fixed by the damaging effects (ablation and vaporization) of the x-rays and target debris.

Pitts previously sought to minimize the size of the chamber from a mechanical and thermal perspective.[80] In this problem, the neutronic perspective is considered.

5.1.3 Constraints on the Design.

Three constraints are imposed on the Cascade design. The first is a requirement for a tritium breeding ratio greater than 1.05. This is the same constraint as used for the modified HYLIFE chamber optimization problem discussed in Chapter 4. The constraint is expressed as,

$$T \geq 1.05. \tag{5.2}$$

The second constraint relates to the mechanical design of the Cascade chamber. GA Technologies recently proposed a concept where the rotating chamber is constructed of individual SiC panels held together by Aℓ tendons.[81] The Aℓ tendons are actually a composite of Aℓ and SiC fibers to increase tensile strength of Aℓ. Based on a temperature limit of 400°C for the tendons, the heat generation rate in the tendons due to neutron and gamma heating must be less than 0.85 W/cm^3.[81] The second constraint is

$$G \leq 0.85 \text{ W/cm}^3. \tag{5.3}$$

The heat rate in the tendons is calculated from,

$$G = E_t P_f / 17.6 V_t, \tag{5.4}$$

where

E_t = energy deposited in the zone representing the Aℓ/SiC tendons, MeV per DT reaction,

P_f = the fusion power, W, and

V_t = volume of the zone representing the tendons, cm^3.

The value 17.6 is the total energy in MeV released per DT reaction. For Cascade, the fusion power is 3000 MW.

A third constraint is placed on the total neutron leakage rate from the Cascade chamber. This parameter gives an indication of the effectiveness of the blanket design in performing one of its primary functions, namely, capturing the fusion neutrons.

The beam ports at the ends of the Cascade chamber provide a direct leakage path from the chamber. The two ports subtend 1.25% of the total solid angle. The neutron leakage through the ports, however, will be greater than 1.25% of the fusion neutron source for two reasons.[82] One is that neutrons entering the blanket can be scattered out through the ports. The second is that neutron multiplication in the BeO region will tend to increase the neutron leakage through the ports.

There will also be some neutron leakage through the $LiAlO_2$ blanket itself. The constraint on the total neutron leakage is set at

0.1 neutrons per DT reaction. That is,

$$L \leq 0.1. \tag{5.5}$$

The constraints given by Eqs. 5.2, 5.3 and 5.5 are evaluated as a function of the three design variables using successive, two point variational interpolation. As such, eight reference point transport calculations are required. The neutronics model for the Cascade chamber is discussed in the next section.

5.2 REFERENCE POINT TRANSPORT CALCULATIONS

5.2.1 Neutronics Model for the Cascade Chamber.

The neutronics model of the Cascade chamber is shown in Fig. 5.2. The football shaped chamber (see Fig. 5.1) is approximated by a sphere. As in the neutronics model for the modified HYLIFE chamber, the 14.1 MeV neutron source is uniformly distributed throughout a region of DT compressed to a density-radius product of 3.0 g/cm^2. The target, zone 1, is located at the center of the chamber. The region between the target and the blanket is void.

The innermost blanket region, zone 3, contains the BeO neutron multiplier. This zone is 0.1 m thick and has an inner radius of 3.4 m. The density of BeO within zone 3 is varied to represent variations in the effective multiplier thickness, x_3.

The $LiAlO_2$ breeding blanket, zone 4, extends from a radius of 3.5 to 4.5 m. Again the material density is varied to represent variations in the breeding blanket thickness, x_2. The ^6Li fraction of lithium in this zone is the third design variable, x_1.

Outside the breeding blanket is a 2-cm-thick shell, zone 5, of SiC representing the chamber wall. This is followed by a 2-cm-thick region, zone 6, that contains the Al/SiC fiber composite and represents the tendons. The two beam ports are represented by cylindrical voids in the blanket. The radius of these holes is 0.72 m so that the solid angle fraction subtended at a radius of 4.5 m is 1.25%.

The geometric characteristics are listed in Table 5.1. The volume of zone 6 is 5.09 x 10^6 cm^3. Thus from Eq. 5.4, the heat rate in

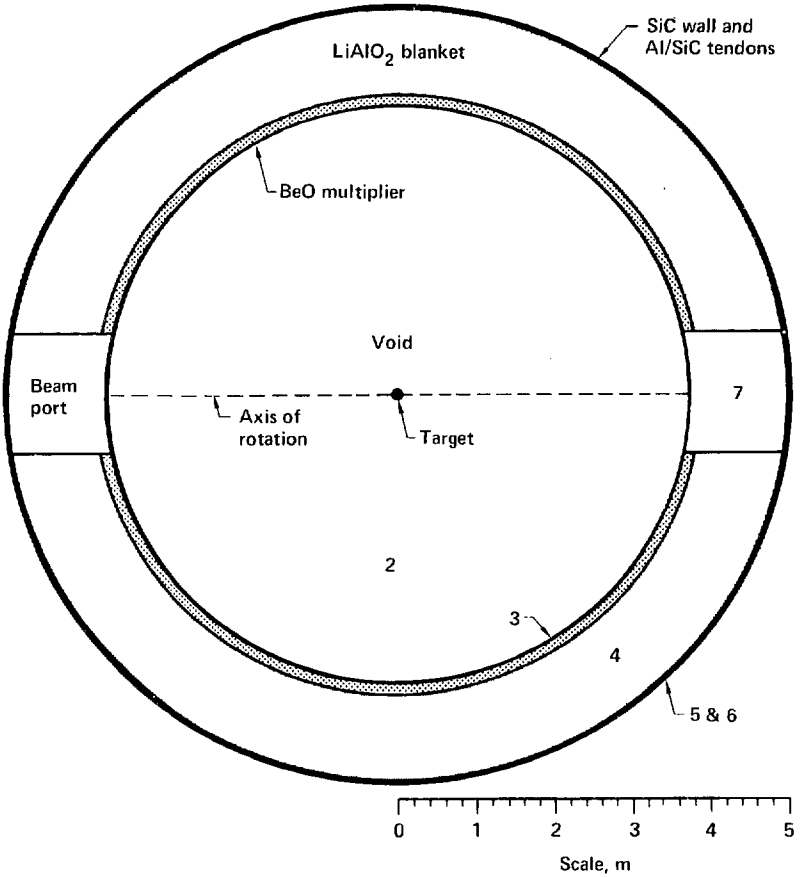

Fig. 5.2 Neutronics model of the Cascade chamber.

Table 5.1

Geometric characteristics of the Cascade neutronics model.

Zone	Description	Inner Radius (cm)	Outer Radius (cm)	Material
1	Target	0	0.03	1
2	Vacuum	0	340	Void
3	Neutron multiplier	340	350	2
4	Breeding blanket	350	450	3
5	Chamber wall	450	452	4
6	Tendons	452	454	5

the Aℓ/SiC tendons for 3000 MW of fusion power is

$$G = 33.5\ E_t, \tag{5.6}$$

where

E_t = energy deposited in zone 6, MeV per DT reaction.

The composition of the materials used in the neutronics calculations are listed in Table 5.2. The tendons are 65 vol% Aℓ and 35 vol% SiC fibers. These fibers contain CO and SiO_2 impurities which gives rise to the indicated oxygen content. The fiber composition is 57 wt% Si, 31 wt% C, and 12 wt% O.

5.2.2 Results of the eight initial transport calculations.

As previously stated, eight reference point transport calculations are required for the Cascade chamber optimization problem. The eight points are defined by the combinations of two values for each of the three design variables. The reference values for the design variables are ^{6}Li fractions of 7.42 and 50%, $LiAlO_2$ blanket thicknesses of 0.30 and 0.50 m, and BeO multiplier thicknesses of 0.05 and 0.15 m.

The results are given in Tables 5.3-5.6. The reaction rates and the neutron balance for the four transport calculations with 0.05 m of BeO and 0.15 m of BeO are given in Tables 5.3 and 5.5, respectively. The neutron balance gives the net neutron gain or loss in the various regions of the chamber. The small remainder is the neutron capture in the SiC wall and Aℓ/SiC tendons.

The energy deposition per DT reaction in each zone is given in Table 5.4 for the four cases with 0.05 m of BeO, and in Table 5.6 for the four cases with 0.15 m of BeO. The key number here is the energy

Table 5.2

Composition of materials used in the Cascade neutronics calculations

Material	Density (g/cm^3)	Isotopic Fractions (%)	
1	100	D	50.00
		T	50.00
2	3.01	Be	50.00
		O	50.00
3[a]	2.55	^{6}Li	1.86
		^{7}Li	23.14
		Al	25.00
		O	50.00
3[b]	2.55	^{7}Li	12.50
		^{7}Li	12.50
		Al	25.00
		O	50.00
4	3.20	Si	50.00
		C	50.00
5	2.60	C	19.71
		O	5.72
		Si	15.49
		Al	59.08

a) natural lithium.

b) lithium enriched to 50% ^{6}Li.

Table 5.3

Reaction rates and neutron balance for transport calculations with 0.05 m of BeO

Reference point	1	2	3	4
$LiAlO_2$ thickness, m	0.30	0.30	0.50	0.50
^6Li Fraction, %	7.42	50.00	7.42	50.00
Reactions[a]				
$^6Li(n,T)\alpha$	0.797 (1.2)[b]	0.948 (1.3)	0.999 (1.7)	1.100 (1.1)
$^7Li(n,n'T)\alpha$	0.070 (0.9)	0.038 (1.0)	0.075 (1.5)	0.040 (1.9)
Be(n,2n)	0.269 (1.6)	0.266 (1.4)	0.264 (1.1)	0.267 (0.9)
Neutron balance[a]				
Target	1.057	1.056	1.055	1.057
BeO	0.189	0.188	0.187	0.184
$LiAlO_2$	-0.893	-1.046	-1.104	-1.179
Port leakage	-0.046 (4.1)	-0.033 (3.5)	-0.043 (3.2)	-0.030 (8.6)
Blanket leakage	-0.303 (2.0)	-0.161 (2.5)	-0.094 (2.7)	-0.031 (3.1)
Remainder	0.004	0.004	0.001	0.001

a) per DT reaction.

b) percent standard deviation.

Table 5.4

Energy deposition for the transport calculations with 0.05 m of BeO

Reference point	1	2	3	4
$LiAlO_2$ thickness, m	0.30	0.30	0.50	0.50
^6Li Fraction, %	7.42	50.00	7.42	50.00
Energy deposited[a]				
Target	1.80 (0.4)[b]	1.85 (1.0)	1.85 (0.7)	1.83 (0.8)
BeO	3.05 (0.9)	3.02 (0.4)	3.06 (1.0)	3.03 (0.4)
$LiAlO_2$	9.19 (0.7)	9.98 (0.7)	10.77 (1.1)	11.28 (0.8)
SiC wall	0.11 (2.9)	0.11 (2.9)	0.03 (10.2)	0.02 (7.5)
Tendons	0.059 (3.1)	0.059 (2.8)	0.013 (8.2)	0.014 (6.3)
Port leakage	0.20 (5.9)	0.20 (7.5)	0.19 (7.7)	0.18 (8.8)
Blanket leakage	0.66 (3.7)	0.65 (2.7)	0.14 (7.4)	0.13 (7.6)

a) MeV per DT reaction.

b) percent standard deviation.

Table 5.5

Reaction rates and neutron balance for transport calculations with 0.15 m of BeO

Reference point	5	6	7	8
$LiAlO_2$ thickness, m	0.30	0.30	0.50	0.50
^6Li Fraction, %	7.42	50.00	7.42	50.00
Reactions[a]				
$^6Li(n,T)\alpha$	1.158 (0.5)	1.217 (0.9)	1.263 (0.8)	1.276 (1.2)
$^7Li(n,n'T)\alpha$	0.023 (2.6)	0.012 (2.7)	0.023 (3.2)	0.012 (3.0)
Be(n,2n)	0.562 (1.1)	0.569 (1.4)	0.561 (1.1)	0.556 (1.3)
Neutron balance[a]				
Target	1.052	1.051	1.061	1.057
BeO	0.321	0.318	0.325	0.315
$LiAlO_2$	-1.179	-1.252	-1.290	-1.305
Port leakage	-0.057 (3.8)	-0.051 (4.6)	-0.056 (4.2)	-0.050 (6.4)
Blanket leakage	-0.136 (1.9)	-0.065 (3.3)	-0.039 (5.3)	-0.016 (12.9)
Remainder	0.001	0.001	0.001	0.001

a) per DT reaction.

b) percent standard deviation.

Table 5.6

Energy deposition for the transport calculations with 0.15 m of BeO

Reference point	5	6	7	8
$LiAlO_2$ thickness, m	0.30	0.30	0.50	0.50
^6Li Fraction, %	7.42	50.00	7.42	50.00
Energy deposited[a]				
Target	1.81 (0.6)[b]	1.83 (0.7)	1.84 (0.8)	1.83 (0.5)
BeO	6.89 (0.6)	6.82 (0.9)	6.94 (0.5)	6.82 (0.9)
$LiAlO_2$	7.77 (0.9)	7.91 (0.7)	8.36 (1.0)	8.38 (1.2)
SiC wall	0.05 (6.2)	0.04 (4.5)	0.01 (7.8)	0.01 (8.0)
Tendons	0.026 (5.4)	0.024 (3.8)	0.007 (7.1)	0.006 (16.5)
Port leakage	0.21 (8.0)	0.20 (6.5)	0.18 (6.3)	0.19 (9.1)
Blanket leakage	0.28 (4.8)	0.26 (4.3)	0.06 (8.2)	0.06 (14.6)

a) MeV per DT reaction.

b) percent standard deviation.

deposition in the Al/SiC tendons. The other information is provided for completeness.

The results of the eight reference point transport calculations form the basis for estimating the neutronic performance as a function of the three design variables. This is discussed in the next section.

5.3 INITIAL OPTIMIZATION RESULTS FOR CASCADE

5.3.1 Estimated Neutronic Performance.

The neutronic performance is estimated as a function of the three design variables by successive, two point variation interpolation. In particular, the constraints on the tritium breeding ratio, the tendon heat generation rate, and the total neutron leakage must be determined.

The tritium breeding ratio as a function of the ^6Li fraction and the $LiAlO_2$ blanket thickness for the case of a 0.05-m-thick BeO multiplier is shown in Fig. 5.3. Note from Table 5.3 that the tritium breeding is dominated by the contribution from ^6Li. A contour plot of the tritium breeding ratio with 0.5 m of BeO is shown in Fig. 5.4. To meet the constraint of $T \geq 1.05$ requires a $LiAlO_2$ blanket thickness greater than ~0.37 m if the Li is enriched to ~40% ^6Li.

Figures 5.5 and 5.6 show the tritium breeding ratio in the $LiAlO_2$ blanket when a 015-m-thick BeO multiplier is used. Here the benefit multiplier is clear. The tritium breeding ratio exceeds the minimum required value of 1.05 over the entire range of ^6Li fractions and $LiAlO_2$ blanket thickness shown. The only exception is for thin blankets with denatured Li, i.e., less than ~3% ^6Li.

As seen in the previous four figures, the tritium breeding ratio shows the same trends as discussed for the modified HYLIFE chamber. In particular, the breeding ratio increases with increasing ^6Li fraction and with increasing blanket thickness. The breeding ratios were calculated by interpolating on x_1 first, then on x_2 and finally on x_3.

As indicated in Tables 5.4 and 5.6 the energy deposition in the

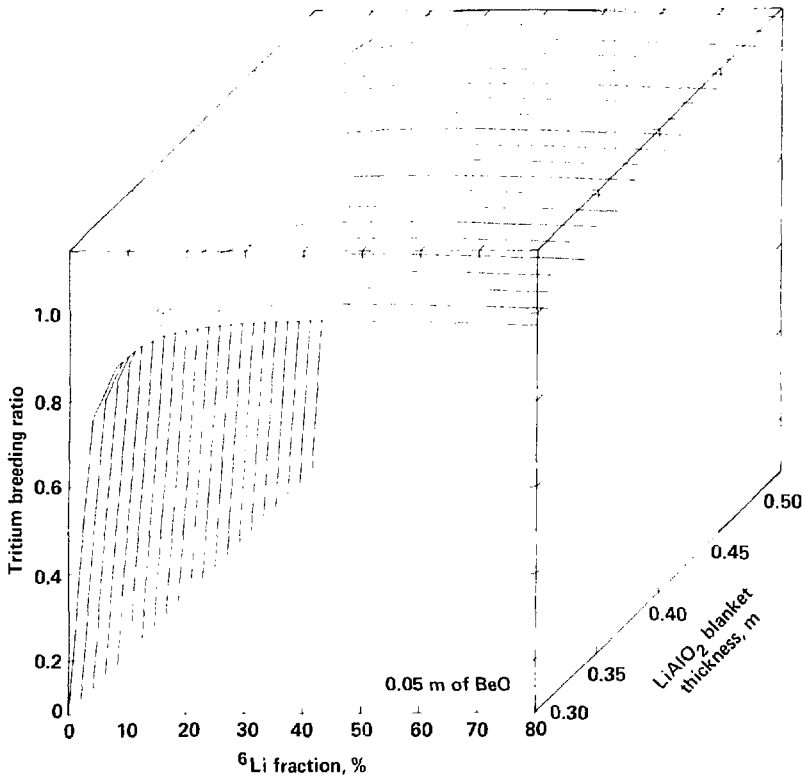

Fig. 5.3 Tritium breeding ratio as a function of ^{6}Li fraction and $LiAlO_2$ thickness with 0.05 m of BeO.

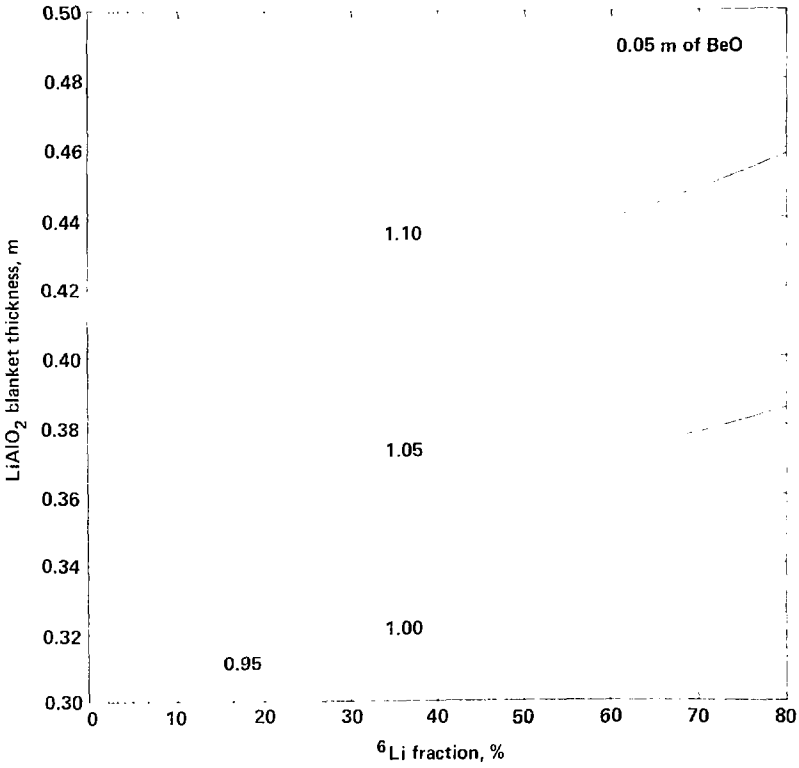

Fig. 5.4 Contour plot of tritium breeding ratio with 0.05 m of BeO. The tritium breeding ratio must be greater than 1.05.

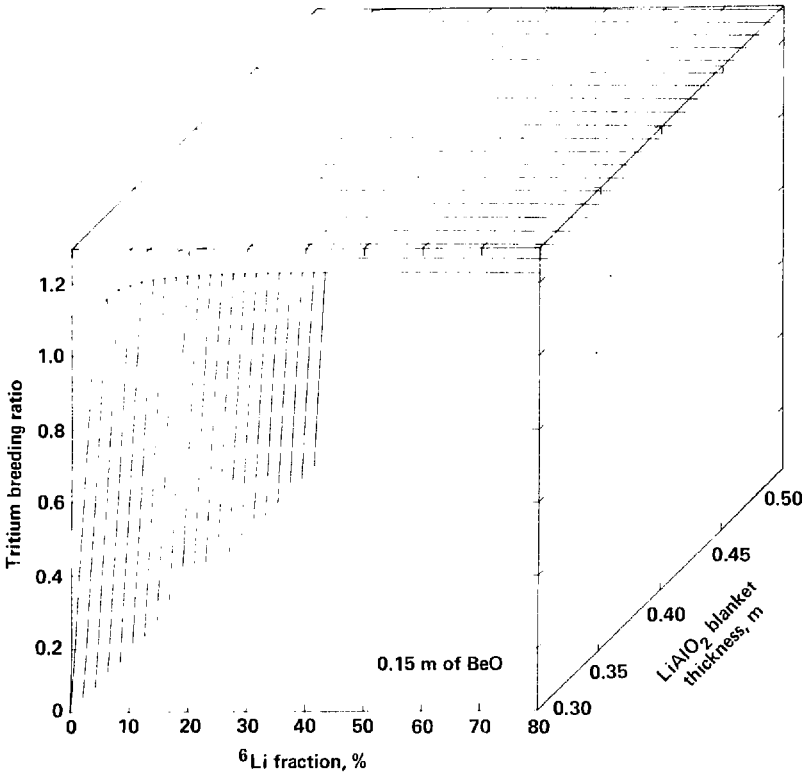

Fig. 5.5 Tritium breeding ratio as a function of ^{6}Li fraction and $LiAlO_2$ thickness with 0.15 m of BeO.

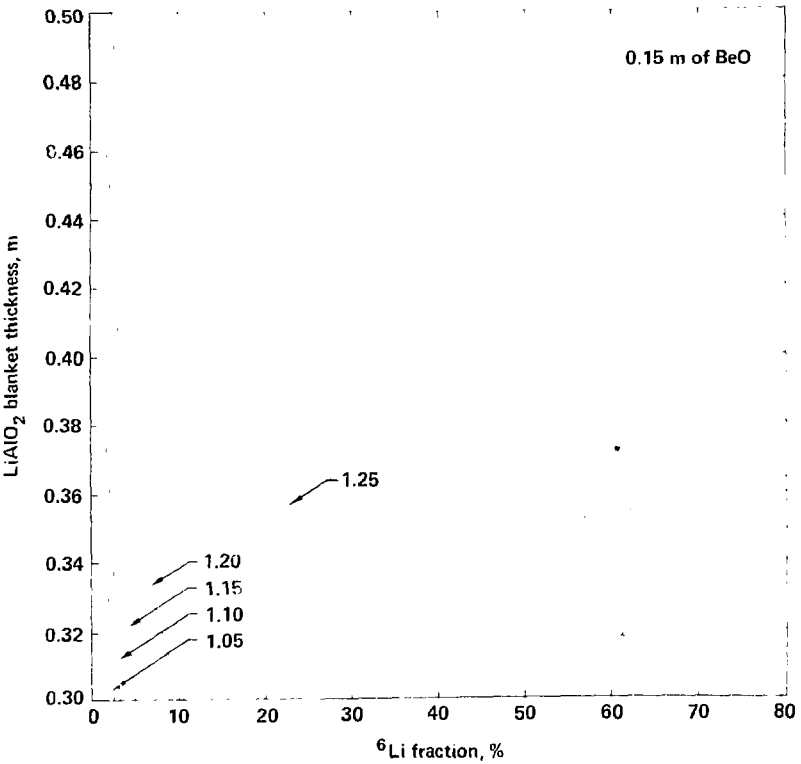

Fig. 5.6 Contour plot of tritium breeding ratio with 0.15 m of BeO. The tritium breeding ratio must be greater than 1.05.

Al/SiC tendons is independent of the ^6Li fraction. Figure 5.7 shows the heat generation rate (W/cm^3) in the tendons as a function of the BeO thickness and the $LiAlO_2$ blanket thickness. As indicated, the heat generation rate decreases as the thickness of either region increases.

A contour plot of the tendon heat rate is shown in Fig. 5.8. Recall the heat rate must be ≤ 0.85 W/cm^3. In order to meet this constraint, the minimum required $LiAlO_2$ thickness is ~0.38 m with 0.05 m of BeO. The required thickness decreases with increasing BeO thickness to ~0.30 m with 0.15 m of BeO. The heat generation rate is calculated by first interpolating on x_2 and then on x_3.

The neutron leakage is calculated from a neutron balance with the net gain in the BeO region and the net absorption in the $LiAlO_2$ blanket being estimated by successive two point interpolation. That is

$$L = 1.056 + N_g - N_a, \tag{5.7}$$

where

N_g = net neutron gain in BeO, and

N_a = net neutron absorption in $LiAlO_2$.

The factor of 1.056 is the number of neutrons emitted by the target per DT reaction. It exceeds one because of (n,2n) reactions with D and T in the compressed fuel zone.

The total neutron leakage as a function of the ^6Li fraction and $LiAlO_2$ blanket thickness is shown in Figs. 5.9 and 5.10 for the case of a 0.05-m-thick BeO multiplier. The leakage decreases with

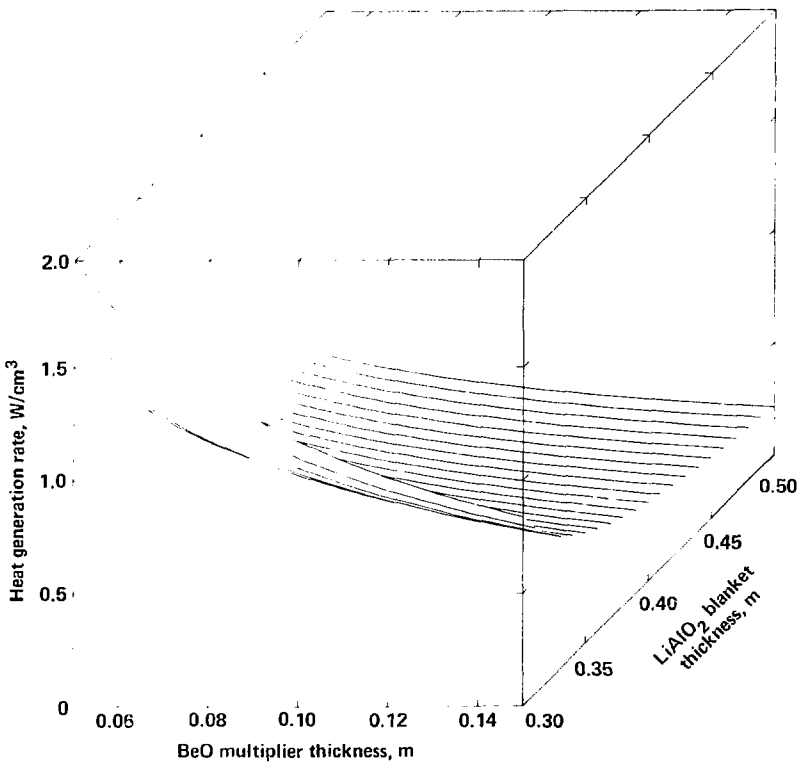

Fig. 5.7 Heat generation rate in Aℓ/SiC tendons as a function of BeO thickness and $LiAlO_2$ thickness. The fusion power is 3000 MW.

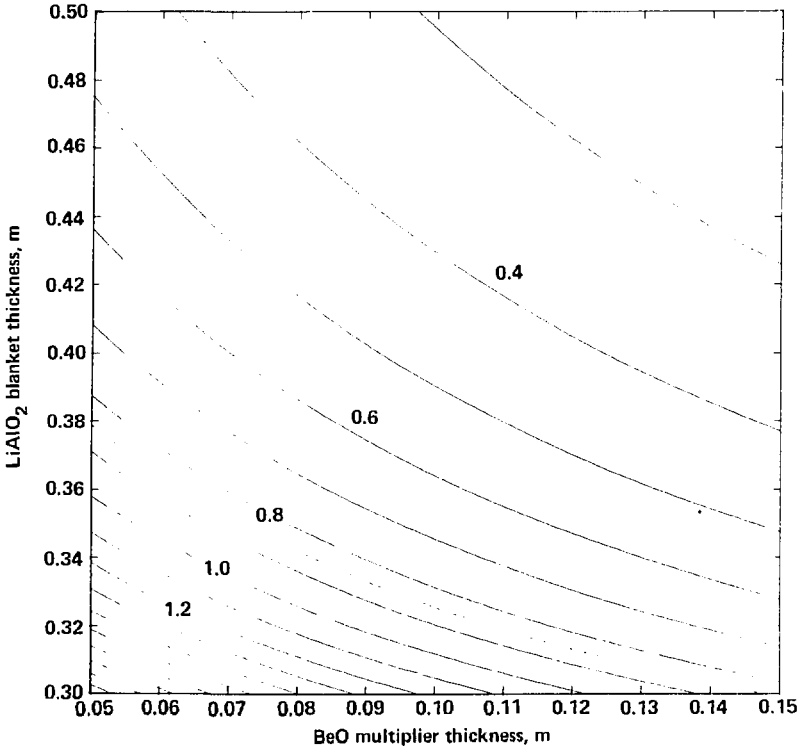

Fig. 5.8 Contour plot of the heat generation rate in the tendons. The heat rate must be less than 0.85 W/cm^3.

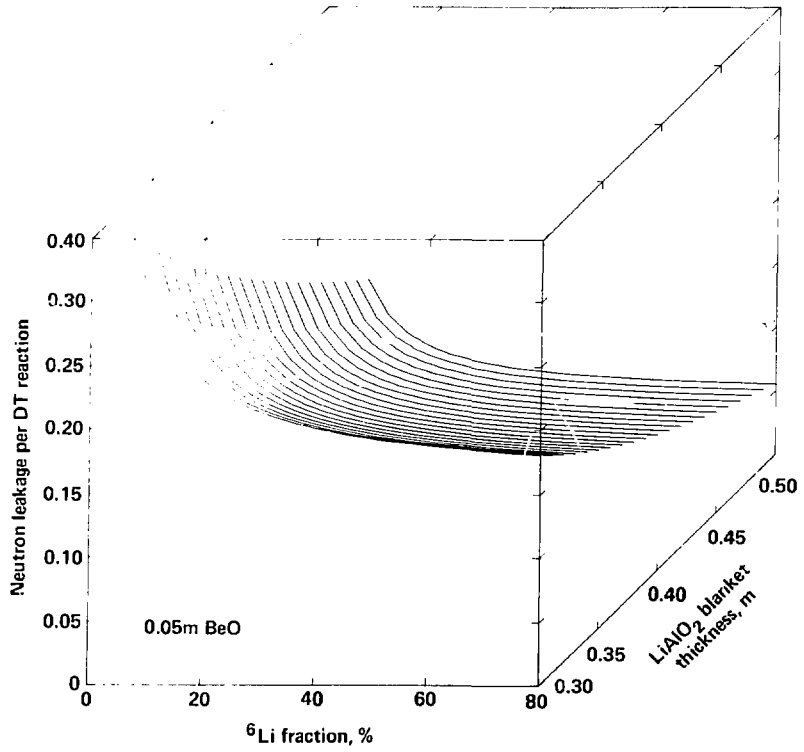

Fig. 5.9 Total neutron leakage per DT reaction as a function of ^{6}Li fraction and $LiAlO_2$ thickness with 0.05 m of BeO.

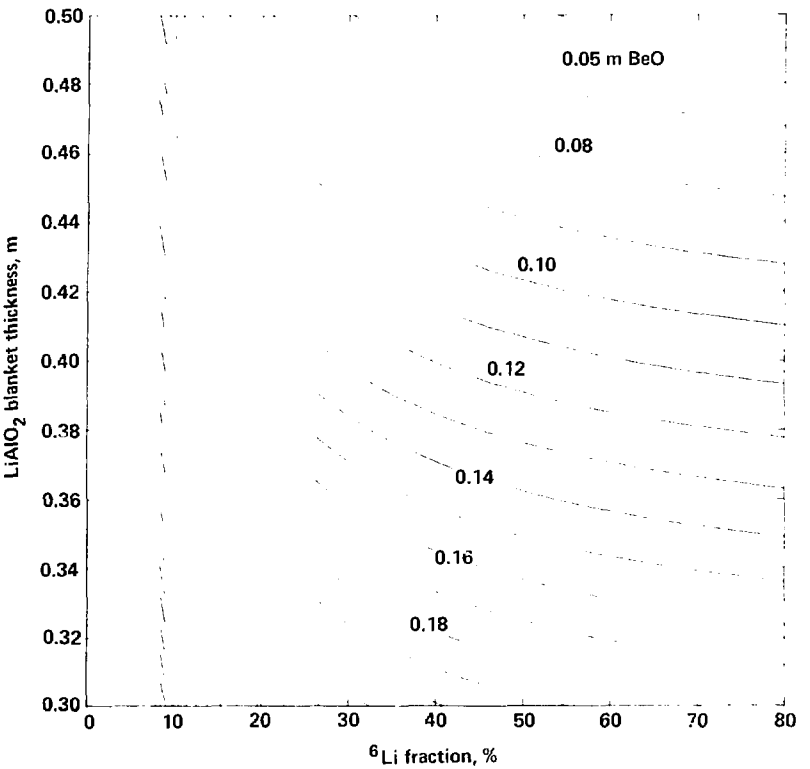

Fig. 5.10 Contour plot of neutron leakage with 0.05 m of BeO. The total neutron leakage is limited to 0.10.

increasing ^6Li fraction and with increasing blanket thickness since in both cases more neutrons are captured by ^6Li as these variables increase. The curves extend down to 7.42% ^6Li, i.e., natural lithium. Note from Fig. 5.10, that even if the Li is enriched to 80% in ^6Li, a 0.41-m-thick blanket is required to keep the neutron leakage below 0.1 per DT reaction.

Figures 5.11 and 5.12 show the neutron leakage as a function of the ^6Li fraction and the $LiAlO_2$ blanket thickness when a 0.15-m-thick BeO multiplier is used. Note that the range of the vertical scale of Fig. 5.11 is about a factor of two smaller than in Fig. 5.9. In this case, the minimum required breeding blanket thickness decreases from ~0.49 m with natural Li to ~0.33 m with Li enriched to 80% ^6Li.

The three constraints, Eqs. 5.2, 5.3 and 5.5 are shown as a function of the ^6Li fraction and the $LiAlO_2$ blanket thickness for 0.05, 0.10, and 0.15 m of BeO in Figs. 5.13, 5.14 and 5.15, respectively. In each case it is desirable to find the minimum value of the $LiAlO_2$ thickness such that the figure of merit, $x_2 + x_3$, is minimized.

Comparing these three figures gives an indication of how the constraints vary as a function of the BeO thickness. The minimum $LiAlO_2$ blanket thickness set by the tritium breeding ratio constraint decreases with increasing BeO thickness. The same trend applies to the heat generation rate constraint.

Note that for the neutron leakage constraint, the minimum $LiAlO_2$ blanket thickness is greater at 0.10 m of BeO than at 0.05 or 0.15 m. This rise and fall in the required blanket thickness is

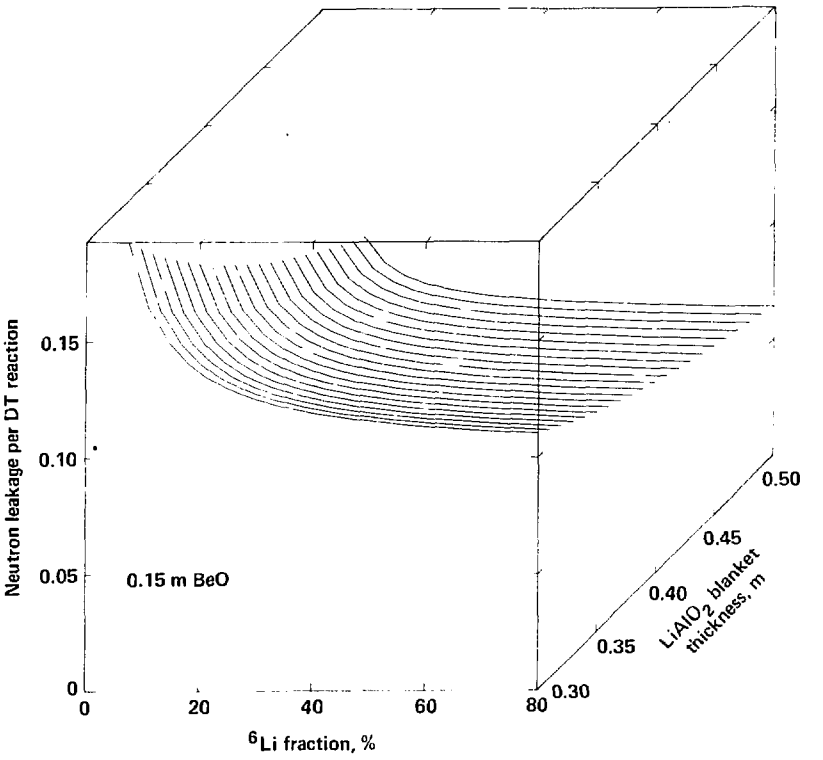

Fig. 5.11 Total neutron leakage per DT reaction as a function of ^{6}Li fraction and $LiAlO_2$ thickness with 0.15 m of BeO.

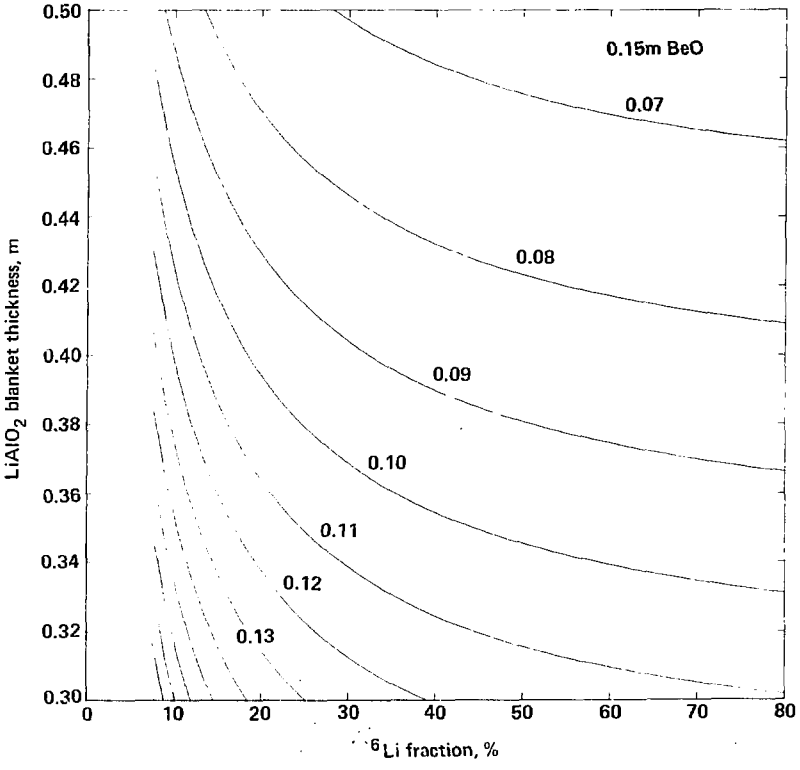

Fig. 5.12 Contour plot of neutron leakage with 0.15 m of BeO. The total neutron leakage is limited to 0.10.

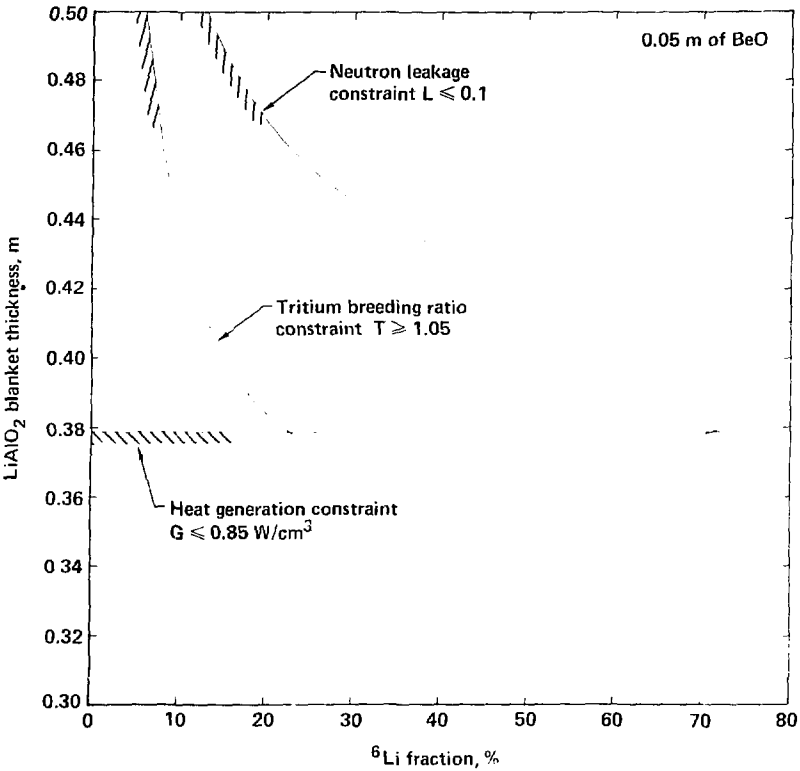

Fig. 5.13 Three constraints as a function of ^{6}Li fraction and $LiAlO_2$ thickness with 0.05 m of BeO.

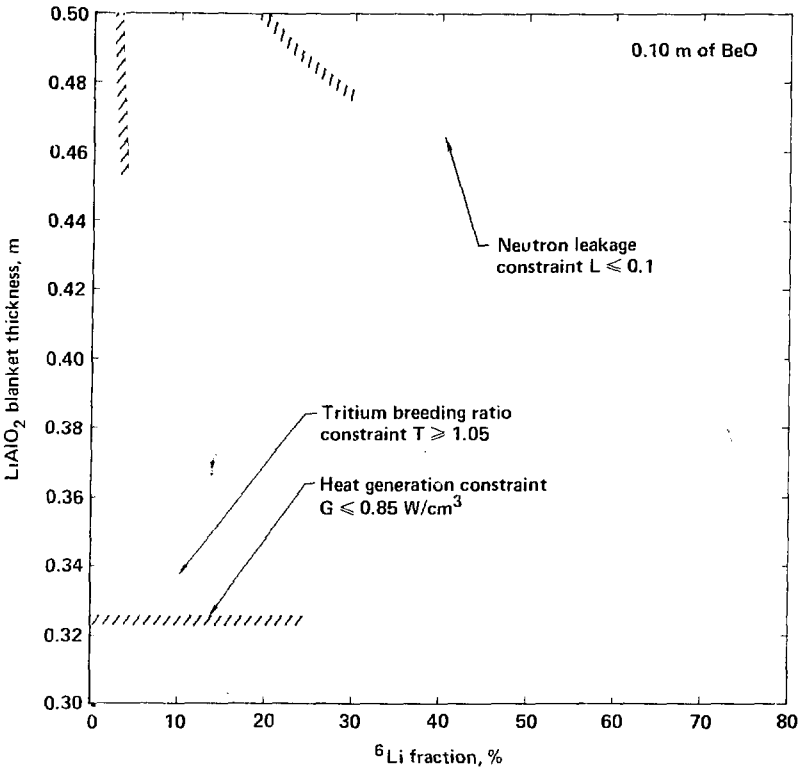

Fig. 5.14 Three constraints as a function of ^{6}Li fraction and $LiAlO_2$ thickness with 0.10 m of BeO.

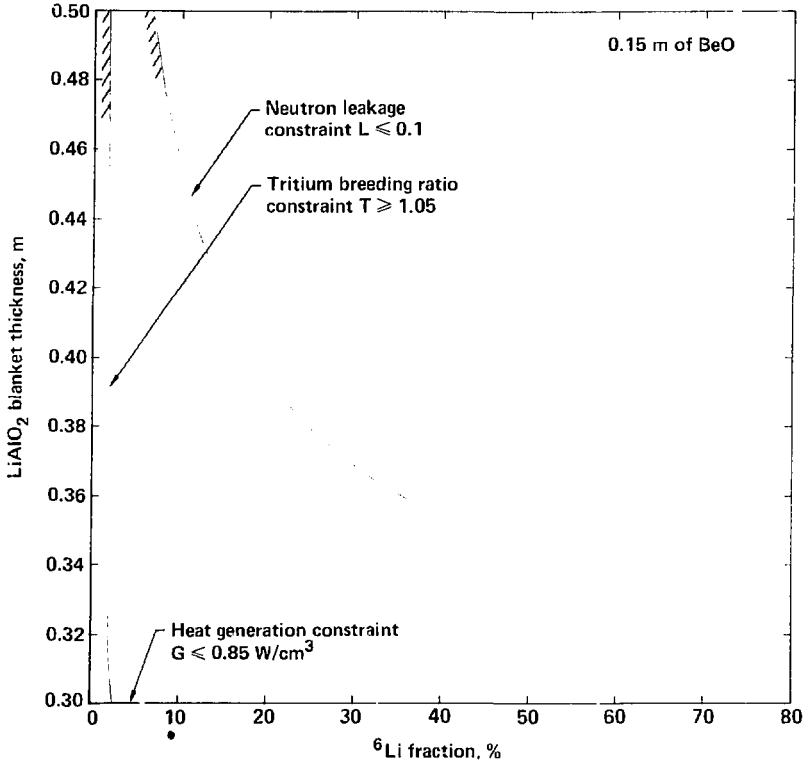

Fig. 5.15 Three constraints as a function of ^{6}Li fraction and $LiAlO_2$ thickness with 0.15 m of BeO.

related to the two modes of neutron leakage. As indicated in Tables 5.3 and 5.5, increasing the BeO thickness increases the neutron leakage through the ports and decreases the blanket leakage. For a blanket highly enriched in ^6Li, the increase in port leakage can exceed the decrease in blanket leakage. As a result a thicker breeding blanket is required to maintain a constant total leakage rate of 0.1 per DT reaction.

In all three figures the limiting constraint is the neutron leakage constraint. Assuming a upper limit of 80% on the ^6Li enrichment, the minimum $LiAlO_2$ blanket thicknesses are 0.41, 0.44, and 0.33 m for the 0.05, 0.10, and 0.15 m thick BeO cases, respectively.

5.3.2 Optimal Design Point.

The direct search algorithm gives the optimal design point as 63.6% ^6Li, 0.397 m of $LiAlO_2$ and 0.040 m of BeO. This result is shown graphically in Figs. 5.16 and 5.17. Figure 5.16 shows the minimum blanket thickness as set by the neutron leakage constraint and the heat generation constraint as a function of the BeO thickness. For less than 0.04 m of BeO the heat generation rate is the limiting constraints. Between 0.04 and 0.16 m of BeO, neutron leakage is the limiting constraint. Beyond 0.16 m, the $LiAlO_2$ blanket thickness is again limited by the heat generation rate.

Also shown in Fig. 5.16 is the figure of merit, i.e., the total blanket thickness. Note that there are two local minima, one at 0.04 m of BeO and the other at 0.16 m. The minima at 0.04 m however, is the lower of the two.

The constraints as a function of the ^6Li fraction and the

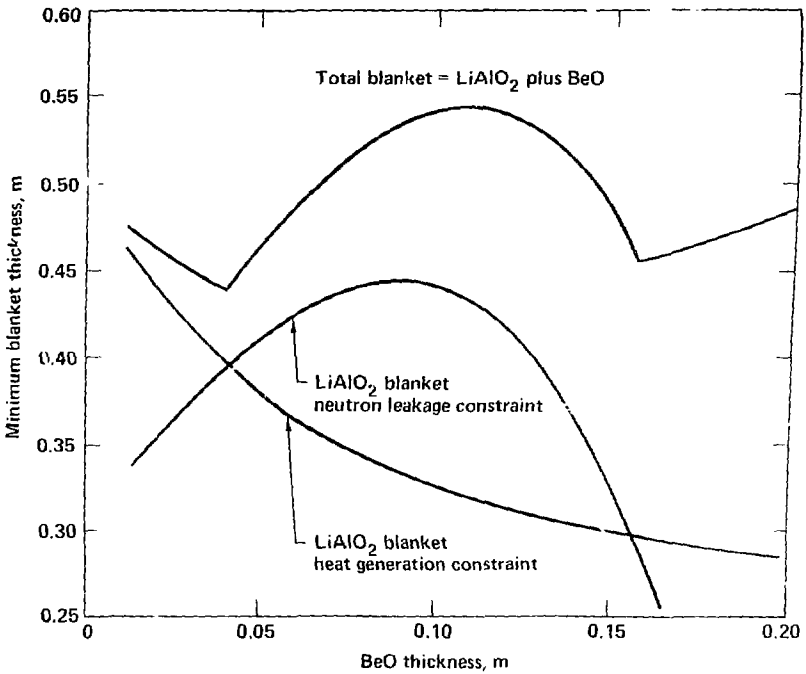

Fig. 5.16 Minimum blanket thickness as a function of BeO thickness. The lower curves show the minimum $LiAlO_2$ thickness as set by the neutron leakage and heat rate constraints. The top curve is the total blanket thickness including the BeO thickness.

$LiAlO_2$ thickness are shown in Fig. 5.17 for the optimal 0.04 m of BeO. Note again how the optimal design point lies at the intersection of the neutron leakage and heat generation rate constraints. Clearly higher ^6Li enrichments give the same minimum thickness since the heat rate is independent of this variable. The minimum acceptable ^6Li fraction, 63.6%, is chosen from a resource consideration.

5.3.3 Comparison to transport calculation at the optimal point.

An additional neutron transport calculation was carried out at 63.6% ^6Li, 0.40 m of $LiAlO_2$ and 0.04 m of BeO. The results are compared to the estimated results at the optimal point in Table 5.7. The estimated tritium breeding ratio is ~3% higher than the TART result and the estimated neutron leakage is low by ~6%. While these are acceptable differences, heat generation rate in the Al/SiC tendons is actually 22% higher than the estimated result.

In the next section an improved estimate of the location of the optimal design point is made based on a new estimate o the tendon heat generation rate as a function of the $LiAlO_2$ and BeO thickness.

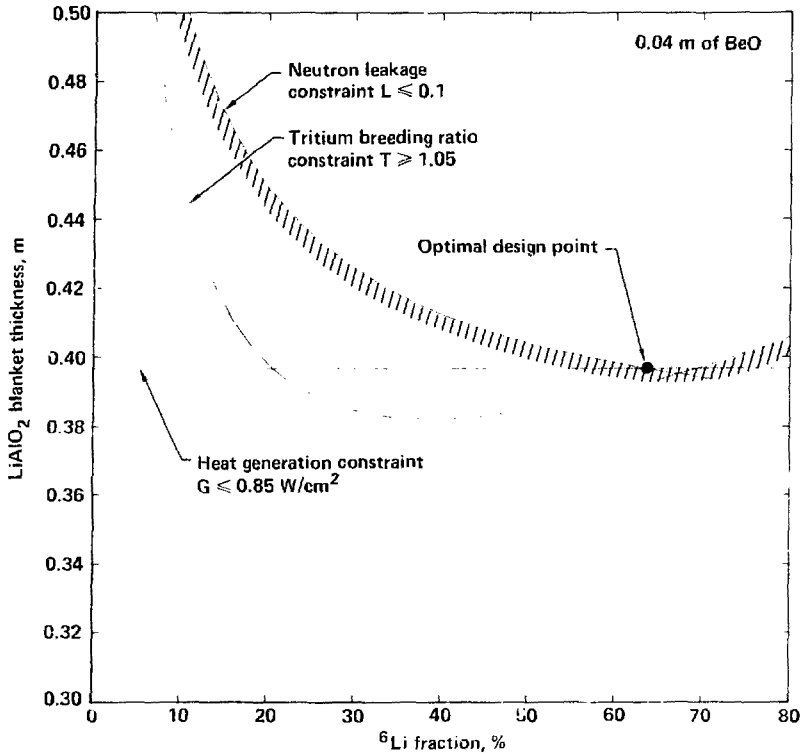

Fig. 5.17 First estimate of the location of the optimal design point. The point lies at the intersection of the neutron leakage and heat generation rate constraints.

Table 5.7

Comparison of neutronic performance at x_1 = 63.6%, x_2 = 0.40 m, and x_3 = 0.04 m

Parameter[a]	TART	Estimated
$^{6}Li(n,T)\alpha$	0.985 (1.3)[b]	1.021
$^{7}Li(n,n'T)\alpha$	0.032 (2.0)	0.032
Tritium breeding ratio	1.017	1.053
Total neutron leakage	0.106 (3.0)	0.100
Energy deposited in tendons, MeV	0.031 (4.0)	0.025

a) per DT reaction.

b) percent standard deviation.

5.4 IMPROVED ESTIMATE OF LOCATION OF OPTIMUM

As indicated in the previous section, there is a significant difference between the estimated heat generation rate in the Al/SiC tendons and the results of the neutron transport calculation. It is postulated that this difference is largely due to the fact that a significant fraction of the energy deposited in the Al/SiC tendons is photon energy that originates in the $LiAlO_2$ blanket. The break down is given in Tables 5.8 and 5.9. The variational interpolation formula used to predict the energy deposition in the tendons only accounts for variations in the neutron flux in that region. It does not account for variations in the photon source in adjacents region and the transport of those photons into the tendons.

An alternate approach is therefore used to estimate the heat rate in the tendons as a function of the BeO and $LiAlO_2$ blanket thicknesses. It is assumed that the heat generation rate decreases exponentially with the thickness of BeO and with the thickness of $LiAlO_2$. That is

$$E = E_0 \exp(-\mu_2 x_2) \exp(-\mu_3 x_3) \qquad (5.8)$$

where

E = energy deposition in the Al/SiC tendons, MeV,

E_0 = energy deposition with no blanket, MeV,

μ_2 = attenuation coefficient for $LiAlO_2$ thickness, m^{-1}, and

μ_3 = attenuation coefficient for BeO thickness, m^{-1}.

Using the energy deposition results given in Tables 5.4 and 5.6

Table 5.8

Photon energy source and deposition in Al/SiC tendons with 0.05 m of BeO.

Reference point	1	2	3	4
$LiAlO_2$ thickness, m	0.30	0.30	0.50	0.50
^6Li Fraction, %	7.42	50.00	7.42	50.00
Photon source[a]	0.028	0.039	0.006	0.006
Photon deposition[a]	0.043	0.043	0.010	0.012
Photon/Total[b]	0.73	0.73	0.77	0.86

a) MeV per DT reaction.

b) Ratio of photon energy deposition to total energy deposition. Total deposition given in Table 5.4.

Table 5.9

Photon energy source and deposition in Al/SiC tendons with 0.15 m of BeO.

Reference point	5	6	7	8
$LiAlO_2$ thickness, m	0.30	0.30	0.50	0.50
^6Li Fraction, %	7.42	50.00	7.42	50.00
Photon source[a]	0.013	0.007	0.006	0.003
Photon deposition[a]	0.021	0.019	0.006	0.005
Photon/Total[b]	0.81	0.79	0.86	0.83

a) MeV per DT reaction.

b) Ratio of photon energy deposition to total energy deposition. Total deposition given in Table 5.6.

the following system of equations can be written,

$$0.059 = E_0 \exp(-0.3\mu_2) \exp(-0.05\mu_3), \quad (5.9)$$

$$0.014 = E_0 \exp(-0.5\mu_2) \exp(-0.05\mu_3), \quad (5.10)$$

$$0.025 = E_0 \exp(-0.3\mu_2) \exp(-0.15\mu_3). \quad (5.11)$$

Solving for the three unknowns and substituting into Eq. 5.8 gives

$$E = 0.827 \exp(-7.37x_2) \exp(-8.59x_3). \quad (5.12)$$

Using this expression, the predicted energy deposition for the optimal design point of $x_2 = 0.40$ m and $x_3 = 0.04$ m is 0.031 MeV or 1.03 W/cm^3. Hence at this particular point the new estimate is quite accurate.

The heat generation rate in the tendon as a function of the BeO multiplier thickness and $LiAlO_2$ thickness is shown in Figs. 5.18 and 5.19. Note that the surface in Fig. 5.18 is somewhat flatter than the earlier estimate shown in Fig. 5.7.

The optimization problem was rerun, using the exponential estimate for the heat generation rate in the tendons. The optimal design point in this case is 34.2% ^{6}Li, 0.424 m of $LiAlO_2$, and 0.042 m of BeO. The constraints and location of the optimal design point for this case are shown in Fig. 5.20

A final transport calculation was carried out at the new optimal point. The results are compared to the estimated results in Table 5.10. In this case the agreement is close for all the relevant parameters.

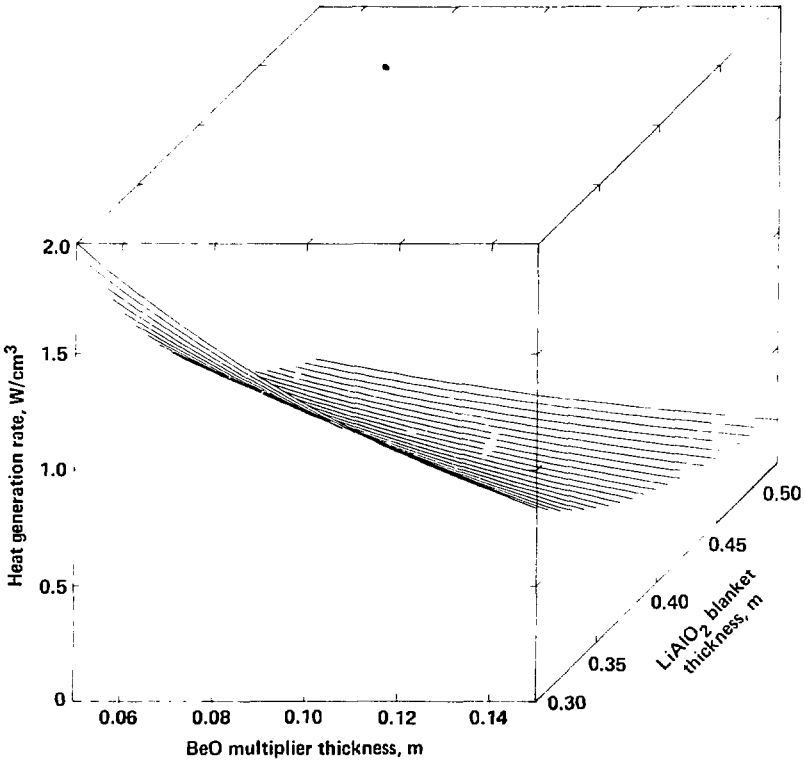

Fig. 5.18 New estimate of heat generation rate in Al/SiC tendons as a function of BeO thickness and $LiAlO_2$ thickness.

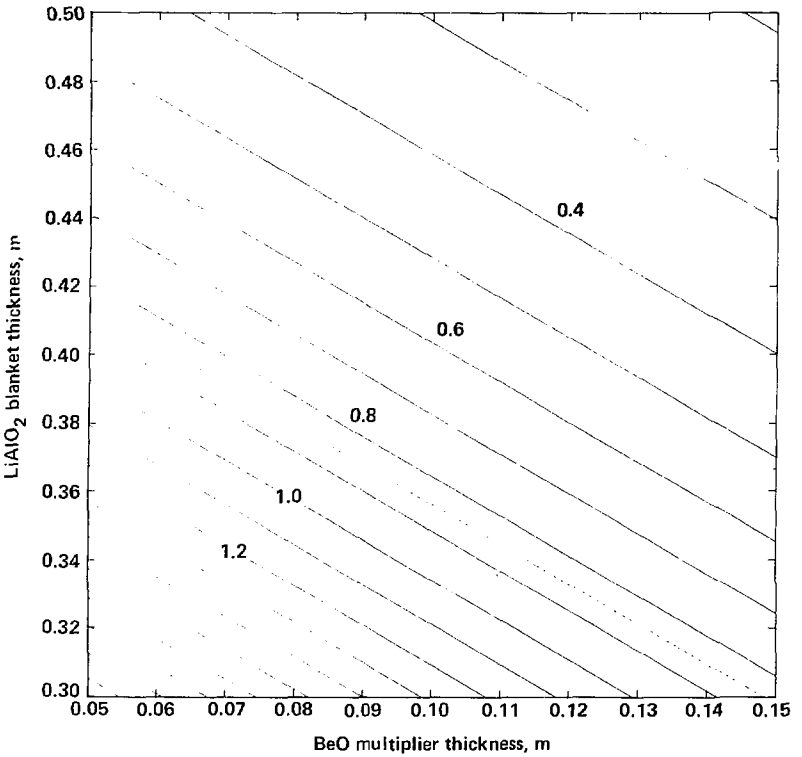

Fig. 5.19 Contour plot of new heat generation rate.

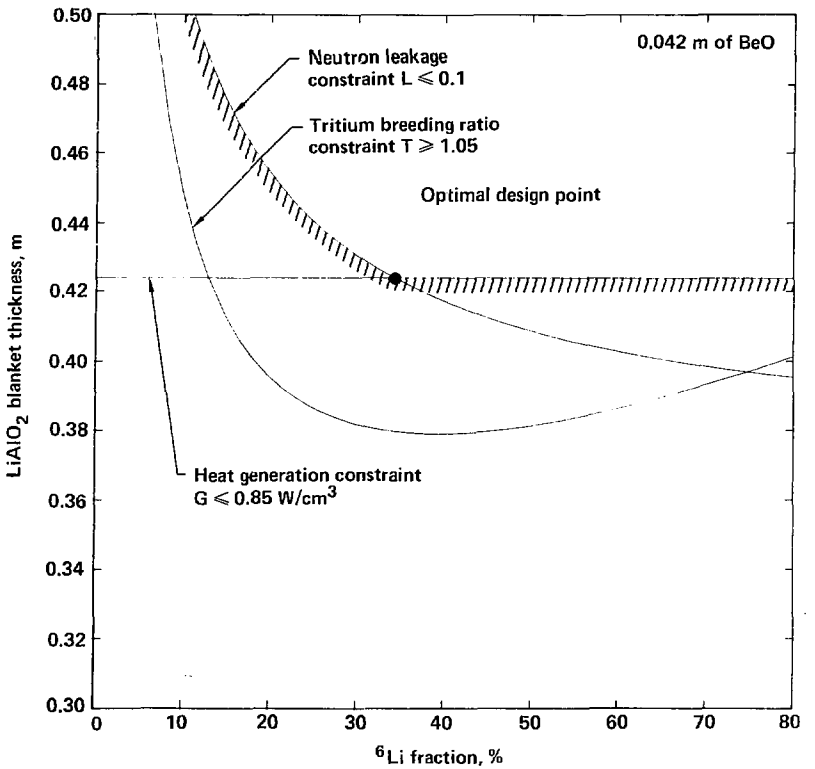

Fig. 5.20 Final estimate of location of optimal design point.

Table 5.10

Comparison of neutronic performance at x_1 = 34.2%, x_2 = 0.424 m, and x_3 = 0.042 m.

Parameter[a]	TART	Estimated
$^{6}Li(n,T)\alpha$	1.019 (1.0)[b]	1.029
$^{7}Li(n,n'T)\alpha$	0.040 (1.1)	0.057
Tritium breeding ratio	1.059	1.086
Total neutron leakage	0.097 (3.7)	0.100
Energy deposited in tendons, MeV	0.024 (3.0)	0.025

a) per DT reaction.

b) percent standard deviation.

5.5 SUMMARY

In summary, the Cascade chamber can be designed with a $LiAlO_2$ breeding blanket if a BeO neutron multiplier is used. The configuration that minimized the total blanket thickness is 0.042 m of BeO followed by 0.424 m of $LiAlO_2$. The Li must be enriched to at least 34.2% in ^6Li.

Since the blanket is a pebble bed, the actual thickness is the effective thickness divided by the pebble packing fraction. Assuming a 50% packing fraction gives an actual total blanket thickness of 0.93 m.

6. CONCLUSIONS AND RECOMMENDATIONS FOR FUTURE WORK

6.1 SUMMARY AND CONCLUSIONS

Optimal blanket design is a key element in effective fusion reactor design. A methology has been developed to systematically optimize the blanket design as a function of several variables. The optimization problem consists of four essential elements: the figure of merit for the particular reactor concept, a technique for estimating the neutronic performance as a function of the selected design variables, constraints on both the design variables and the neutronic performance, and a method for optimizing the figure of merit subject to the constraints.

In the method presented, the neutronic performance is estimated using variational interpolation. By successive interpolations, the neutronic performance can be estimated as a function of several design variables based on a limited number of reference point, neutron transport calculations. Since only forward flux solutions are required for the interpolation, any number of neutronic characteristics can be estimated based on the same reference point transport calculations. The applicability of this approach has been demonstrated in the optimization of two inertial confinement fusion reactor concepts, one as a function of two variables and the second as a function of three variables.

The variational interpolation approach should not be used indiscriminately. If the reference point results vary linearly with one or more of the design variables, it is senseless to use a

nonlinear interpolation. Also, with the three point interpolation, care must be taken to check for singularities within the range of interest. Where possible, it is advisable to relate the variational results to known boundary or continuity conditions. The neutron balance method is an example of this approach.

The optimization algorithm employed in this work is a direct search, nonlinear simplex method. The method seeks to minimize a figure of merit by comparing its value at several points and selecting a new point based on the results of the comparison. The method was found to work quite efficiently. Even with convergence parameters $\varepsilon = \delta = 10^{-6}$, the optimum was generally found with less than 200 iterations. (To prevent the possiblity of an endless search, the maximum number of iterations is specified in the input file.) Hundreds of iterations were typically completed in less than a second of CRAY-1 CPU time. In a typical problem, each iteration involved calculating several neutronic characteristics using successive variational interpolation, and then calculating a figure of merit that depends on the neutronic results.

It was found that graphical display of the constraints and figure of merit was very useful in understanding the factors determining to the location of the minimum. In addition, a visual display can reveal a nonunique minimum as in Fig. 5.20.

The optimization methodology was applied to two different ICF reactor concepts. The first optimization problem involved a modification to the HYLIFE concept. The object was to increase the fusion energy multiplication factor and thus reduce the plant capital cost per unit of net electric power. By reducing the tritium breeding

ratio and capturing more neutrons in a manganese steel, the energy multiplication factor was increased by 22% and the plant cost per kWe reduced by 12%.

The two design variables in this problem were the ^{6}Li fraction in lithium and the effective thickness of the lithium blanket. Constraints were imposed on the minimum tritium breeding ratio and a maximum displacement damage rate in the first structural wall. The optimal design point was found to be slightly less than 0.1% of ^{6}Li in an 0.91-m-thick blanket.

The second optimization problem was based on the Cascade reactor concept. A version using a $LiAlO_2$ breeding blanket with a BeO neutron multiplier was investigated. In this case the objective was to minimize the sum of the multiplier thickness and the breeding blanket thickness. Constraints were imposed on the minimum tritium breeding ratio, the maximum neutron leakage, and the maximum heat generation rate in the Al/SiC tendons that wrap the chamber.

The Cascade chamber was optimized as a function of three design variables: the BeO multiplier thickness, the ^{6}Li fraction and the $LiAlO_2$ blanket thickness. The optimal design point was found to lie at the intersection of the neutron leakage constraint and the heat generation rate constraint. The blanket parameters at this point were 0.042 m of BeO, and a 0.42-m-thick $LiAlO_2$ blanket enriched to 34.2% ^{6}Li.

6.2 RECOMMENDATIONS FOR FUTURE WORK

It is hoped that the method developed and demonstrated here will be used in future conceptual reactor design studies for both inertial and magnetic confinement fusion. The exploratory nature of such studies is an ideal format for multivariable optimization. The study of fusion-fission hybrid blankets is another area for potential future application of this method for systematic optimization.

An interesting application of the techniques developed here would be to compare the optimal blanket designs for the same reactor but with various figures of merit. For the modified HYLIFE concept the blanket was optimized to reduce the cost per unit of net electric power. In doing so, Mn is activated, and the afterheat problem is thus heightened. If minimizing induced activity had been the figure of merit, a completely different blanket design would have emerged. Alternatively, a cost penalty proportional to the chamber's afterheat could be included in defining the figure of merit. The Cascade reactor concept should also be reexamined from an economic perspective once cost scaling relations are developed.

One final recommendation for future work would be to automate and more closely couple the graphics with the definition of the figure of merit and constraints. As it now stands, the graphics are done separately.

6.3 A FINAL WORD

In an optimization problem a complex decision involving the selection of values for a number of interrelated variables, is made by focussing on a single figure of merit designed to quantify performance and measure the quality of the decision. This figure of merit is maximized or minimized subject to the constraints that may limit the selection of decision variable values. Since all the complexities of the system being analyzed can not, in general, be fully represented in the model, optimization should be regarded as a tool of conceptualization and analysis rather than a principle yielding the true optimum.[83] The result is only as good as the model. A thorough understanding of the system one is dealing with, i.e., being able to select an appropriate figure of merit, define the constraints, and model the system as accurately as possible, is, therefore, the first prerequisite to effective design optimization.

REFERENCES

1. M. J. Monsler, et al., "An Overview of Inertial Fusion Reactor Design," Nucl. Technol./Fusion, 1, p. 302 (July 1981).
2. C. C. Baker, et al., "Trends and Developments in Magnetic Fusion Reactor Concepts," Nucl. Technol./Fusion, 1, p. 5 (January 1981).
3. J. A. Maniscalco, et al., "Recent Progress in Fusion-fission Hybrid Reactor Design Studies," Nucl. Technol./Fusion, 1, p. 419 (October 1981).
4. R. W. Werner, Synfuels from Fusion - Using the Tandem Mirror Reactor and a Thermochemical Cycle to Produce Hydrogen, Lawrence Livermore National Laboratory, Livermore, CA, Rept. UCID-19609 (November 1982).
5. M. A. Pralas, J. B. Romero, E. F. Pearson, "A Critical Review of Fusion Systems for Radiolytic Conversion of Inorganics to Gaseous Fuels," Nucl. Technol./Fusion, 2, p. 143 (April 1982).
6. J. A. Maniscalco, et al., Civilian Applications of Laser Fusion, Lawrence Livermore National Laboratory, Livermore, CA, Rept. UCRL-52349 Rev. 1 (August 1978).
7. S. Glasstone and R. H. Lovberg, Controlled Thermonuclear Reactions (R. E. Krieger Publishing Co., Huntington, NY, 1960), p. 13.
8. M. M. El-Wakil, Nuclear Energy Conversion (Intext Educational Publishers, Scranton, PA, 1971) p. 548.

9. E. F. Plechaty, et al., Tabular and Graphical Presentation of 175 Neutron-Group Constants Derived from the LLL Evaluated-Nuclear-Data Library (ENDL), Lawrence Livermore National Laboratory, Livermore, CA, Rept. UCRL-50400, Vol. 16, Rev. 2 (1978).

10. J. D. Lee et al, "Fusion Reactor Nucleonics: Status and Needs," in Proc. 4th Topical Meeting on the Technology of Controlled Nuclear Fusion (King of Prussia, PA, Oct. 14-17, 1980) p. 367.

11. E. T. Cheng and R. W. Conn, "A Multipoint Interpolation Method Based on Variational Principles for Functionals of the Solution to Linear Equations," J. Math, Phys., 17, (5) p. 683 (1976).

12. E. T. Cheng and R. W. Conn, "The Influence of Design Variations on Controlled Thermonuclear Reactor Blanket Neutronic Performance Using Variational Techniques," Nucl. Sci., Eng., 62, p. 601 (1977).

13. G. R. Walsh, Methods of Optimization (John Wiley and Sons, London, England, 1977) p. 81.

14. J. A. Nelder and R. Mead, "A Simplex Method for Function Minimization," Computer Journal, 7, p. 308 (1965).

15. D. Klein, "Optimization Considerations in the Design of a Tokamak Reactor," Trans. American Nuclear Society Summer Meeting (Chicago, IL, June 10-14, 1973) p. 10.

16. D. S. Zuckerman and L. A. Carosella, "Parametric Studies of an Inertial Confinement Fusion Reactor," Trans. American Nuclear Society Winter Meeting (San Francisco, CA, November 11-15, 1979) p. 54.

17. W. R. Meier, Cost-Performance Studies of an Inertial-Fusion Power Plant, Lawrence Livermore National Laboratory, Livermore, CA, Rept. UCRL-50021-79, p. 8-107, (1980).

18. D. H. Berwald and W. R. Meier, "Reactor Systems Modeling for ICF Hybrids," in Proc. 4th Topical Meeting on the Technology of Controlled Nuclear Fusion (King of Prussia, PA, October 14-17, 1980) p. 1487.

19. D. J. Bender, "Mirror Hybrid Reactor Optimization Studies," in Proc. Joint US-USSR Symposium on Fusion Fission Reactors (Livermore, CA, July 13, 1976) p. 37.

20. D. S. Zuckerman and C. G. Bathke, "Optimization Studies of a Commercial EBTR Power Plant," in Proc. 9th Symposium on Engineering Problems of Fusion Research (Chicago, IL, October 26-29, 1981) p. 1839.

21. S. A. W. Gerstl, "A Minimum-Thickness Blanket/Shield with Optimum Tritium Breeding and Shield Effectiveness," in Proc. 3rd Topical Meeting on the Technology of Controlled Nuclear Fusion (Sante Fe, NM, May 9-11, 1978) p. 269.

22. M. A. Abdou, "Nuclear Design of the Blanket/Shield System for a Tokamak Experimental Power Reactor," Nucl. Technol. 29, p. 7 (April 1976).

23. M. Z. Youssef, R. W. Conn, G. A. Moses, Neutronics Optimization Studies for a Proliferation Resistant Fuel Assembly from the Fusion-Fission Fuel Factory, SOLASE-H, University of Wisconsin, WI, Rept. UWFDM 263 (October 1978).

24. O. S. Zuckerman, et al., "Impact of Blanket and Shield Materials on Cost of an EBT Fusion Power Plant", in Proc. 2nd Topical Meeting on Fusion Reactor Materials (Seattle, WA, August 9-12, 1981) p. 603.

25. Y. Gohar and M. A. Abdou, "Neutronic Optimization of Solid Breeder Blankets for STARFIRE Design," in Proc. 4th Topical Meeting on the Technology of Controlled Nuclear Fusion (King of Prussia, PA, October 14-17, 1980) p. 628.

26. L. J. Perkins and G. L. Kulcinski, "Economic Design Optimization of the LiPb Blanket for the Mirror Advanced Reactor (MARS)," Nucl. Tehcnol./Fusion, 4, p. 1107. (Sept. 1983).

27. M. A. Abdou and C. W. Maynard, "Nuclear Design of the Magnet Shield for Fusion Reactors," in Proc. 1st Topical Meeting on the Technology of Cpntrolled Nuclear Fusion (San Diego, CA, April 16-18, 1974) p. 685.

28. M. Kasai, S. An, S. Kondo, "Parametric Study and Optimization of CTR Engineering Design," in Proc. 5th Symposium on Engineering Problems of Fusion Research (Princeton, NJ, November 5-9, 1973) p. 257.

29. W. W. Engle, Jr., and F. R. Mynatt, "A Shield Optimization Technique with Direct Utilization of Transport Calculations," Trans. American Nuclear Society Winter Meeting (San Francisco, CA, November 30-December 4, 1969) p. 953.

30. G. S. Schwartz, An Optimization Method for the Design and Operation of Fusion-Fission Hybrid Breeder Reactors, M.S. thesis, Pennsylvania State University, Penn. (1982).

31. E. Greenspan, A Method for the Optimization of Fusion Reactor Neutroonic Characteristics, Princeton University, Princeton, Rept. MATT-481 (1972).

32. E. Greenspan, W. G. Price, Jr., H. Fishman, SWAN: A Code for the Analysis and Optimization of Fusion Reactor Neucleonic Characteristics, Princeton University, Princeton, Rept. MATT-1008 (Nov. 1973).

33. W. M. Stacey, Jr., "Variational Estimates and Generalized Perturbation Theory for the Ratios of Linear and Bilinear Functionals," J. Math, Phys., 13, 8, p. 1119 (1972).

34. R. W Conn and W. M. Stacey, Jr., "Variational Methods for Controlled Thermonuclear Reactor Blanket Studies," Nucl. Fusion, 13, p. 185 (1973).

35. S. A. W. Gerstl and W. M. Stacey, Jr., "A Class of Second-Order Approximate Formulations of Deep Penetration Radiation Transport Problems," Nucl. Sci. Eng., 51, p. 339 (1973).

36. E. T. Cheng, "Application of Generalized Variational Principles to Controlled Thermonuclear Reactor Neutronics Analysis," Nucl. Sci. Eng., 74, p. 147 (1980).

37. W. M. Stacey, Jr., Variational Methods in Nuclear Reactor Physics, (Academic Press, Inc., New York, 1974).

38. E. T. Cheng and R. W. Conn, "Application of Variational Methods to Fusion Reactor Blanket Studies," Trans. American Nuclear Society Summer Meeting (Philadelphia, PA, June 23-27, 1974) p. 27.

39. G. I. Bell and S. Glasstone, Nuclear Reactor Theory, (Van Nostrand Reinhold Co., New York, 1970).

40. R. Roussopoulos, "Methodes Variationueles en Theories des Collisions," C. R. Acad. Sci., 236, p. 1858 (1953).

41. S. Glasstone and A. Sesonske, Nuclear Reactor Engineering (Van Nostrand Reinhold Co., New York, NY, 1967).

42. W. Spendley, G. R. Hext, F. R. Himsworth, "Sequential Applications of Simplex Designs in Optimization and Evolutionary Operation," Technometrics, 4, p. 441 (1962).

43. D. B. Fox and J. S. Liebman, "A Discrete Nonlinear Method for Optimized Engineering Design," Engineering Optimization, 5, p. 129 (1981).

44. J. M. Parkinson and D. Hutschinson, "An Investigation into Efficiency of Variants on the Simplex Method," Numerical Methods for Non-linear Optimization (Academic Press, 1972) p. 115.

45. J. Trenholme, Lawrence Livermore National Laboratory, Livermore, CA, private communication (June, 1983).

46. 1978 Laser Program Annual Report, Lawrence Livermore National Laboratory, Livermore, Rept. UCRL-50021-78 (1979) section 9.

47. 1979 Laser Program Annual Report, Lawrence Livermore National Laboratory, Livermore, Rept. UCRL-50021-79 (1980) section 8.

48. 1980 Laser Program Annual Report, Lawrence Livermore National Laboratory, Livermore, Rept. UCRL-50021-80 (1981) section 9.

49. 1981 Laser Program Annual Report, Lawrence Livermore National Laboratory, Livermore, Rept. UCRL-50021-81 (1982) section 8.

50. M. Monsler et al., "Electric Power from Laser Fusion: The HYLIFE Concept," in Proc. 13th IECEC Conf. (San Diego, CA, Aug. 1978), p. 2164.

51. M. J. Monsler and W. R. Meier, "A Conceptual Design Strategy for Liquid-Metal-Wall Inertial Fusion Reactors," Nucl. Eng. Des., 63, p. 289 (1981).

52. W. R. Meier and W. B. Thompson, "Conceptual Design Considerations and Neutronics of Lithium Fall Laser Fusion Target Chambers," in Proc. Third Topical Meeting Technology of Controlled Nuclear Fusion (Santa Fe, NM, May 9-11, 1978), CONF-780508, p. 297.

53 H. I. Avci and G. L. Kulcinski, "The Effect of Liquid-Metal Protection Schemes in Inertial Confinement Fusion Reactors," Nucl. Technol., 44, 333 (1979).

54. W. R. Meier, "Two-Dimensional Neutronics Calculation for the HYLIFE Converter," Nucl. Technol., 52, 22 (1981).

55. Handbook of Chemistry and Physics (CRC Press, Inc., Boca Raton, FL, 1982), 63rd ed.

56. R. T. Perry and C. W. Mynard, "A Review of Neutronic Design Criteria," in Proc. Fourth Topical Meeting on Controlled Nuclear Fusion (King of Prussia, PA, Oct. 14-17, 1980), p. 470.

57. J. Jung and M. Abdou, "Importance of Shield Design in Minimizing Radioactive Material Inventory in Tokamaks," in Proc. Fourth Topical Meeting on Controlled Nuclear Fusion (King of Prussia, PA, Oct. 14-17, 1980), p. 458.

58. Mirror Advanced Reactor Study Interim Design Report, Lawrence Livermore National Laboratory, Livermore, Rept. UCRL-53333 (April, 1983).

59. E. E. Bloom, et al., "Vanadium Alloys and Modified Steels for Low-Activation Fusion Reactor Design," in Transactions American Nuclear Society Winter Meeting (Washington, D.C., Nov. 14-18, 1982), p. 305.

60. W. R. Meier, "Tritium Breeding Management in the HYLIFE Chamber," Nucl. Technol., 52, p. 170 (1981).

61. G. L. Kulcinski, "Radiation Damage to Materials in DT Fusion Reactors," in Proc. of the Fifth Conference on Plasma Physics and Controlled Nuclear Fusion Research (Tokyo, Japan, Nov. 11-15, 1974).

62. F. A. Smidt, Jr., "Swelling Behavior of Commercial Ferritic Alloys, EM-12 and HT-9, as Assessed by Heavy Ion Bombardment," Irradiation Effects on the Microstructure and Properties of Metals, ASTM STP 611, 1976, pp. 227-241.

63. E. E. Bloom, "Candidate First Wall Materials for Fusion Reactors," in Proc. of the Tenth Symposium on Fusion Engineering (Philadelphia, PA, Dec. 5-9, 1983).

64. W. E. Mooz, Cost Analysis of Light Water Reactors, Rand Corporation, Santa Monica, CA, Rept. R-203-DOE (June 1978).

65. E. F. Plechaty and J. R. Kimlinger, TARTNP: A Coupled Neutron-Photon Monte Carlo Transport Code, Lawrence Livermore National Laboratory, Livermore, Rept. UCRL-50400, Vol. 14 (1976).

66. J. R. Kimlinger, Lawrence Livermore National Laboratory, Livermore, private communication (Oct. 1983).

67. D. G. Doran, J. N. Graves, "Neutron Displacement Damage Cross Sections for Structural Metals," Irradiation Effects on the Microstructure and Properties of Metals, ASTM STP 611, 1976, pp. 463-482.

68. D. G. Doran, "Neutron Displacement Cross Sections for Stainless Steel and Tantalum Based on a Lindhard Model," Nucl. Sci., Eng., 49, 130 (1972).

69. D. G. Doran, "Displacement Cross Sections for Iron, Nickel, Stainless Steel, and Tantalum," Nucl. Sci., Eng., 52, 398 (1973).

70. M. D. Greenberg, Foundations of Applied Mathematics, (Prentice-Hall, Inc., Englewood Cliffs, NJ) 1978.

71. J. H. Pitts, "Cascade: A Centrifugal-Action Solid Breeder Reaction Chamber," Nucl. Technol./Fusion, 4, p. 967 (1983).

72. J. H. Pitts, "Shock Propagation Through the Cascade ICF Reactor Li_2O-Pebble Blanket," Trans. American Nuclear Society Winter Meeting (San Francisco, CA, Oct. 30-Nov. 3, 1983) p. 184.

73. C. E. Johnson, "Recent Advances in the Development of Solid Breeder Blanket Materials," to be published in Proc. on 3rd Top. Mtg. on Fusion Reactor Materials (Albuquerque, NM, Sept. 19-22, 1983).

74. J. H. Norman and G. R. Hightower, "Measurements of the Activity Coefficient of LiOH Dissolved in $Li_2O(s)$ for an Evaluation of Li_2O as a Tritium Breeder Material," to be published in Proc. on 3rd Top. Mtg. on Fusion Reactor Materials (Albuquerque, NM, Sept. 19-22, 1983).

75. P. A. Finn, et al, "Compatibility Study of Solid Ceramic Breeder Materials," in Proc. on 2nd Top. Mtg. on Fusion Reactor Materials (Seattle, WA, Aug. 9-12, 1981) p. 561.

76. R. J. Howerton, Thresholds of Nuclear Reactions Induced by Neutrons, Photons, Protons, Deuterons, Tritions, and Alpha Particles, Lawrence Livermore National Laboratory, Livermore, Rept. UCRL-50400, Vol. 9 (Sept. 1970).

77. J. H. Pitts, et al, A High-Temperature, Low-Activation Design for the Cascade Reactor, Lawrence Livermore National Laboratory, Livermore, Rept. UCRL-90199 Sum. (Jan. 1984). To be presented at the 1984 American Nuclear Society Summer Meeting in New Orleans, June 3-8, 1984.

78. V. A. Murry and M W. McDowell, Primary Heat Transfer Loop Design for the Cascade Inertial Confinement Fusion Reactor, Lawrence Livermore National Laboratory, Livermore, Rept. UCRL-15578 Sum. (Jan. 1984). To be presented at the 1984 American Nuclear Society Summer Meeting in New Orleans, June 3-8, 1984.

79. O. R. Walton, Granular Flow Considerations in the Design of a Cascade Solid Breeder Reacton Chamber, Lawrence Livermore National Laboratory, Livermore, Rept. UCID-19903 (Oct. 1983).

80. J. H. Pitts, "Mechanical and Thermal Design of the Cascade Reactor," to be published in Proc. on 10th Symposium of Fusion Engineering (Philadelphia, PA, December 5-9, 1983).

81. I. Maya, G. A. Technologies, San Diego, CA, private communication (March 1984).

82. W. R. Meier, "Neutron Leakage Through Fusion Chambers Ports: A Comparison of Lithium and Lead-Lithium Blankets," Nucl. Technol./Fusion, 3, p. 385 (May 1983).

83. D. C. Luenberger, Introduction to Linear and Nonlinear Programming (Addision-Wesley, Reading, PA, 1973).

APPENOIX - I DERIVATIVE OF THE THREE POINT INTERPOLATION FORMULA WITH Σ(x) PROPORTIONAL TO x.

Consider the case where Σ(x) is proportional to x. The three point interpolation formula, Eq. 2.64, becomes

$$R_{SI3} = xR_a/x_a - [(x-x_a)/(x_c-x_a)][x_cR_a/x_a - R_c][xR_b/x_b - xR_a/x_a]/D, \quad (I.1)$$

where

$$D = [(x-x_b)/(x_c-x_b)][x_cR_b/x_b - R_c] - [(x-x_a)/(x_c-x_a)][x_cR_a/x_a - R_c].$$

Equation I.1 can be rewritten as

$$R_{SI3} = xR_a/x_a - [(x-x_a)/x_a][xR_b/x_b - xR_a/x_a]i_{ac}/D, \quad (I.2)$$

where

$$D = (x-x_b)i_{bc}/x_b - (x-x_a)i_{ac}/x_a,$$

$$i_{ac} = (x_cR_a - x_aR_c)/(x_c-x_a),$$

and

$$i_{bc} = (x_cR_b - x_bR_c)/(x_c-x_b).$$

Note that i_{ac} is the intercept on the R-axis of a straight line through the points (x_a,R_a) and (x_c,R_c). Likewise, i_{bc} is the intercept on the R-axis of a line through (x_b,R_b) and (x_c,R_c).

Gathering terms, Eq. I.2 can be rewritten as

$$R_{SI3} = xR_a/x_a - (C_1x^2 - C_2x)/(C_3x + C_4), \qquad (I.3)$$

where

$$C_1 = i_{ac}(R_b/x_b - R_a/x_a)/x_a,$$

$$C_2 = i_{ac}(R_b/x_b - R_a/x_a),$$

$$C_3 = i_{bc}/x_b - i_{ac}/x_a, \text{ and}$$

$$C_4 = i_{ac} - i_{bc}.$$

The derivative of R_{SI3} with respect to x is then,

$$R'_{SI3} = R_a/x_a - [(C_3x + C_4)(C_1x - C_2) - (C_1x^2 - C_2x)C_3]/D, \qquad (I.4)$$

where

$$D = (C_3x + C_4)^2.$$

The limit as x approaches zero is

$$\lim_{x \to 0} R'_{SI3} = R_a/x_a + C_2/C_4. \qquad (I.5)$$

To avoid negative values of R as x approaches zero, Eq. I.5 must be greater than or equal to zero. That is,

$$R_a/x_a - i_{ac}(R_b/x_b - R_a/x_a)/(i_{ac} - i_{bc}) \geq 0, \qquad (I.6)$$

or

$$(i_{ac}R_b/x_b - i_{bc}R_a/x_a)/(i_{ac} - i_{bc}) \geq 0. \qquad (I.7)$$

APPENDIX II USER INFORMATION

The fusion reactor blanket optimization code is available on the National Magnetic Fusion Energy Computer Center (NMFECC) system. To access the code type

```
FILEM RDS 3011 .FRBOPTC filelist
```

where "filelist" is one or more of the following filenames.

MVOHY = multivariable optimization program for the modified HYLIFE concept. It includes the figure of merit function and the successive interpolation functions. MVOHY reads INPUT, calls CREEP, and writes OUTFILE.

INPUT = sample input file for MVOHY. This file allows the user to change the starting point of the search, the step size, the convergence criterion, and the maximum number of iterations without recompiling the program.

OUTFILE = sample output file from MVOHY. It includes information written by CREEP.

CREEP = subroutine for the direct search, nonlinear simplex optimization algorithm.

BCRP = binary file of CREEP.

MVOHY3 = multivariable opitmization program for the modified HYLIFE concept which includes three point interpolation for one of the variables.

MVOCS = multivariable optimization program for the Cascade reactor concept. This is a 3 variable problem.

Combining an MVO program with the subroutine CREEP makes up the fusion reactor blanket optimization code. The code runs on CRAY-1 machines with the CIVIC compiler.

The figure of merit function in MVO changes from problem to problem. Since the optimization algorithm, CREEP, does not change from problem to problem, the binary file BCRP can simply be passed to the loader using a LIB= specification in the CIVIC statement. Alternatively, the subroutine CREEP must be merged with the MVO program.

Many comment statements have been included in an attempt to make the MVO and CREEP routines self explanatory. Questions that do arise can be referred to the author in care of Lawrence Livermore National Laboratory, Livermore, CA 94550.

U. S. Government Printing Office: 1984/6-787 002/A4047